

AN ABSTRACT OF THE DISSERTATION OF

Wei Wang for the degree of Doctor of Philosophy in Chemical Engineering presented on July 5, 2012.

Title: Fabrication of CuInGaSe₂ Thin Film Solar Cells using Low-cost Air-stable Inks

Abstract approved: _____

Chih-Hung Chang

CuInGaSe₂ (CIGS), a promising thin film solar cell material, has gained lots of attention in decades due to its high energy conversion efficiency and potential lower manufacture cost over conventional Si solar cells. As a cheaper processing method compared to vacuum-based techniques, solution-based deposition has been successfully applied to fabricate electronic devices, such as transistors and solar cells. In my research, CIGS thin film solar cells with energy conversion efficiencies up to 8.01% were successfully fabricated using newly developed air-stable, low-cost inks. The inks consist of commercially available, low-cost compounds and solvents and can be processed using a variety of printing and coating techniques. More importantly, it can synthesize CIGS films free of contamination from copper selenides and amorphous carbon which are common issues for most of solution-based techniques. Besides, high-quality micrometer-sized CIGS films were obtained by using our

enhanced selenization approach. Various characterization techniques were employed to qualitatively and quantitatively characterize the semiconductor materials and devices fabricated by this process. The mechanism for the transformation from metal salt precursor films to CIGS absorber thin films and the influence of ink composition and selenium vapour pressure on absorber film quality and photovoltaic device performance were investigated and discussed.

©Copyright by Wei Wang

July 5, 2012

All Rights Reserved

Fabrication of CuInGaSe₂ Thin Film Solar Cells using Low-cost Air-stable Inks

by

Wei Wang

A DISSERTATION

submitted to

Oregon State University

in partial fulfillment of

the requirements for the

degree of

Doctor of Philosophy

Presented July 5, 2012

Commencement June 2013

Doctor of Philosophy dissertation of Wei Wang presented on July 5, 2012.

APPROVED:

Major Professor, representing Chemical Engineering

Head of the School of Chemical, Biological & Environmental Engineering

Dean of the Graduate School

I understand that my dissertation will become part of the permanent collection of Oregon State University libraries. My signature below authorizes release of my dissertation to any reader upon request.

Wei Wang, Author

ACKNOWLEDGEMENTS

I like to express my sincere gratitude and heartfelt appreciation to Dr. Chih-Hung Chang for his enormous support and invaluable guidance for this project. I am greatly indebted to Dr. Chang for his heuristic suggestion and inspirational encouragement through this research projects and during the writing of this dissertation. I would like to thank Dr. Shi-Joon Sung and Dae-Hwan Kim from Green Energy Research Division, Daegu Gyeongbuk Institute of Science & Technology, Daegu, Korea for their financial support. This work was supported by the DGIST R&D Program of the Ministry Education, Science and Technology of Korea (12-BD-0101), US Department of Energy, Industrial Technologies Program, through award #NT08847, under contract DE-AC-05-RL01830, OSU Venture fund, ONAMI and Oregon BEST.

I would like to extend my appreciation to my current and previous committee members: Dr. Chong Fang, Dr. Christine Kelly, Dr. Gregory S. Herman, Dr. Brady Gibbons, Dr. Daniel R. Palo, and Dr. Alex Yokochi for their time and commitment to my PhD program.

I would like to thank Dr. Shi-Joon Sung and Dae-Hwan Kim from Green Energy Research Division, Daegu Gyeongbuk Institute of Science & Technology, Daegu, Korea and Dr. Yi Liu from Electron Microscopy Laboratory at Oregon State University for his assistance of TEM and SEM imaging.

I also want to thank all of my colleagues Yu-Wei Su, Seung-yeol Han, Katherine Han, Changqing Pan, Changho Choi, Paravee Vas-Umnuay, Dick Chiu, and Yong Li for their academic assistance and all others who ever helped me.

Finally, I like to dedicate my most grateful blessing to my wife Qian Lu, my daughter Jia Yue Wang and my family for their love.

TABLE OF CONTENTS

	<u>Page</u>
Chapter 1 Introduction	1
Chapter 2 Literature review	5
2.1 CuInGaSe ₂	5
2.2 Vacuum-based techniques	9
2.2.1 Co-evaporation	9
2.2.2 Sputtering and chalcogenization	11
2.2.3 Other vacuum techniques	14
2.3 Non-vacuum-based techniques	15
2.3.1 Nanoparticles	15
2.3.2 Electrodeposition	22
2.3.3 Hydrazine	24
2.3.4 Sol-gel and pyrolysis	25
2.3.5 Film deposition techniques	26
2.3.6 Comparisons between non-vacuum techniques	27
2.4 Solar cells	29
2.4.1 Current-voltage characteristics of diodes	30
2.4.2 Ideal solar cells under illumination	34
2.4.3 Non-ideal solar cells	36
Chapter 3 Chalcopyrite thin film deposition and device fabrication	39
3.1 Chalcopyrite thin film deposition by low-cost air-stable metal salt inks	39
3.1.1 Ink preparation	39

TABLE OF CONTENTS (Continued)

	<u>Page</u>
3.1.2 Thin film deposition.....	40
3.2 Fabrication of CIGS thin film solar cells	42
3.2.1 Molybdenum back contact deposition	42
3.2.2 Absorber formation by selenization	42
3.2.3 CdS buffer layer deposition	45
3.2.4 Window layer deposition	47
3.2.5 Al top contact deposition	47
Chapter 4 Results	49
4.1 Characterization of materials.....	49
4.1.1 Molybdenum back contact	49
4.1.2 Absorber films.....	50
4.1.3 Buffer layer CdS	68
4.1.4 Window layer ZnO	68
4.2 Solar cell characterization	70
4.2.1 Current-voltage analysis	70
4.2.2 Quantum efficiency (QE).....	74
Chapter 5 Discussions	78
5.1 Thermodynamics of selenization.....	78
5.2 Characterization of solar cells using recipe A	81
5.3 Carbon contamination issue	86
5.4 Resolving carbon contamination issue using recipe B	88

TABLE OF CONTENTS (Continued)

	<u>Page</u>
5.5 Improved CIGS crystallinity	91
5.6 Future works	97
Chapter 6 Conclusion	100
References	102

LIST OF FIGURES

<u>Figure</u>	<u>Page</u>
Figure 2.1 CuInSe ₂ unit cell.....	6
Figure 2.2 CuInGaSe ₂ solar cell structure.....	6
Figure 2.3 CuInGaSe ₂ solar cell bandgap energy structure.	8
Figure 2.4 Schematic of a CIGS three-stage co-evaporation system (a) and elemental deposition rates (b).....	10
Figure 2.5 Comparison between the metal salt route and nanoparticle route.	29
Figure 2.6 P-N junction energy band diagram for (a) $V_a=0V$, (b) $V_a>0$, (c) $V_a<0$	31
Figure 2.7 Current density profiles in a p-n junction diode.	33
Figure 2.8 J-V characteristics of solar cells.	35
Figure 2.9 The equivalent circuit of a non-ideal solar cell.	36
Figure 3.1 Schematic of CIGS film deposition by inkjet printing.	40
Figure 3.2 Dimatix DMP-2800 inkjet printer.	41
Figure 3.3 Schematic of CIGS film fabrication process by spin casting.	41
Figure 3.4 Illustration of furnace setups for selenization (a): low selenium vapor pressure, (b): high selenium vapor pressure.....	43
Figure 3.5 Schematic of selenization reactions.....	44
Figure 3.6 Schematic of CdS deposition by chemical bath deposition.....	45
Figure 3.7 Schematic of CdS deposition by continuous flow deposition.	46
Figure 3.8 Mask pattern for Al evaporation. Chapter 4 Results	48
Figure 4.1 Illustration of van der Pauw method for sheet resistance measurement.....	50
Figure 4.2 TGA result for the ink using recipe A.	51
Figure 4.3 TGA results for copper acetate, indium acetate, gallium acetylacetonate and the ink using recipe B.....	53

LIST OF FIGURES (Continued)

<u>Figure</u>	<u>Page</u>
Figure 4.4 X-ray diffraction of CIS and CIGS films made from recipe A.	54
Figure 4.5 X-ray diffraction of CIS films made from recipe A at different selenization temperatures. JCPDS #: CuInSe ₂ (87-2265), Cu _{2-x} Se (06-0680), Cu ₄ O ₃ (83-1665), In ₂ O ₃ (88-2160) and CuCl (06-0344).....	55
Figure 4.6 X-Ray diffraction of CIS and CIGS films made from recipe B.	56
Figure 4.7 X-ray diffraction of CIS films made from recipe B at different selenization temperatures. JCPDS #: CuInSe ₂ (87-2265), Cu _{2-x} Se (06-0680), CuSe (49-1457), and Se (51-1389).....	57
Figure 4.8 Raman spectrum of CIS films made from recipe A.	59
Figure 4.9 Raman spectra of CIGS films made from recipe B at different selenization temperatures.	60
Figure 4.10 UV-Vis-NIR spectra of CIGS films with various Ga concentrations using recipe B.	62
Figure 4.11 Scanning electron microscopy images of CIGS films using recipe A.....	64
Figure 4.12 SEM images of CIGS films using recipe B under low Se pressure.....	64
Figure 4.13 SEM images of CIGS films using recipe B under high Se pressure.	65
Figure 4.14 TEM cross-section images (a,b) and elemental mappings (c, d) of CIS and CIGS films, (a, c) for CIS and (b, d) for CIGS.	67
Figure 4.15 TEM images of ZnO/CdS/CIGS structures.	68
Figure 4.16 XRD and UV-Vis-NIR (insets) spectra of i-ZnO (a) and Al:ZnO (b).....	69
Figure 4.17 J-V characteristics of a solar cell. (a) measured and simulated J-V curves, (b) plotting equation (5) and (6) to extrapolate device parameters.	73
Figure 4.18 (a) External QE, internal QE and reflectance of a solar cell, (b) bandgap energies extracted from IQE in forward bias range.	76
Figure 4.19 EQE curves of CIGS solar cells at 0V and 1V bias. Top inset: EQE ratio at -1V and 0V bias.	77

LIST OF FIGURES (Continued)

<u>Figure</u>	<u>Page</u>
Figure 5.1 Gibbs free energies of CIS formation using CuCl and CuCl ₂	81
Figure 5.2 SEM images of CIGS films: (A) top view of a CIGS film and (B) cross-sectional view of the full device.....	82
Figure 5.3 Optical Image (a) and Raman mapping image (b) of CIGS films and Raman spectra corresponding to Raman mapping image (c).	83
Figure 5.4 J-V characteristics of a CIGS solar cell.	84
Figure 5.5 Comparison of J-V measurements of CIGS solar cell at dark, AM1.5 and 610nm long pass filter.	85
Figure 5.6 Raman spectrum of a CIGS film using recipe B.	88
Figure 5.7 SEM images of precursor film and CIGS film: top-view (a) and side view (b) of precursor film, top view (c) and side view (d) of CIGS film.	89
Figure 5.8 J-V characteristics of CIGS thin film solar cells using recipe B.	90
Figure 5.9 TEM elemental profiles of CIS and CIGS thin films.	91
Figure 5.10 XRD comparison of CIS and CIGS films, Inset: Raman spectra for the same films.	92
Figure 5.11 SEM cross-section images of CIGS films selenized at low Se pressure (a) and high Se pressure (b).	93
Figure 5.12 J-V characteristics of CIGS solar cells selenized at different Se partial pressures.	94
Figure 5.13 Bandgap measurement by UV-Vis absorption.	96
Figure 5.14 Grazing incidence XRD of a CIGS film at different angles.	99

LIST OF TABLES

<u>Table</u>	<u>Page</u>
Table 3.1 Chemical list for recipe A	39
Table 3.2 Chemical list for recipe B	39
Table 3.3 Chemical list for CBD.....	45
Table 3.4 Chemical list for CFD	46
Table 4.1 Compositional comparison between WDS results on CIGS films and calculated results based on precursors' weights.....	63
Table 4.2 Device parameters of a solar cell	74
Table 5.1 Gibbs free energy of forming ternary selenide CIS	78
Table 5.2 Gibbs free energy of forming binary selenides	79
Table 5.3 Gibbs free energy of transformation of oxides to selenides.....	80
Table 5.4 Device characteristics of CIGS solar cells selenized at different Se pressures	95

Chapter 1 Introduction

Currently, chalcopyrite CuInGaSe_2 (CIGS) thin film solar cells have reached up to 20.3% power conversion efficiency using a three stage co-evaporation process¹, which is comparable with the energy conversion efficiency of multicrystalline Si solar cells. Decent conversion efficiency and high chemical stability of CIGS make itself a promising p-type material for thin film solar cells. However, the high cost of vacuum-based fabrication process becomes a barrier to affordable commercial modules for the substitution of conventional fossil fuels as a primary energy source. An efficient non-vacuum printing process has the potential to overcome this barrier. Nanosolar Inc.² utilizing formulated inks containing binary copper/indium/gallium selenide nanoparticles successfully fabricated 15% CIGS thin film solar cells via high throughput roll-to-roll printing. Guo *et al.*³ synthesized CuInS_2 and CuInGaS_2 nanoparticles by hot injecting method and converted nanoparticle-stacked sulfide films to densified selenide thin films. The resulting cells demonstrate a maximum energy conversion efficiency of 12.5%. Kapur *et al.*⁴ reduced oxide nanoparticles using pure hydrogen to metal films which were then converted to chalcopyrite CuInGaSe_2 films by selenization. A maximum cell efficiency of 13.6% was achieved from these films. All these methods using precursor films made of nanoparticles require extra preparation steps such as mechanical milling or chemical synthesis. The final absorber films were deprived of their initial nano-structured features. These additional steps for the preparation of nanoparticles and hydrogen reduction are likely to increase the manufacture cost and decrease the production yield. A scalable and high throughput

synthesis process is needed to lower down the cost of these nanocrystal inks.

Bhattacharya *et al.*⁵ used electroplating method to fabricate CIGS thin film solar cells with an efficiency of 15.4%. However, a post composition adjustment by physical vapour deposition is required to ensure a Cu-poor CIGS films. Guillemoles *et al.*⁶ fabricated CIGSSe solar cells using precursor films by electrodeposition following by sulfurization. Hydrazine is a powerful solvent which can dissolve various binary metal selenides and sulfides with additional chalcogen elements. Todorov *et al.*⁷ demonstrated CIGS cells with a 15.2% energy conversion efficiency using this method. However, due to the toxic and explosive nature of hydrazine and slow dissolution rate of chalcogenides, the wide application of this method will require careful engineering work to ensure the safety of working environment. Weil *et al.*⁸ demonstrated an air-stable vulcanized ink for the production of large-grained CuInS₂ absorber layers by rolling printing process with a post KCN etching. A power conversion efficiency of 2.15% was achieved.

Lee *et al.*⁹ have developed a process that uses metal salt precursors dissolved in an aprotic solvent (i.e. acetonitrile) and is capable of forming uniform and continuous thin films through both digital fabrication (e.g. inkjet printing) and blanket coating (e.g. spin coating) techniques. This feature makes the printing process follows a simple dissolution and drying mechanism. In addition, the high volatility of solvent helps convert the printed liquid thin films into solid metal salt thin films in a short time. The printed metal salt thin films were converted into oxide semiconductors through a substitution reaction between the metal halide and oxygen (i.e. H₂O). This synthetic

pathway opens a general route to fabricate a variety of patterned metal oxide semiconductors through a simple and low-cost process at an atmospheric environment¹⁰. Herein, we are able to extend this approach to enable printing of chalcopyrite semiconductors (e.g. CuInGaSe₂) for solar cell application.

Deposition at atmospheric environment offers an opportunity for the deposition of absorber materials at large scale with high throughput. This provides a potential cost advantage over conventional fabrication process that involves expensive vacuum equipment. In addition, solution processes (such as inkjet printing, spray and roll-to-roll printing) are able to increase the raw material utilization ratio compared to more wasteful vacuum-based deposition techniques.

The solution-based solar cell fabrication process reported in this work has several advantages over the conventional vacuum based techniques and other solution approaches. The solution based approaches in general could potentially lower down the capital cost associated with the more expensive vacuum equipment. The newly developed route that was investigated in this work uses low-cost and benign metal salts directly as starting materials. This route shortens the reaction pathway for the fabrication of CIGS thin films which will reduce the processing cost and lower its environmental impact. In contrast, a number of solution processes require additional chemical treatment for the removal of secondary phase, the use of toxic chemicals or tedious process to prepare the precursors. From a chemistry standpoint, metal salts such as metal chloride and acetate are more reactive than metal oxides which have

been successfully used to fabricate CIGS solar cells^{4, 11-13}. These benefits make metal salts good candidates to serve as CIGS precursors. The most efficient CIGS solar cell is fabricated by co-evaporation with elemental concentration gradients which are beneficial for the cell performance¹. The printing technique could potentially be used to create a similar gradient by adjusting the ink concentration. Herein, I present a low-cost and air-stable approach for the fabrication of chalcopyrite $\text{CuIn}_x\text{Ga}_{1-x}\text{Se}_2$ thin film solar cells using metal salts as starting materials.

Chapter 2 Literature review

2.1 CuInGaSe₂

CuInGaSe₂ (CIGS), the most efficient thin-film solar cell technology, has reached up to 20.3% efficiency which is comparable with the energy conversion efficiency of multicrystalline Si solar cells¹. Continuous effort was spent on this material in the last several decades. Since 1953 when CuInSe₂ was synthesized for the first time¹⁴, it took 20 years to create the first CIS PV devices in 1973¹⁵. In the middle of 1980s, Boeing¹⁶ introduced two-stage coevaporation method to fabricate polycrystalline CIS films with >10% efficiency in integrated solar cells. So far, CIGS solar cells fabricated by three stage co-evaporation process hold 20% energy conversion efficiency which is the highest record for thin film polycrystalline solar cells^{17, 18}.

CuInSe₂ belonging to I-III-VI materials family with tetragonal chalcopyrite structure (see figure 2.1) which is similar to cubic zinc blende structure of II-V materials like ZnSe¹⁴. Due to the very different nature of copper and indium atoms, the bonds between them and neighboring selenium atoms have very different ionic properties and lengths, which make CIS structure anisotropic in most cases¹⁹.

By adding other elements into chalcopyrite structures, the bandgap energies of this materials range from 1.04eV in CuInSe₂ to 1.65eV in CuGaSe₂, and even to 2.4eV in CuGaS₂ and 2.7eV in CuAlS₂¹⁴. It is interesting to note that the most efficient chalcopyrite solar cells is not made from pure ternary compounds but rather alloys like CuInGaSe₂. The quaternary CIGS phase has several advantages over ternary

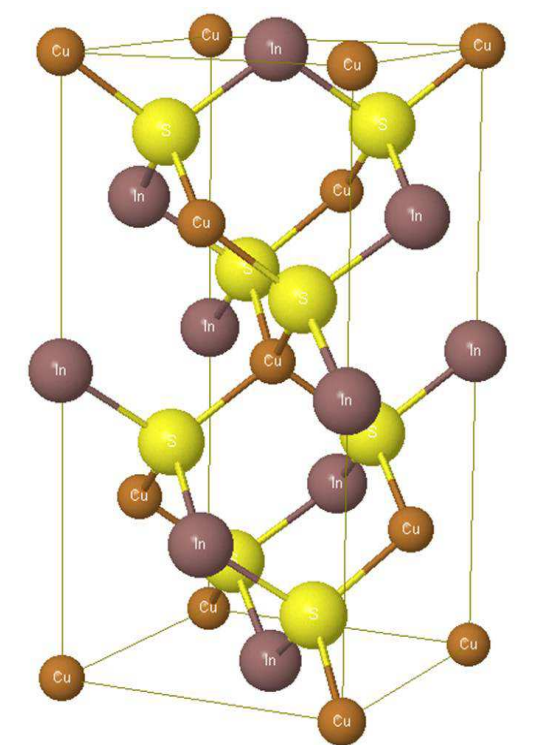


Figure 2.1 CuInSe₂ unit cell.

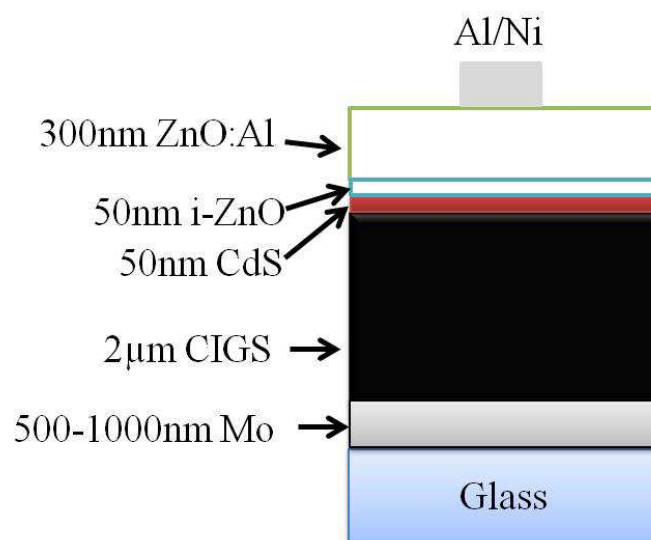


Figure 2.2 CuInGaSe₂ solar cell structure.

compounds. First, the bandgap of CIGS is tunable according to the ratio of In/Ga, which cover most of the visible spectrum. Second, the synthesis of single phase CIGS is easier than the synthesis of single phase CIS¹⁹.

Depending on the dominant defects, CIGS can be either p type or n type. Usually, p-type CIGS is grown under In-rich and Se-rich condition, whereas n-type CIGS is grown under Cu-rich and Se-deficient condition¹⁴. Thus, Cu vacancy and Se vacancy are believed to be the dominant defects in p and n type CIGS, respectively¹⁴.

The CIGS materials have very high absorption coefficient which is larger than 10^5cm^{-1} over most of the visible spectrum¹⁹. Therefore only a-few-micrometer-thick CIGS films are needed to absorb most of the lights, which makes the cost of materials much lower than conventional thick Si solar cells. Besides, CIGS is more stable than some other p-type semiconductors like Cu_2S and less toxic than CdTe which is already a big player in the thin film solar cell market.

CIGS solar cells usually employ a substrate structure which is illustrated in figure 2.2. Molybdenum and transparent conductive oxides (TCO) deposited by sputtering serve as back and front contacts, respectively. ZnO and CIGS form p-n junction with thin CdS layers as buffer layers in the middle. Chemical bath deposition is utilized to deposit CdS layers for most of highly efficient CIGS solar cells.

In order to maximize the collection of photocurrent generated in the absorber layers and efficiency of the devices, bandgap engineering is usually employed for high-efficiency solar cells¹⁴. The common bandgap structure of CIGS solar cells is

exhibited in figure 2.3. At the front side of CIGS layers, the bandgap is enlarged by higher Ga or sulphur concentration. The increased bandgap of front surface of CIGS films can reduce the energy loss during thermalization and recombination at CdS/CIGS interface^{14, 20} and consequently increase open circuit voltage V_{oc} and energy conversion efficiency. At the back side of CIGS films, the bandgap is increased solely by increasing Ga/In ratio. The gradual increase of the conduction-band energy sweeps the photogenerated electrons into the direction of p-n junction¹⁴. This helps the collection of photocurrent current and increase short circuit current J_{sc} .

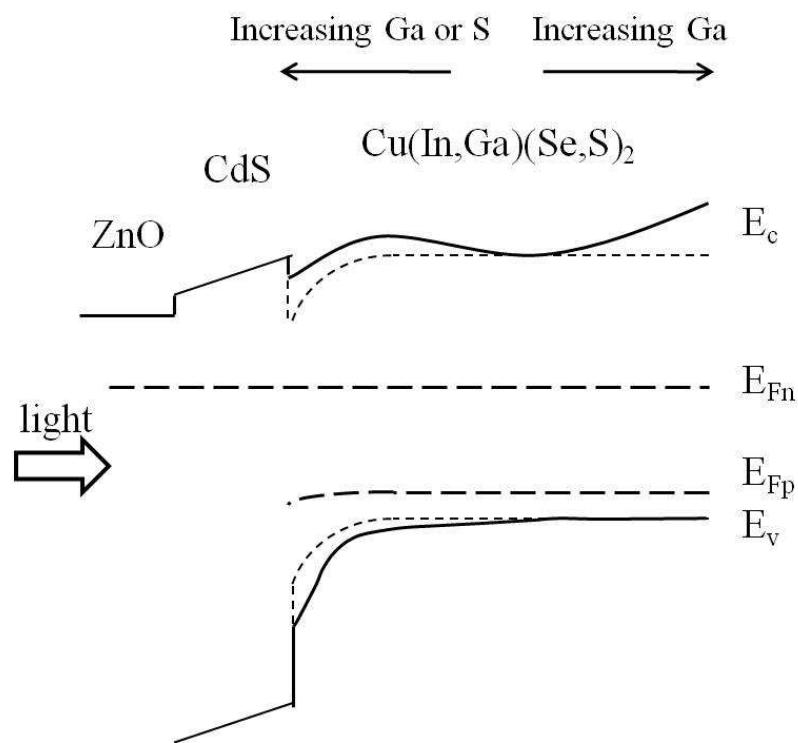
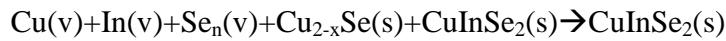
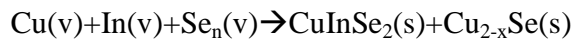


Figure 2.3 CuInGaSe₂ solar cell bandgap energy structure.

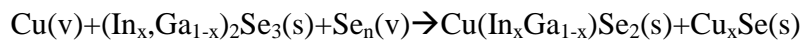
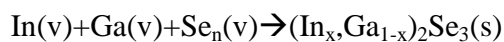
2.2 Vacuum-based techniques

2.2.1 Co-evaporation

CIGS absorbers prepared by co-evaporation from element sources yield the highest efficiencies for thin film photovoltaic devices. In 1980, Mickelsen and Chen¹⁶ made 5.7% polycrystalline CIS PV devices by using a so-called Boeing bilayer co-evaporation process which simultaneously evaporated elemental copper and indium metals under selenium vapor. In order to avoid the interaction between selenide and gold back contact at high temperature, the deposition started with the deposition of low-resistivity small-grain Cu-rich CIS at 350°C and ended with excess indium deposition rate at 450°C. The reaction pathway for this method is illustrated as below¹⁹:



Based on this bilayer co-evaporation process, Gabor *et al.*²¹ refined this approach to form a so-called three-stage co-evaporation process which started deposition with ~90% indium and gallium with excess Se at 250°C-300°C which were followed by copper selenide deposition and finally capped with the rest ~10% indium and gallium at >540°C. The finished CIGS film after three stages is slightly indium-rich. the reaction pathway for three stage co-evaporation is illustrated as below¹⁹:



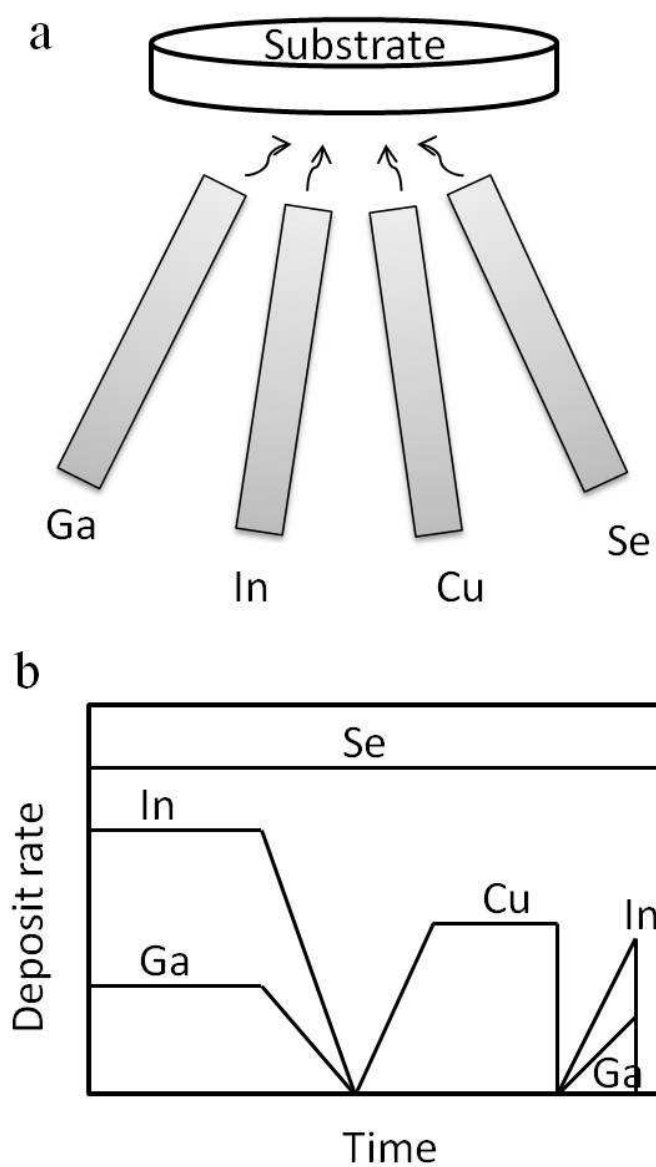
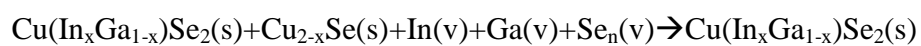


Figure 2.4 Schematic of a CIGS three-stage co-evaporation system (a) and elemental deposition rates (b).

Figure 2.4 shows the schematic of three-stage co-evaporation setup and the elemental deposition rates. Based on Cu-Se binary phase diagram²², Cu_{2-x}Se might exist in a liquid phase with excess Se present at high temperature ($>523^\circ\text{C}$). In the three-stage evaporation approach, Cu_{2-x}Se was formed at the second stage and used as flux agent helping the recrystallization of CIGS grains. Two factors were found to contribute to the cell efficiency by using this process²¹. The surface of finished CIGS films was extremely smooth with roughness less than 50nm. The small roughness of CIGS films resulted in smaller surface area contributing to the junction area and consequently reduced both the recombination happened at the junction interface and the saturation current J_0 . However, a drawback of smoother films is to increase the light reflection on CIGS films. Another factor beneficial to cell efficiency was the gallium gradient as a function of depth in the CIGS films. The gallium concentration increased toward the back of the film. Such notch structure provided quasielectric fields sweeping free electrons from CIGS neutral region to the junction. In the aspect of process control, the deposition in three-stage coevaporation was commonly monitored by mass spectroscopy which provided precise control on the deposition rate of each element¹⁹. So far, CIGS solar cells fabricated by three stage co-evaporation process hold 20% energy conversion efficiency which is the highest record for thin film polycrystalline solar cells^{17, 18}.

2.2.2 Sputtering and chalcogenization

Although co-evaporation method has yielded the best efficiencies in laboratory devices^{17, 18} and is one of the common methods used in the manufacture of commercial CIGS modules²³, There are several drawbacks existing in this process. The uniformity of deposited films by co-evaporation over large areas does not satisfy the requirement for highly efficient modules due to the limitation of the geometry of evaporation source²⁴. Low production throughput and poor simultaneous control of all evaporation sources are barriers impeding the commercial development of co-evaporation technique²⁴.

By virtue of high deposition uniformity and rate, sputtering is a common physical vapor deposition method widely used in the manufacture of thin films. Usually, two separated steps including material deposition and selenization are needed to synthesize CIGS absorber films. Selenization can be conducted during or after sputtering. Marudachalam *et al.*²⁵ utilized DC magnetron sputtering to deposit metal precursor films in a sequence of Cu-Ga-In on Mo-coated soda lime glass substrates which were selenized under the environment of H₂Se/Ar/O₂ gas mixture for 90min. A post-reaction heat treatment in Ar for 60-90min was applied to selenized CIGS films which were converted to single CIGS phase after 600°C treatment. 13% efficiency was achieved by using this three-layer structure. In order to solve the problems of low-melting temperature property of gallium and deleterious interaction between indium and gallium, Dhere *et al.*²⁶ used Cu-Ga alloy and indium targets instead of individual metal targets in a sequence of CuGa/In/CuGa/Selenization/In/CuGa/Selenization. The two-selenization strategy and Ga addition near the Mo contact have significantly

improved the adhesion of CIGS films to the Mo back contact. 9.02% efficiency was achieved by using this approach. In order to further simplify the deposition process and better control the uniformity of metallic precursor films, Cu-In-Ga ternary alloy targets were successfully developed to fabricate CIGS thin film solar cells with 8% efficiency²⁷. The efficiency increased up to 13% by using High Power Impulse Magnetron Sputtering instead of regular DC sputtering in the presence of evaporated selenium²⁸. One issue of this two-step sputtering approach is the gallium accumulation near Mo back contact regions regardless of the kind of targets used^{25, 27}. This led to the phase separation which needs special treatments to recrystallize the films to single phase.

In addition to metallic targets, quaternary chalcogenide targets were also able to be used for CIGS solar cells. RF sputtered films from single phase CIGS targets showed binary selenides which were converted to single CIGS phase by post-selenization with 7.95% efficiency for finished devices²⁹. Frantz *et al.*²⁴ have fabricated highly oriented single phase CIGS absorber films without selenization during or after sputtering achieving 8.9% efficiency for working devices.

Comparing the cells fabricated by co-evaporation and sputtering, the efficiencies from co-evaporated cells are ~6% (absolute) larger than the sputtered cells on the laboratory scale. However, commercial modules made by these techniques have no significant difference in terms of device performances²³. The low elemental uniformity across

solar panels by co-evaporation technique counterbalances the advantage of better crystallinity and cell performances.

2.2.3 Other vacuum techniques

In addition to the aforementioned co-evaporation and sputtering, molecular beam epitaxy and close-space chemical vapor transport are additional vacuum-based methods that have been used for the synthesis of CIGS film³⁰. Single crystalline CIGS films grown by using molecular beam epitaxy perform not as good as the polycrystalline films. Although high quality p-type CIGS films were obtained by close-space chemical vapor transport, this technique uses corrosive HI as a transport agent which is too corrosive for many materials. Due to these reasons, these two methods are rarely used in practice.

Field-Assisted Simultaneous Synthesis and Transfer (FASST) process developed by Heliovolt is a two-stage reactive transfer printing method³¹. In the first step, copper selenide and indium selenide are deposited by PVD on Molybdenum-coated glass substrates and calcium fluoride-coated substrates, respectively. In the second step, these two films are brought to contact closely and go through rapid reaction under pressure and electrostatic field. The final films are transferred to Molybdenum substrates and calcium fluoride-coated substrates can be reused for many times with proper cleaning. Due to the imposed pressure and electrostatic field, the reaction between these two precursors is fast. That may reduce the thermal budget. The resulted CIGS films show a (220)/(204) preferred orientation which is different from

the preferred (112) orientation by other methods. 12% efficiency was achieved by this technique.

2.3 Non-vacuumed-based techniques

2.3.1 Nanoparticles

Nanoparticles or quantum dots are one of the most attractive materials in the scientific world due to their unique properties from bulk materials. In this section, several CIGS deposition approaches based on nanoparticles were reviewed.

2.3.1.1 Metal nanoparticles

Copper and indium metal nanoparticles have been used to produce metal precursor layers which were then subjected to post selenization in either Se or H₂Se gas to form CIS absorber films³². Ideally, this method should be very promising considering the low melting temperatures of indium and energetic nature of both elements which might be beneficial for forming dense films in a short time. However, considerable indium oxide formed during spray deposition in ambient atmosphere contaminates CIS films³².

2.3.1.2 Binary chalcogenides nanoparticles

Nanosolar inc.² has used binary copper selenide and indium/gallium selenides as starting materials to fabricate 14% thin film CIGS solar cells. Single metallic nanoparticles are the simplest form one could design. The structure of nanoparticles used by Nanosolar inc. has a core-shell structure. Copper nanoparticles serve as the

cores which are coated with IIIA-VIA shells such as indium selenide, gallium selenide and *etc.*³³. These selenide nanoparticles are dispersed in organic solution which may contain various ingredients including solvents, surfactants, binders, emulsifiers, thickening agents, film conditioners, anti-oxidants, flow and leveling agents, plasticizers and preservatives³³. The real recipe is not disclosed in the literature but must assure the appropriate properties allowing the formulated ink to be printed. With proper adjustment of ink's rheological and thermal properties, the ink was printed by typical wet coating techniques onto rigid and flexible substrates. Cu_{2-x}Se , having relatively low melting temperature 523°C , is used to assist the growth of large and dense CIGS films. Rapid thermal processing (RTP) was the most critical step to convert porous nanoparticle films into dense PV-quality films. The main advantage of RTP over conventional slow-rate heating processes is its high ramping rate (typically $10\text{-}20^\circ\text{C}/\text{sec}$) which could suppress the selenium loss during annealing and melt down the flux agent Cu_{2-x}Se before it totally reacts with indium/gallium selenides to form CIGS which has high melting temperature over 1000°C . The liquid or quasi-liquid phase of Cu_{2-x}Se having very high flowability compared to solid phase may fill the voids between particles and densify the films. The choice of substrates influences the selenized CIGS grain size and composition in the resulting CIGS films. Sodium is the magic element controlling the migration of gallium across CIGS films. By manipulating the sodium concentration in CIGS films, the gallium profiles can be flat at high Na content or notch-shape at low Na content². The finished PV device has decent characteristics with 14% efficiency for aperture area. By using the similar core-

shell strategy, Yoon *et al.*³⁴ synthesized CuSe/InSe nanoparticles which yield only ~1% efficiency which is much smaller than the result from Nanosolar inc.

2.3.1.3 Metal oxides nanoparticles

Metal oxides are abundant forms of metal compounds existing on the earth. Using metal oxides to synthesize chalcopyrite CIGS may reduce the cost of raw material and potentially the final PV modules. International Solar Electric Technology Inc. (ISET)^{11, 12} and Unisun³⁵ are the two pioneers exploring the area of converting metal oxides to CIGS films. In ISET's method, element copper, indium and gallium with fixed Cu/(In+Ga) ration were dissolved by acid to obtain homogeneously mixed aqueous solution of Cu, In and Ga compounds. These metal ions were co-precipitated by adding sodium hydroxide solution resulting in a mixture of metal hydroxides which were dried at 450°C to obtain fine oxides powder. The size of the oxide particles were controlled by the pH value of reaction mixture and delivery rate of NaOH during hydrolysis. Usually the average diameter of nanoparticles is 250nm with tight distribution. The ink was formulated by dispersing the powder in water and surfactants with assistance of ball milling. The obtained oxides paste can be deposited on Molybdenum-coated substrates by various types of printing techniques. A H₂ reduction reaction was conducted on oxide films which were reduced and converted to metal layers, followed by a selenization or sulfurization process to convert the metal films to CIGS. Unisun³⁵ used oxide nanoparticles as starting materials as well, but the synthesizing method is not clear. However, the reduction reaction by H₂ was not

included in Unisun's process. Cells reached 13.6% and 11.7% efficiency have been achieved in the laboratory by ISET and Unisun, respectively. Two major issues of this oxide nanoparticle approach may counterbalance its advantage in low cost, compositional uniformity and easy handling. Copper oxide, indium oxide and gallium oxide are very stable at room temperature and even high temperature. The good stability makes the ink easily preserved, but impedes the reduction of metal oxides to pure metals. Thermodynamically, the reduction reaction of copper oxide at 500°C is favorable, whereas the reduction of indium and gallium oxides is not favorable even at 500°C¹¹. This disadvantage makes the reduction reaction very difficult to complete and residual oxides are likely to remain in the films. In the ISET approach, elemental metals go through dissolution, precipitation and reduction back to metal forms. From the perspective of mass and energy consumption, this process is not mass and energy efficient at all, that is saying extra energy and materials are consumed and inevitably increase the manufacture cost.

2.3.1.4 Ternary/quaternary nanoparticles

It is a straightforward thought to use ternary/quaternary chalcopyrite particles as 'bricks' to directly build bulk chalcopyrite materials. Guo *et al.*³⁶ and Panthani *et al.*³⁷ have used hot injection method to successfully synthesize CuInSe₂ and CuInS₂ nanoparticles in chalcopyrite phase. The nanoparticles can be dispersed in various non-polar solvents such as hexane, toluene and etc. to form stable ink for printing³⁷. After deposited on substrates, the organic solvents were evaporated by annealing in an

inert atmosphere (e.g. Ar) at 500°C. Afterwards, selenization at 500°C was applied to the nanoparticles films in order to densify and recrystallize the films³⁶. KCN was used to etch Cu_xSe phases and adjust the composition to Indium-rich phase. The obtained PV devices with conventional structures show 3% efficiency with relatively small V_{oc} ³⁶. Small grain size and large grain boundary are the main issues for these devices. CIS has high melting temperature above 1000°C which impedes the recrystallization of CIS nanoparticles even though 500°C selenization was applied. Guo *et al.* synthesized CuInGaS₂ nanoparticles by using similar chemistry and converted CuInGaS₂ nanoparticle films to Cu(In_{1-x}Ga_x)(S_{1-y}Se_y) films by selenization. There are two benefits related with this new strategy. First, the bandgap of CuInSe₂ is about 1eV which is lower than the optimal bandgap 1.14eV for maximum efficiency based on calculation³⁸. Gallium and sulfur are used as doping elements to enlarge the bandgap of CIS to enhance the cell performance. Second, due to larger atomic size of selenium, the replacement of sulfur by selenium during selenization can help the recrystallization of nanoparticles and expand the lattice to eliminate void space between nanoparticles to achieve dense films with larger grain size. The efficiency of CIGSS PV devices increased to 6% by using this new selenization strategy^{39, 40}. By adding another Na soaking step prior to selenization, the efficiency was able to increase to 12%³. In Guo's approach, the nanoparticle films have lost the nano-structured feature during selenization. Instead of 'melting' nanocrystals together, Panthani *et al.*³⁷ used the nanoparticle films to make devices directly without selenization, which preserves the nanoparticle feature. However, due to the high recombination through defects and

impurities, the device performance is much lower than the selenized samples⁴¹.

Another issue related with ternary/quaternary nanoparticles is the low production yield and composition uniformity of nanoparticles synthesized by batch hot injection methods³⁷.

2.3.1.5 Nanoparticles synthesis

Mechanical ball milling is a widely-used method for grinding materials to extremely fine powder⁴². Typical ball mills contain a cylinder rotating around a horizontal axis which is partially filled with the material to be ground and the ground medium (hard materials such as ceramic ball, stainless steel balls and *etc.*). The materials are ground to fine powder by an internal cascading effect. The rotating speed should be smaller than the critical speed after which the ability of grinding decreases, because the ground medium starts to move along with cylinders at the same pace. High-quality ball mills are able to reduce particle size to nanometer scale, resulting in extremely large surface area which may become very reactive. In order to prevent particles from agglomeration, surfactants or organic solvents are added during grinding. For CIGS application, ball mills have been used to grind different precursor materials, such as chalcogenides^{43, 44} and metal oxides^{11, 12}. Chemical reaction can also be introduced during grinding to synthesize CIGS nanoparticles from pure element powders⁴⁵.

Hot injection method developed by Murray *et al.*⁴⁶ in 1993 for the synthesis of monodispersed cadmium chalcogenides quantum dots is one of the most popular methods to make nanoparticles. A multi-necked flask mounted on a heating mantle is

filled by solvents which has been de-gassed by inert gas and connected to vacuum/inert gas by Schlenk line. After the solvents are heated to a certain temperature, the reagents are injected into the flask and the reaction start quickly. In order to control the size and agglomeration of nanoparticles, surfactants have to be added to cap the surface of nanoparticles and stop further reaction and the interaction between particles. The selection of surfactants strongly depends on the type of precursors and the desired properties of nanoparticles. Surfactants are usually long carbon-chain hydrocarbons with nucleophilic groups such as oleic acid, oleylamine, Trioctylphosphine(TOP) *etc.* The nucleophilic groups attach to the surface of nanoparticles via coordinate bonds. By adjusting the strength of coordinate bonds and the temperature of solvents, the size and shape of nanoparticles are able to be controlled precisely. For CIS synthesis^{36, 40}, metal salts, such as CuCl and InCl₃, and Se which are dissolved in oleylamine separately are injected into a preheated (e.g. ~130°C) three-neck flask under the protection of inert gas (e.g. Ar). The temperature is then increased up to 265°C and held for 1 hour to let the particles grow. Hexane and ethanol are added to the mixture to flocculate the nanoparticles after the temperature decreases to 60°C. CIS nanoparticles are separated from the reaction mixture by centrifuge and can be redispersed in non-polar solvents. Gallium can be added to this reaction to form quaternary CIGS crystals.

Solvothermal synthesis is another important solution-based approach to synthesize nanoparticles. The reaction temperature can be lower than the hot injection method since autoclaves are commonly employed to provide relatively high pressure over the

reactants. For CIS synthesis^{47, 48}, metal salts such as copper/indium chlorides and selenium powder are added to autoclaves with solvents and surfactants. The sealed autoclaves are heated at temperature $<200^{\circ}\text{C}$ for several hours to a day then cooled to room temperature naturally. The obtained nanoparticles are collected by centrifuge and redispersed in non-polar solvents. The biggest disadvantage of solvothermal method is its long reaction time compared to the hot injection method.

In order to synthesize metal chalcogenides, the simplest way is the precipitation reaction of metal cations and chalcogenide anions. However, the reaction rate of precipitation is too fast to yield nanoparticles at room temperature. In order to slow down the reaction rate and control the particle size formed in solution, low temperature condition has to be used. Schulz *et al.*⁴⁹ mixed CuI, InI₃, and GaI₃ dissolved in pyridine with Na₂Se in methanol at reduced temperature under inert atmosphere to produce selenides colloids which were amorphous by XRD and TEM. The CIGS PV devices made from the Cu-In-Ga-Se colloids have ~4% efficiency.

2.3.2 Electrodeposition

Electrodeposition is a fully developed technology for mass production of metallic film coatings in industry. However, the application of electrodeposition in semiconductor films was limited since it was much harder to control the semiconductor properties compared to metallic properties⁵⁰. Several deposition strategies were employed to synthesize ternary or quaternary chalcopyrite films. The simplest strategy is to deposit elemental layers (i.e. Cu, In, Ga, Se) from single elemental solutions one by one. The

resulted elemental stack layers are then subjected to selenization for the conversion of precursor films to CIS/CIGS films⁵¹. The electrodeposition potentials over normal hydrogen electrode (NHE) for Cu, In, Ga, Se are 0.35V, -0.34V, -0.53V and 0.75V, respectively⁵⁰. It is fairly easy to electro-deposit Cu and Se by reduction but very difficult for In and Ga depositions due to their negative potential values and the side reaction of reduction of proton. Special efforts are needed to obtain good quality films. Instead of multiple depositions, Herrero *et al.*⁵² deposited Cu-In alloy in a single bath with a negative potential smaller than that of In.

Cu_xSe , In_2Se_3 and Ga_2Se_3 have positive electrodeposition potential vs. NHE and can be deposited easier than the metallic films⁵¹. By mixing metal and Se precursors in solutions, binary selenides can be deposited in sequence on substrates and transformed to ternary or quaternary compounds with an extra annealing step.

Bhattacharya⁵³ is the first one to electro-deposit CuInSe_2 films from single bath containing all three elements. The deposition process is controlled by the ratio between selenium and copper ionic species in an acidic and In-rich environment. The as-deposited films showed a mixture of several phases in a nanocrystalline or amorphous states. In addition to CIS, binary phases were present in the films and transformed to ternary phases easily due to their reactive properties. Due to the poor electronic properties of as-deposited films, extra steps are necessary to recrystallize the films. Selenization is a common method to improve the crystallinity of CIS/CIGS films. Guillemoles *et al.*⁶ fabricated CIGSSe solar cells with 11% efficiency using

precursor films by electrodeposition followed by sulfurization. Bhattacharya *et al.*⁵ utilized physical vapor deposition to adjust the composition of electrodeposited films to indium-rich phase and recrystallize the CIGS_{Se} grains resulting in cells with a 15.4% efficiency.

2.3.3 Hydrazine

An ideal solution-based method for the synthesis of CIGS thin films is dissolving CIGS compound into solvents that can be easily evaporated by mild thermal annealing leaving pure CIGS films. Regular solvents such as water, alcohols and acetone do not have the ability to break down the crystal network of metal or ceramics though. Hydrazine, an extremely polar liquid with similar physical properties as water, possesses the unique reducing nature to dissolve certain metal selenides and sulfides at high concentrations with extra chalcogens⁵⁴.

Commonly, Cu₂S, Ga₂Se₃, In₂Se₃, S and/or Se are dissolved separately in hydrazine with continuous stirring and afterwards mixed to form precursor inks⁵⁴⁻⁵⁶. N₂ and H₂ gases are released during dissolution. The benefit of this approach is the flexibility to conveniently and precisely modify the CIGS film composition simply by varying the amount of each component solution used. The formed inks can be deposited on substrates by various deposition techniques such as spin casting and dip coating, followed by annealing on a hotplate to get rid of volatile N₂H₄. Due to the weak bond between hydrazine and metal chalcogenides, the obtained CIGS films do not suffer from contamination of solvent and surfactant residues which is a common issue for

many solution-based methods. 15% CIGS solar cells were able to be fabricated with conventional solar cell structure using this method⁵⁷.

Since hydrazine is a highly toxic and flammable species, it is rather hard to transfer this technique to a large-scale industrial production. Effort has been made to find alternative benign solvents with appropriate polar and reducing properties to replace hydrazine. However, no good results have been reported.

2.3.4 Sol-gel and pyrolysis

The sol-gel method is another common technique used in the fields of material science for bulk and thin film preparation. Typical precursors are metal salts and metal alkoxides. Oliveira *et al.*⁵⁸ deposited CIGS films using copper (II) acetate monohydrate, indium (III) acetate and gallium (III) acetylacetonate which were dissolved in ethanol along with complex agent diethanolamine. Kaelin *et al.*⁵⁹ used copper nitrate hemipentahydrate, indium chloride and gallium nitrate hydrate dissolved in methanol with ethylcellulose as binder to fabricate solar cells with 6.7% efficiency. The drawback of this method is the thick carbon layers formed between CIGS films and back contact layers. These impure carbon layers behave as potential recombination centers and barriers for collecting photocurrent. The binder ethylcellulose for modifying the rheology of the inks is the major source of carbon residue. Without binders, some of the coating techniques such as spin coating, doctor blading could result in rough films with serious cracking problems. Spray pyrolysis is one way to deposit CIGS precursor films without binders. The fabrication procedure is

similar to the sol-gel method. During spraying, the substrates were subject to continuous heating which simultaneously transforms the metal precursors to oxides under air or sulfides/selenides with sulfur/selenium precursors in precursor inks. Sulfurization or selenization were utilized to recrystallize the obtained films. However, no working devices were reported by this method.

2.3.5 Film deposition techniques

Solution-based thin film deposition usually requires special tools to process inks to desired thin films. The common thin film deposition tools include spin coating, doctor blading, spray, inkjet printing *etc.*

Spin coating is a very useful thin film deposition technique for semiconductor fabrication. An excess amount of inks is placed on a flat substrates which is then rotated at high speed to spread the fluid by centrifugal force. The film thickness is controlled by rotation speed. The advantages of this method are its easy operation and low equipment cost, while the disadvantages are its low material utilization and non-uniform coating on large substrates.

Doctor blading is a simple technique to deposit thin films on moving substrates at a high production rate. The thickness of films is controlled by the gap size between doctor blades and substrates. Its high production rate and high material utilization could reduce the manufacturing cost.

Spray coating employs a compressed gas to atomize and spray the inks. This technique can be applied to the large area deposition at a relatively high production rate.

Ultrasonics can be used in spray systems to enhance the atomization of inks and improve the film quality.

Inkjet printing uses piezoelectric actuators or thin film heaters to eject inks onto a substrate. The main advantage of inkjet printing is the mask-less patterning that lowers the cost of fabrication and simplifies the process of patterning compared with other patterning techniques.

2.3.6 Comparisons between non-vacuum techniques

In this work, the precursor inks for CIGS films were formed by directly dissolving copper, indium and gallium salts in alcohol solvents (see chapter 3 for more details). Figure 2.5 shows a comparison between the metal salt ink approach and the nanoparticle approaches. Compared to the metal salt ink approach used in this work, nanoparticle routes usually require more steps including nanoparticle synthesis, washing and grinding to prepare nanoparticle inks or pastes for film deposition. Most of precursor nanoparticles for CIGS in literature are synthesized using metal chlorides^{37, 41}, acetates⁶⁰ or acetylacetonates^{3, 36, 39, 40} as starting materials which are the same chemicals used in our metal salt inks. Large amount of metal precursors were wasted during synthesis and washing steps. The synthesis and grinding of nanoparticle are much more time-consuming and power-wasting compared to the simple dissolution of metal salts. These limited factors undoubtedly make the cost of

nanoparticle approaches much higher than our route. Moreover, long carbon binders are also used to formulate nanoparticle inks in order to achieve proper rheological properties, which left large amount of amorphous carbon in final CIGS films and potentially downgraded solar cell performance.

As was mentioned in section 2.3.3, dissolving metal chalcogenides in hydrazine is the most efficient solution-based method to synthesize high-quality CIGS films in terms of purity of material, simplicity of processing and solar cell performance. However, it suffers from serious safety issues which impede its wide application in large-volume production. Hydrazine is highly toxic and flammable liquid which has to be handled in an inert gas environment. No doubt the instability of hydrazine increases the cost of the fabrication of CIGS solar cells. In comparison, the metal salts route employed in this work uses benign alcohols as solvents which leave fewer fingerprints in environment. In addition, the high stability of our metal salt inks with oxygen and moisture do not require protection environment and dramatically reduce the manufacture cost.

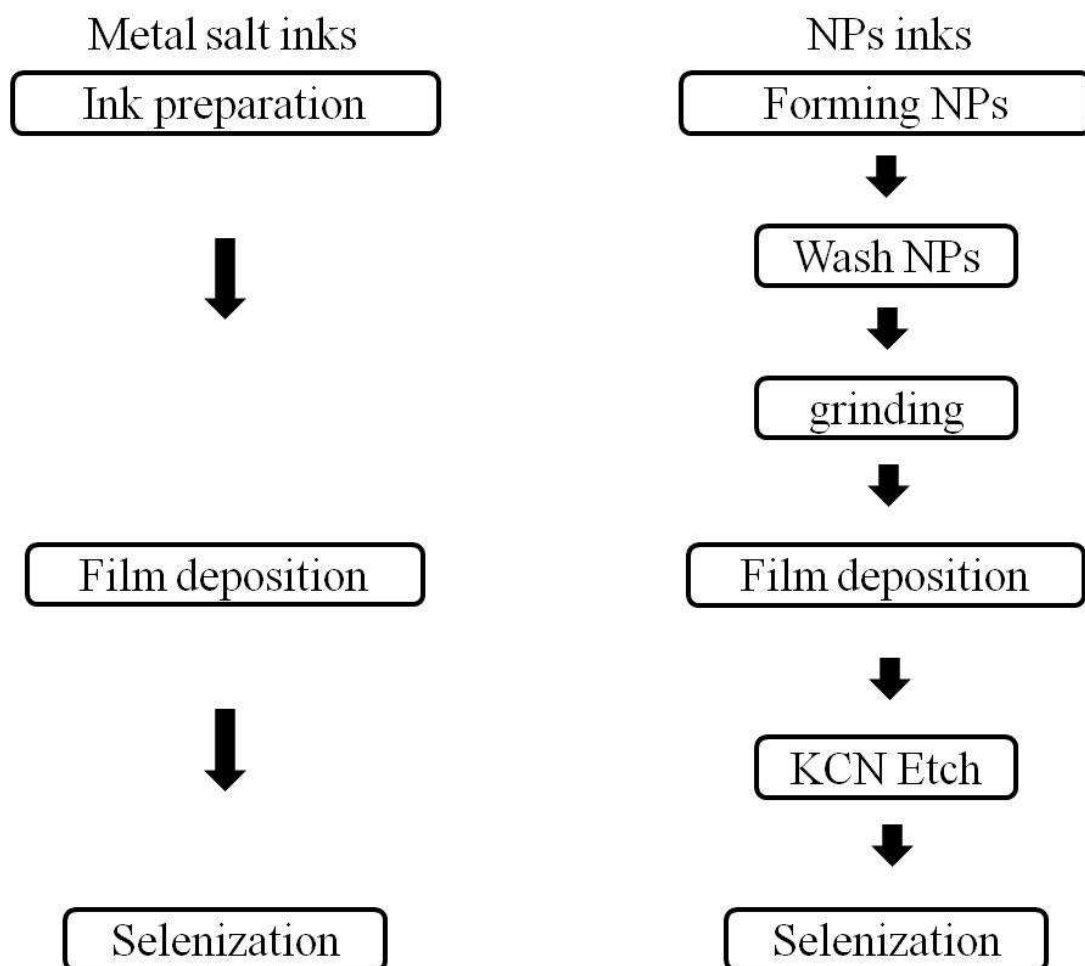


Figure 2.5 Comparison between the metal salt route and nanoparticle route.

2.4 Solar cells

From semiconductor device point of view, solar cells are photodiodes which generate electrical power under illumination. The generated current from solar cells is the superimposed mixture of diode current and photocurrent injected from sunlight. In order to fully understand the working mechanism of solar cells, it is necessary to be familiar with the electrical properties of diodes at first.

2.4.1 Current-voltage characteristics of diodes

Two kinds of carrier flows exist in p-n junction diodes: diffusion and drift. Figure 2.6(a) shows a p-n junction energy band diagram, carrier distributions and carrier activity in the near vicinity of the depletion region under equilibrium (external bias $V_a=0$)⁶¹. The black dots and hollow circles in the figure represent free electrons and holes respectively while the pyramid-like arrangement of dots and circles represents roughly the exponential increase in carrier populations as one is closer to the band edges. On the quasineutral n-side of the junction there are high concentration of electrons and a small number of holes. Due to the higher electron population in the conduction band on the n-side than that on p-side, some of the high-energy electrons will diffuse from n-side to p-side which constitutes the electron diffusion current. The electrons on the p-side have very small population and higher electric potential than electrons on the n-side. Therefore some of the electrons on the p-side will be swept over to the other side of the junction by electric field, which constitute the electron drift current. Naturally, the electron drift current precisely balances the

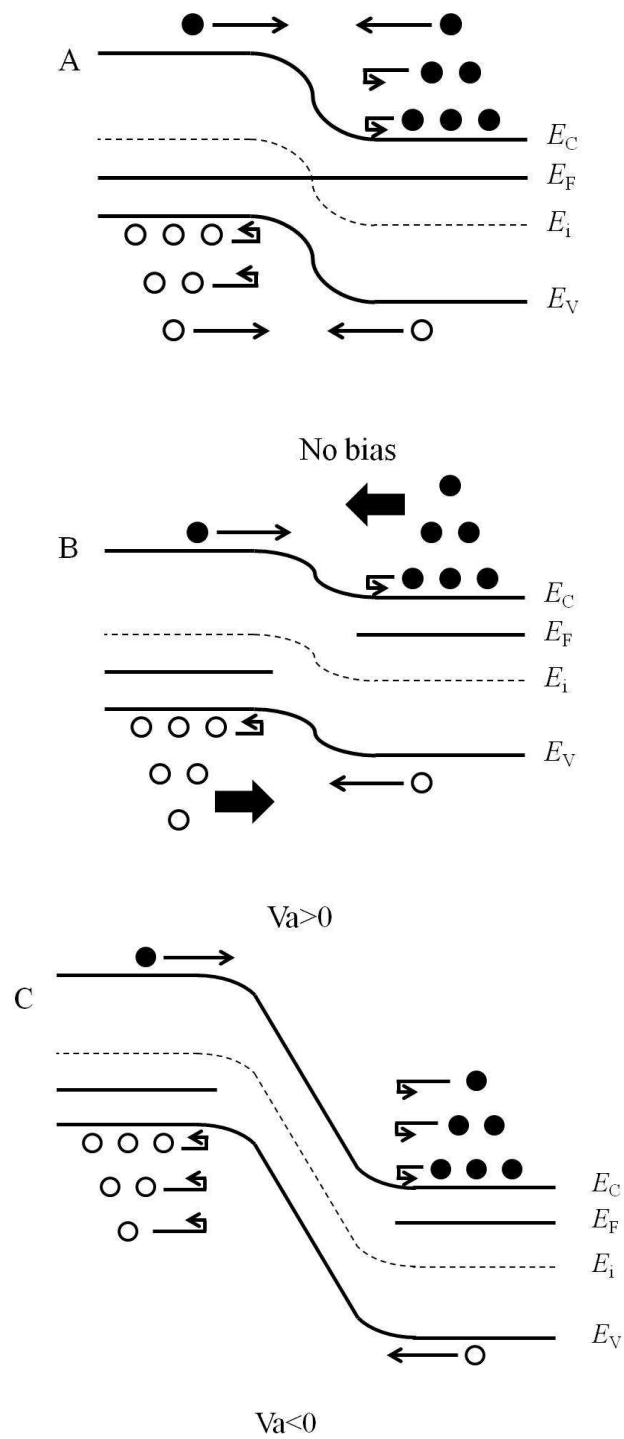


Figure 2.6 P-N junction energy band diagram for (a) $V_a=0V$, (b) $V_a>0$, (c) $V_a<0$.

electron diffusion current at equilibrium conditions. The holes in the p-n junction have analogous movements. the electric potential on p-side of junction decreases under forward bias (see figure 2.6 (b), $V_a > 0$). As a result more electrons on the n-side and holes on the p-sides will diffuse to the opposite side of the junction. The drift currents of minority carriers remain unchanged. The total forward current flowing in the junction increases exponentially with applied bias. Figure 2.6(c) shows the energy band diagram under a reverse bias situation. Reverse bias raises up the potential barrier in the junction thus reduces the majority carrier diffusion currents to a negligible level. The minority carrier drift currents remain the same. Therefore the total current in the p-n junction becomes saturated under a reserve bias⁶¹.

In quasineutral regions of the p-n junctions, the flow of minority carriers is predominated by diffusion⁶². The equations below describe the hole current density in the n-side quasineutral region and the electron current in the p-side quasineutral region.

$$J_h = -qD_h \frac{dp}{dx} \text{ (hole current in n-side quasineutral region)}$$

$$J_e = -qD_e \frac{dn}{dx} \text{ (electron current in p-side quasineutral region)}$$

where q is elementary charge, D_h and D_e are diffusion constants for holes and electrons, and p and n are hole and electron density.

Combining with continuity equations and proper boundary conditions, the above equations can be solved⁶². Figure 2.7 shows the minority, majority, and total current

densities in the diode without considering the recombination in the depletion region.

The total current has a formula as

$$J_{total} = J_0 \left(e^{\frac{qV}{kT}} - 1 \right)$$

$$J_0 = \left(\frac{qD_e n_{p0}}{L_e} + \frac{qD_h p_{n0}}{L_h} \right) = \left(\frac{qD_e n_i^2}{L_e N_A} + \frac{qD_h n_i^2}{L_h N_D} \right)$$

where J_0 is the saturation current density, n_{p0} is the electron density at the depletion edge on the p-side of the junction, p_{n0} is the hole density at the depletion edge on the n-side of the junction, L_e and L_h are electron and hole diffusion lengths, V is bias voltage, k is Boltzmann constant, T is temperature, n_i is intrinsic carrier concentration, N_A is acceptor density on the p-side and N_D is donor density on the n-side.

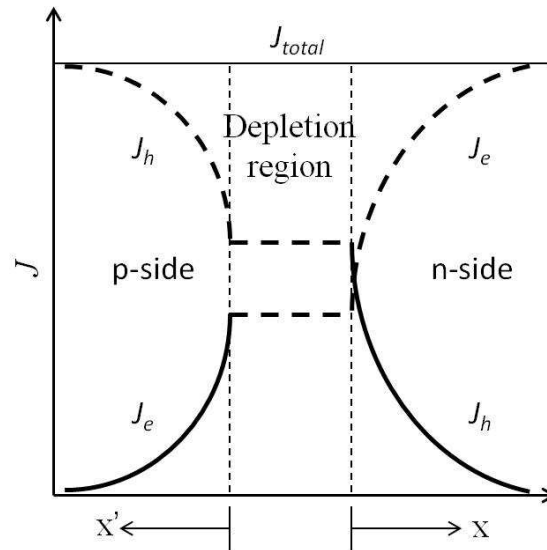


Figure 2.7 Current density profiles in a p-n junction diode.

2.4.2 Ideal solar cells under illumination

When solar cells are exposed to illumination, photons are absorbed in the p-n junction where electron-hole pairs are generated by exciting electrons in the valence band to the conduction band. The generated electrons and holes are separated by the n-side and p-side of the junction forming photo currents simultaneously. In order to simplify the mathematical model of solar cells under illumination, it is assumed that the generation rate of electron-hole pairs by illumination is uniform throughout the device⁶². The obtained current out of solar cells under illumination is simply the superimposed mixture of diode current and a constant photocurrent (J_L) (see equation below).

$$J = J_0 \left(e^{\frac{qV}{kT}} - 1 \right) - J_L$$

$$J_L = qG(L_e + W + L_h)$$

where G is the generation rate of electron-hole pairs and W is the width of depletion region.

Note that the photocurrent J_L has a value equal to the generated carriers by light in the depletion region of the diode and a minority carrier diffusion length on either side⁶². Therefore it is straightforward to conclude that longer minority carrier lifetimes and wider depletion width can generate more photocurrent.

Current-voltage characteristics of solar cells in both the dark and under illumination are illustrated in figure 2.8. Several parameters are used to characterize solar cell

outputs. The first one is the short-circuit current density J_{sc} which is the intersection of illuminated J-V curve and y-axis and equal to the photocurrent J_L . This describes the maximum current extracted from solar cells. The second parameter is the open-circuit voltage V_{oc} which is the intersection of illuminated J-V curve and x-axis. From equation above, setting J to zero gives:

$$V_{oc} = \frac{kT}{q} \ln \left(\frac{J_L}{J_0} + 1 \right)$$

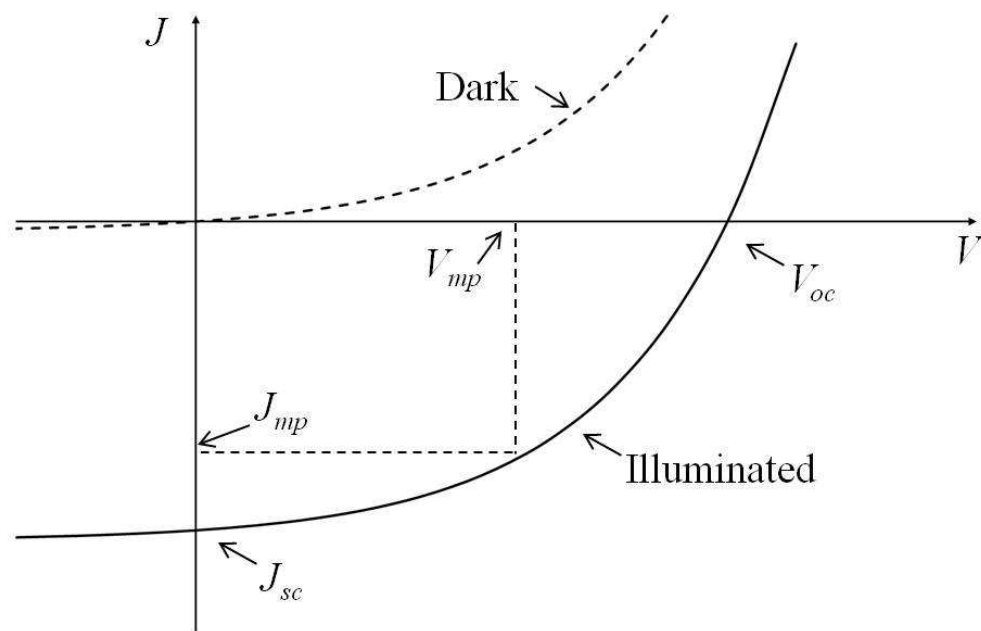


Figure 2.8 J-V characteristics of solar cells.

The maximum power output for the illuminated solar cells is equal to the product of V_{mp} and J_{mp} . Both of them can be determined by calculating the power of each operating points in the graph.

The fill factor, FF , is defined as equation below which a measure of how ‘square’ the output characteristics are⁶².

$$FF = \frac{V_{mp} J_{mp}}{V_{oc} J_{oc}}$$

The most important parameter, energy-conversion efficiency, η , is given by

$$\eta = \frac{V_{mp} J_{mp}}{P_{in}} = \frac{V_{oc} J_{sc} FF}{P_{in}}$$

where P_{in} is the total power of the light incident on the cell.

2.4.3 Non-ideal solar cells

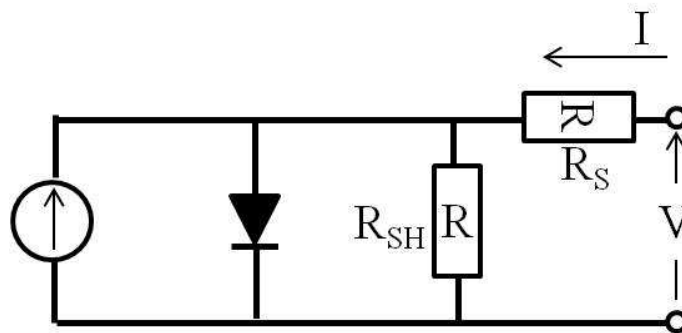


Figure 2.9 The equivalent circuit of a non-ideal solar cell.

The model described in the previous section is based on the assumption that the p-n junction of solar cells is in an ideal open. The real solar cells have several non-ideal issues such as grain boundary and defects in devices. In order to characterize solar

cells more precisely, an equivalent circuit containing series resistance R_S and shunt resistance R_{SH} is usually employed to describe the diode performance (see figure 2.9).

There are several reasons responsible for these resistances. The major causes of the series resistance are the bulk resistance of the semiconductor materials, the bulk resistance of the metallic contacts and interconnections, and the contact resistance between the metallic contacts and the semiconductor⁶². The shunt resistance is influenced by the leakage across the p-n junction via crystal defects and impurities⁶². High series resistance and low shunt resistance can reduce V_{oc} and J_{sc} . Based on the equivalent circuit, the current-voltage relation can be inferred as⁶³

$$J = J_0 \left(e^{\frac{q(V - JR_S)}{AkT}} - 1 \right) + \frac{V - JR_S}{R_{SH}} - J_L$$

where A is diode quality factor.

The saturated current density J_0 may be written in the form¹⁴

$$J_0 = J_{00} e^{\left(\frac{-E_a}{AkT} \right)}$$

where E_a is the activation energy and the prefactor J_{00} is only weakly temperature dependent. The activation energy E_a is equal to the absorber band gap energy E_g for recombination happening at the back surface, in the quasineutral region, and in the space charge region whereas E_a is smaller than E_g for interface recombination¹⁴. The diode quality factor A is equal to 1 for recombination at back surface, in the

quasineutral region, and at the absorber/buffer interface, whereas for space charge recombination $A = 2$.¹⁴

Chapter 3 Chalcopyrite thin film deposition and device fabrication

3.1 Chalcopyrite thin film deposition by low-cost air-stable metal salt inks

3.1.1 Ink preparation

Table 3.1 Chemical list for recipe A

Chemical name	Formula	Brand	purity
Copper acetate monohydrate	$\text{CuAc}_2 \cdot \text{H}_2\text{O}$	Aldrich	99.99%
Indium acetate	InAc_3	Alfa Aesar	99.99%
Gallium chloride	GaCl_3	Aldrich	99.999%
Ethanol	$\text{C}_2\text{H}_5\text{OH}$	\	200proof
Ethylene glycol	$\text{C}_2\text{H}_4(\text{OH})_2$	Mallinckrodt	>99%
Ethanolamine	$\text{H}_2\text{NC}_2\text{H}_4\text{OH}$	Alfa Aesar	99%

Recipe A

$\text{CuAc}_2 \cdot \text{H}_2\text{O}$ (4 mmol), InAc_3 (2.8 mmol), and GaCl_3 (1.2 mmol) were dissolved in a mixture of ethanol (7 ml), ethylene glycol (2 ml) and ethanolamine (1.5 ml) at room temperature with magnetic stirring for several hours until the ink becomes clear. The viscosity of the ink was adjusted to 5 cP by controlling the ratio of ethylene glycol, which is highly viscous. Table 3.1 shows the chemical list of recipe A.

Table 3.2 Chemical list for recipe B

Chemical name	Formula	Brand	purity
Copper acetate monohydrate	$\text{CuAc}_2 \cdot \text{H}_2\text{O}$	Aldrich	99.99%
Indium acetate	InAc_3	Alfa Aesar	99.99%
Gallium acetylacetonate	GaAcac_3	Aldrich	99.999%
Ethanol	$\text{C}_2\text{H}_5\text{OH}$	\	200proof
Propylene glycol	$\text{C}_3\text{H}_6(\text{OH})_2$	Sigma-Aldrich	>99.8%
Stabilizer A and B	\	\	\

Recipe B

0.7mmol InAc_3 , and 0.3mmol GaAcac_3 were added into a glass vial followed by adding a mixture of 1ml propylene glycol, 2ml ethanol and 1.2ml stabilizer A. The mixture was subjected to a continuous stirring at 60-70°C for 5min. 1mmol $\text{CuAc}_2 \cdot \text{H}_2\text{O}$ was added to the glass vial and stirred continuously at 60-70°C for 20-30min until uniform green slurry was formed. Raise the temperature to 110°C and continue stirring for another 10min. 0.6ml Stabilizer B was added to the glass vial quickly. A clear deep blue solution was formed immediately. Keep stirring the solution at 110°C for 20min, then reduce its temperature to 50°C and keep it constant for 30min. Finally the ink was cooled to room temperature. Table 3.2 shows the chemical list of recipe B.

3.1.2 Thin film deposition

Inkjet printing

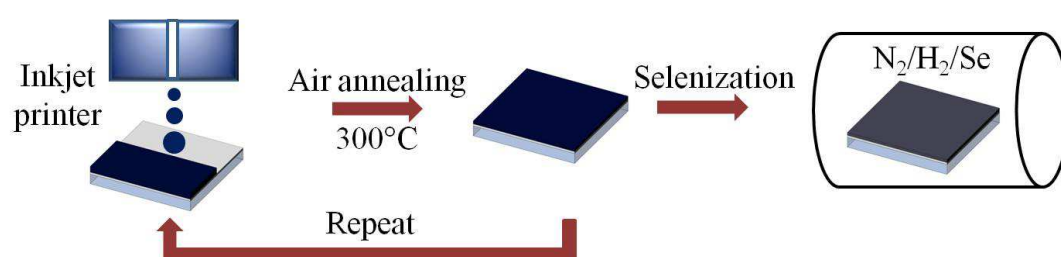


Figure 3.1 Schematic of CIGS film deposition by inkjet printing.

The inkjet printing process is illustrated in figure 3.1. The prepared ink (recipe A) was printed by Dimatix DMP-2800 (See figure 3.2) on molybdenum-coated (200 nm) Corning 1737 substrates, which were annealed on a preheated 300°C hotplate for a

couple of minutes. The printing parameters are drop spacing 25 mm, 6 nozzles, firing voltage 40 V, firing frequency 1 kHz, and 2 passes (about 10 min/pass for 1 in² area). Post-selenization process was utilized to convert the precursor film into a CIGS film with Se vapor from the evaporation of Se powder mixed with 4.2sccm H₂ and 17sccm N₂ in a quartz tube furnace for 20 min at 500°C (ramping rate 20°/min).



Figure 3.2 Dimatix DMP-2800 inkjet printer.

Spin casting

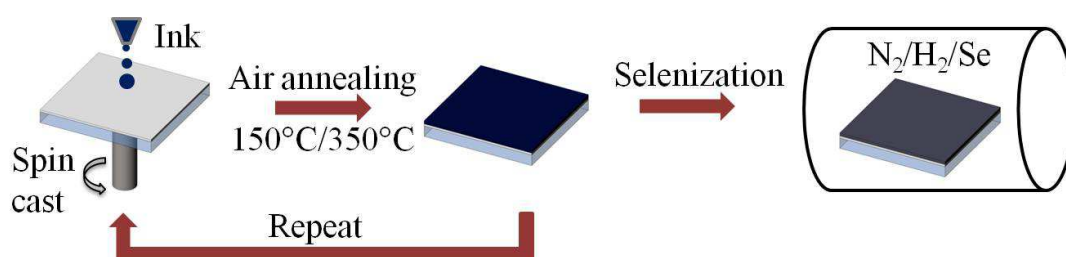


Figure 3.3 Schematic of CIGS film fabrication process by spin casting.

The spin casting process is illustrated in figure 3.3. The prepared ink (recipe B) was spread on 0.75in x 0.75in molybdenum -coated (~500 nm) Corning 1737 substrates which sat on a stationary spin coater chuck. Afterwards the substrate was rotated at 1500 resolution per minute for 70sec. The as-deposited films were softly annealed on a 150°C preheated hotplate for 1min to evaporate the solvents followed by 350°C annealing in a preheated furnace for about 10 minutes to evaporate or decompose all the organic species in the films. Repeat the spin-coating and air-annealing processes for a few times until the desired thickness was achieved. Finally a post-selenization process was utilized to convert the precursor film into CIGS film using Se vapour generated from the evaporation of powder Se mixed with 20% H₂ and 80% N₂ in a 500-530°C quartz tube furnace for 30 min. Usually each cycle can produce 150nm-thick CIGS films.

3.2 Fabrication of CIGS thin film solar cells

3.2.1 Molybdenum back contact deposition

Molybdenum back contact was deposited on Corning 1737 glass by DC magnetic sputtering in AJA sputter system with base pressure of 2×10^{-5} mtorr. Molybdenum target (3 in diameter, 1/4 in thickness, and 99.95% purity) was purchased from Kurt Lesker. The power on target was 400 W. The flow rate of argon was 20 sccm for 20min and decreased to 5sccm for another 20 min. The corresponding pressures in the chamber were 6 mtorr and 1 mtorr respectively.

3.2.2 Absorber formation by selenization

Selenization is the most importance step to transform the obtained raw films to desired CIGS films after air annealing as described in section 2.1.2. The selenization system is illustrated in figure 3.4.

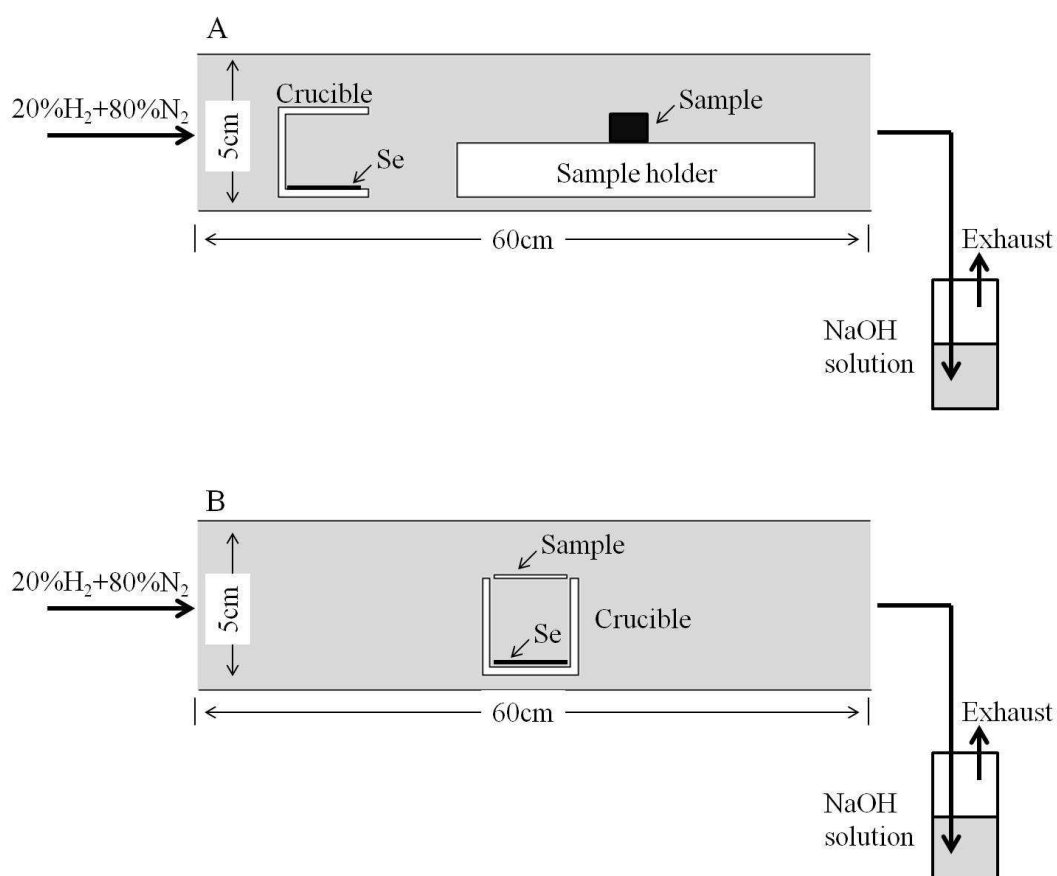


Figure 3.4 Illustration of furnace setups for selenization (a): low selenium vapor pressure, (b): high selenium vapor pressure.

Pure N₂ was purged into a quartz tube at 1L/min flow rate for 1hr after samples were placed in the tubes and before the selenization started. 4.2sccm H₂ and 17sccm N₂

controlled by mass flow controllers were flowed into the quartz tube for 5hr before selenization. Selenium powder was stored in a crucible.

During selenization, the quartz tube was heated up to 500-530°C at a rate of 20°C/min and held at 500-500°C for 30min. Selenium was evaporated and reacted with raw films. Two sets of configurations (low Se vapor pressure and high Se vapor pressure) were used to control the selenium vapor pressure on top of sample surface. In the setup of low selenium pressure, samples were held by a sample holder with raw film surface parallel to the direction of gas flow. In the setup of high selenium pressure, samples sat on top of a crucible with raw film surface facing down.

After selenization finished, the furnace was cooled down overnight with a continuous flow of H_2 and N_2 mixture. When the furnace was at room temperature, pure N_2 was purged into the quartz tube to evacuate selenium source gas in the chamber.

The reaction involved in CIGS formation is present in figure 3.5. Metal salts dissolved in volatile alcohol solvents were deposited on substrate with modestly heat. The resulted films reacted with selenium and hydrogen through substitution reactions.

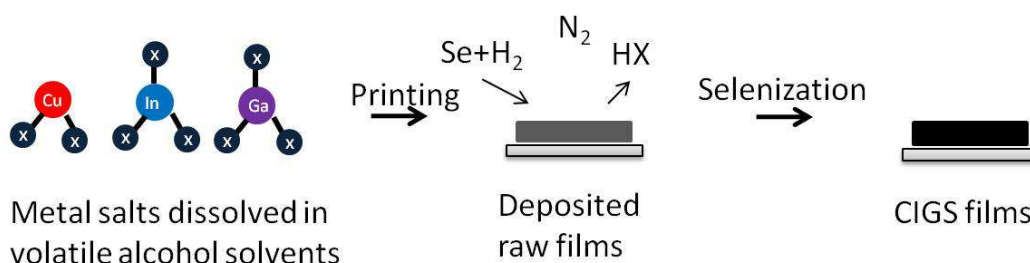


Figure 3.5 Schematic of selenization reactions.

3.2.3 CdS buffer layer deposition

Chemical bath deposition (CBD)

Table 3.3 Chemical list for CBD

Chemical name	Formula	Brand	purity
Cadmium sulfate hydrate	$\text{CdSO}_4 \cdot 8/3\text{H}_2\text{O}$	Alfa Aesar	99.996%
Thiourea	$\text{CH}_4\text{N}_2\text{S}$	Aldrich	99%
Ammonia	$\text{NH}_3 \cdot \text{H}_2\text{O}$	Mallinckrodt	28.0%-30.0%

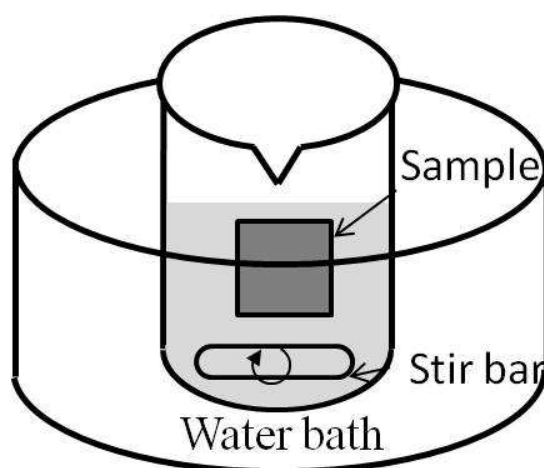


Figure 3.6 Schematic of CdS deposition by chemical bath deposition.

The setup of CdS deposition by CBD is illustrated in figure 3.6. 0.0288g

$\text{CdSO}_4 \cdot 8/3\text{H}_2\text{O}$ and 0.4281g thiourea were separately dissolved in 15ml DI water with the assistance of an ultrasonicator. Sample substrates were placed in a 100ml baker which was filled with 37.5ml DI water, 9.8ml 28%-30% ammonia solution, and freshly prepared CdSO_4 and thiourea solutions. The beaker was modestly stirred by a magnetic bar and put into water bath where temperature was kept around 68°C - 70°C . The solution inside the beaker started to turn yellowish after 3-4min and form CdS

particles after 6-7min. The deposition lasted for 6min. Afterwards the samples were rinsed with DI water and dried at room temperature. After the samples were dried out, they were annealed at 200°C in air for 2min.

Continuous flow deposition (CFD)

Table 3.4 Chemical list for CFD

Chemical name	Formula	Brand	purity
Cadmium sulfate hydrate	$\text{CdSO}_4 \cdot 8/3\text{H}_2\text{O}$	Alfa Aesar	99.996%
Thiourea	$\text{CH}_4\text{N}_2\text{S}$	Aldrich	99%
Ammonia	$\text{NH}_3 \cdot \text{H}_2\text{O}$	Mallinckrodt	28.0%-30.0%
Ammonia sulfate	$(\text{NH}_4)_2\text{SO}_4$	Alfa Aesar	99.0%

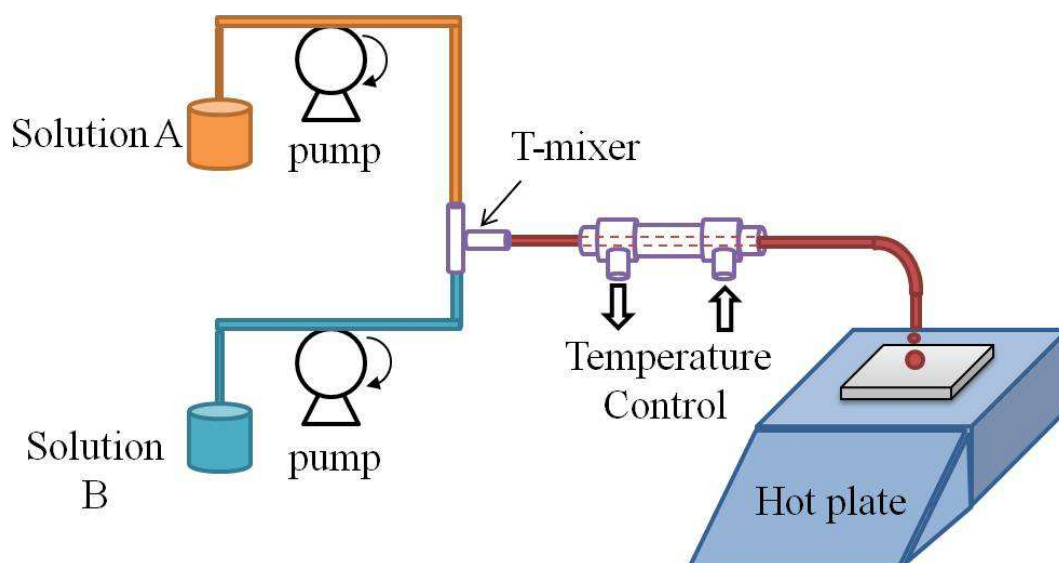


Figure 3.7 Schematic of CdS deposition by continuous flow deposition.

A schematic of continuous flow deposition is illustrated in figure 3.7. Stock solution A was formed by mixing 2.052g $\text{CdSO}_4 \cdot 8/3\text{H}_2\text{O}$, 1.057g ammonia sulfate and 22ml 28%-30% ammonia solution in 78ml DI water while stock solution B contained

0.609g thiourea in 100ml DI water. Flows of solution A and B were pumped by peristaltic pumps at 0.5ml/min and mixed via a T-mixer. The mixed solution flowing out of T-mixer was heated up to 80°C by a constant temperature water circulator and dropped on substrates which were preheated to 90°C on a hotplate. The deposition lasted for 7 to 10min. Afterwards the samples were rinsed with DI water and dried at room temperature. After the samples were dried out, they were annealed at 200°C in air for 2min.

3.2.4 Window layer deposition

The window layer contains two parts: a 50nm thick intrinsic ZnO and a 300nm thick 2% aluminum-doped ZnO. Both films were deposited by RF magnetron sputtering using an AJA sputter system with a base pressure of 5×10^{-6} mtorr. Both targets (3 in diameter, ¼ in thickness, and 99.99% purity) were purchased from Semiconductor Wafer Inc. The power for the deposition of ZnO and Al:ZnO targets were 90 W and 120 W respectively. The oxygen and argon gas flow rates for the deposition of intrinsic ZnO films were 2sccm and 18sccm respectively. The corresponding pressure in the chamber was 6mtorr. 5 sccm argon gas flow at 1 mtorr was used for the deposition of Al:ZnO films.

3.2.5 Al top contact deposition

Polaron thermal evaporation system was used to deposit Al top contact. The base pressure during Al evaporation was 4×10^{-4} Pa. A stainless steel shadow mask was used

to pattern the dimension of top contacts (see figure 3.8 for details of mask). The dimension of individual solar cells is 3mm x 3mm.

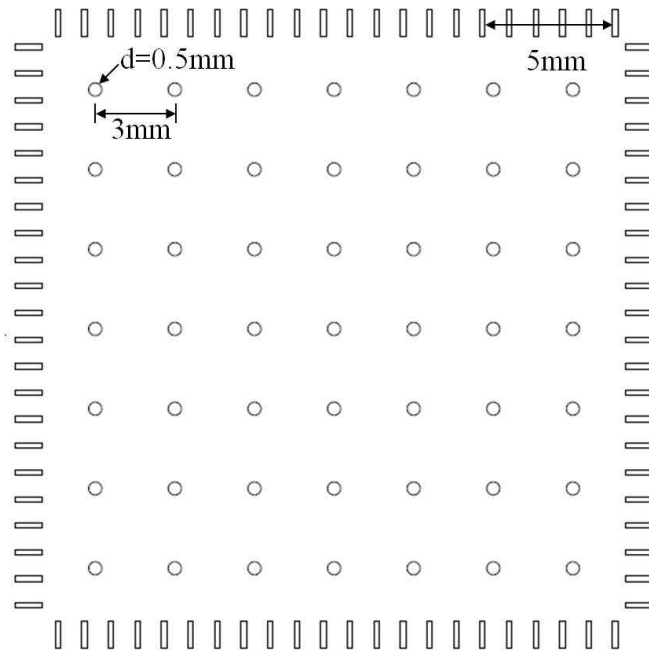


Figure 3.8 Mask pattern for Al evaporation.

Chapter 4 Results

Thermal Gravimetric analysis (TGA) was conducted using TA Q600. Elemental composition was analyzed using a Cameca SX-100 Electron Microprobe (wavelength dispersive X-ray spectroscopy). Powder X-ray diffraction (XRD) spectra was collected using a Bruker D8 Discover Diffractometer. Witec Confocal Raman microscope with a tunable Argon ion laser at 514nm was used to collect the Raman spectra. SEM and TEM images were taken using a FEI Quanta 3D Dual Beam Scanning Electron Microscopy (SEM) and JEOL JEM-ARM200F Transmission Electron Microscopy (TEM). Oriel 96000 Full spectrum solar simulator calibrated with a standard Si solar cell and Newport radiant power meter and PVIV-200 test station were used to analyze the device performance. Quantum Efficiency was measured by a Tau Science Flash QE system.

4.1 Characterization of materials

4.1.1 Molybdenum back contact

Two kinds of thickness of molybdenum back contacts were used in the fabrication of device: 100nm and 100nm+500nm. 100nm thick Mo films on Corning 1737 glass were provided by Sharp Laboratory of America. In order to increase the conductivity of Mo back contacts, extra 500nm Mo films were deposition on top of 100nm Mo films by DC magnetic sputtering process described in section 3.2.1.

The sheet resistances of different Mo films were measured by van der Pauw method (see figure 4.1). Four small ohmic contacts were placed at the corners of a rectangular thin-film sample. To determine the sheet resistance R_S of thin films, two characteristic resistances R_A and R_B associated with the corresponding terminals shown in figure 4.1 were measured. R_A and R_B were related to the sheet resistance through the van der Pauw equation $\exp(-\pi R_A/R_S) + \exp(-\pi R_B/R_S) = 1$, which were solved numerically for R_S . The sheet resistances for 100nm and 100nm+500nm Mo films were $54\Omega/\text{sq}$ and $7\Omega/\text{sq}$.

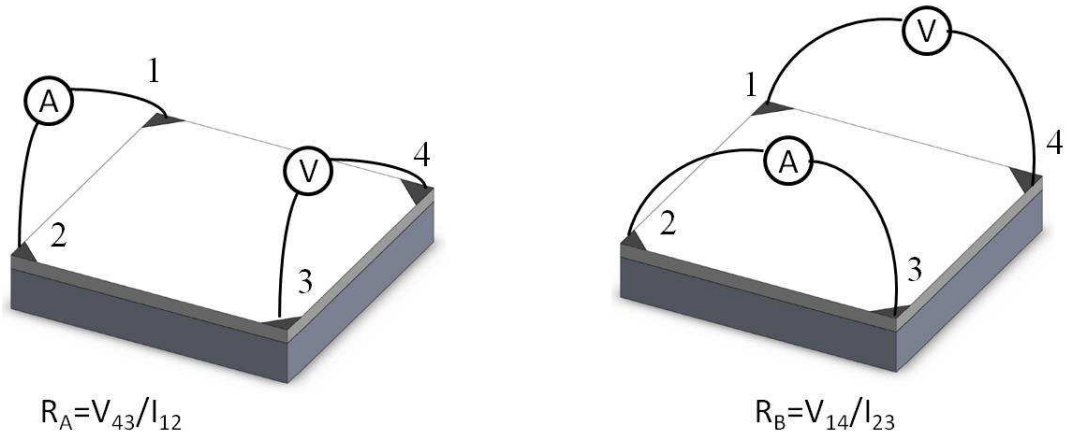


Figure 4.1 Illustration of van der Pauw method for sheet resistance measurement.

4.1.2 Absorber films

In this section, the characterizations of CIGS films produced from recipe A and recipe B are presented. Further discussions related to the influence of absorber films on device performance are presented in chapter 5.

4.1.2.1. Thermal gravimetric analysis (TGA)

Recipe A

Thermal gravimetric analysis was used to analyze the ink weight loss during air annealing (see figure 4.2). Below 100°C, the weight loss was due to the evaporation of ethanol. The ethylene glycol started to evaporate from the film until about 200°C. Ethanolamine in solution was evaporated along with the evaporation of ethylene glycol. After 200°C, anions in solution started to slowly decompose or evaporate. The final weight percentage after 500°C was about 14%. If we assume all the organic species were evaporated or decomposed and all the metal salts reacted with oxygen to form metal oxides, the remaining weight percentage was about 7% which is much lower than the experimental data. Therefore in addition to the transformation of metal

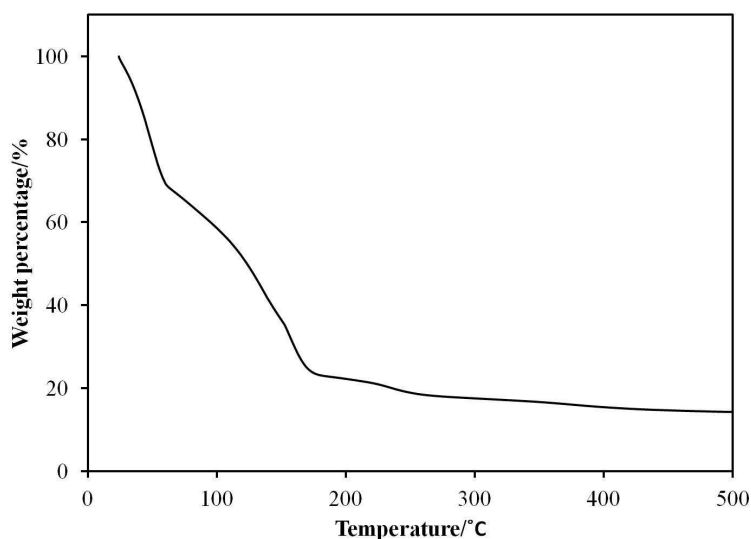


Figure 4.2 TGA result for the ink using recipe A.

oxides from metal salts, there are considerable amount of organic species remaining in the final CIGS films.

Recipe B

In order to form a dense precursor film, after each spin casting, the solvents and anions were removed by thermal evaporation and decomposed by air annealing, respectively. Thermal gravimetric analysis was used to analyze the ink weight loss and the decomposition of metal acetates/acetylacetonate precursor during annealing (see figure 4.3). Pure copper acetate monohydrate lost water at 120°C and completely decomposed at 267°C where the remaining weight was 36.28% of the initial mass indicating the formation of Cu₂O. After this point, the weight of copper precursor actually increased to 40.77% of the initial mass due to the transformation of Cu₂O to CuO. This transformation of $\text{Cu}^{2+} \rightarrow \text{Cu}^{1+} \rightarrow \text{Cu}^{2+}$ for copper acetate under air annealing is consistent with the reported results in literature^{64, 65}. Pure indium acetate completely decomposed at 300°C with 52% remaining weight, whereas gallium acetylacetonate sublimed around 200°C. The TGA curve of a formulated ink composed of these three metal salts and solvents shows a major weight loss due to the evaporation of solvents before 100°C and anion decomposition before 350°C. This result indicates 350°C air annealing after each cycle of spin casting is high enough to remove almost all the organic species in the precursor film without amorphous carbon residue, which was confirmed by the Raman spectrum as well. The results of wavelength dispersive X-ray spectroscopy revealed that the gallium atomic percent decreased from 30% in

precursor films to about 24% after selenization, which was likely resulting from the sublimation of gallium acetylacetonate.

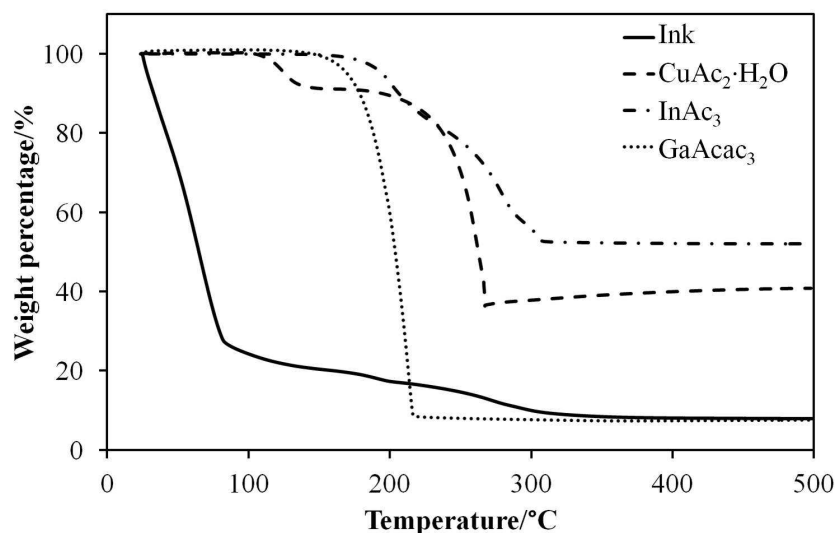


Figure 4.3 TGA results for copper acetate, indium acetate, gallium acetylacetonate and the ink using recipe B.

4.1.2.2. X-ray diffraction

Recipe A

Recipe A was used to produce both CuInSe₂ and CuInGaSe₂ films. CIGS films contained 30% Gallium. X-ray diffraction was used to identify chemical compositions in both films (see figure 4.4). Both films showed (112) dominant orientation over other orientations. The CIS film matched well with XRD reference from data base JCPDS (87-2265). The Ga incorporated CIGS film showed peak shift to higher 2theta value for all the orientations, which resulted from the reduced lattice spaces due to smaller diameter of gallium atoms compared to indium atoms. One can note that the

XRD peaks of CIGS films become broader than CIS films, which was due to the reduced crystal size in CIGS films mainly resulting from gallium incorporation. In addition to CIS or CIGS phases, MoSe_2 and Mo were also detected.

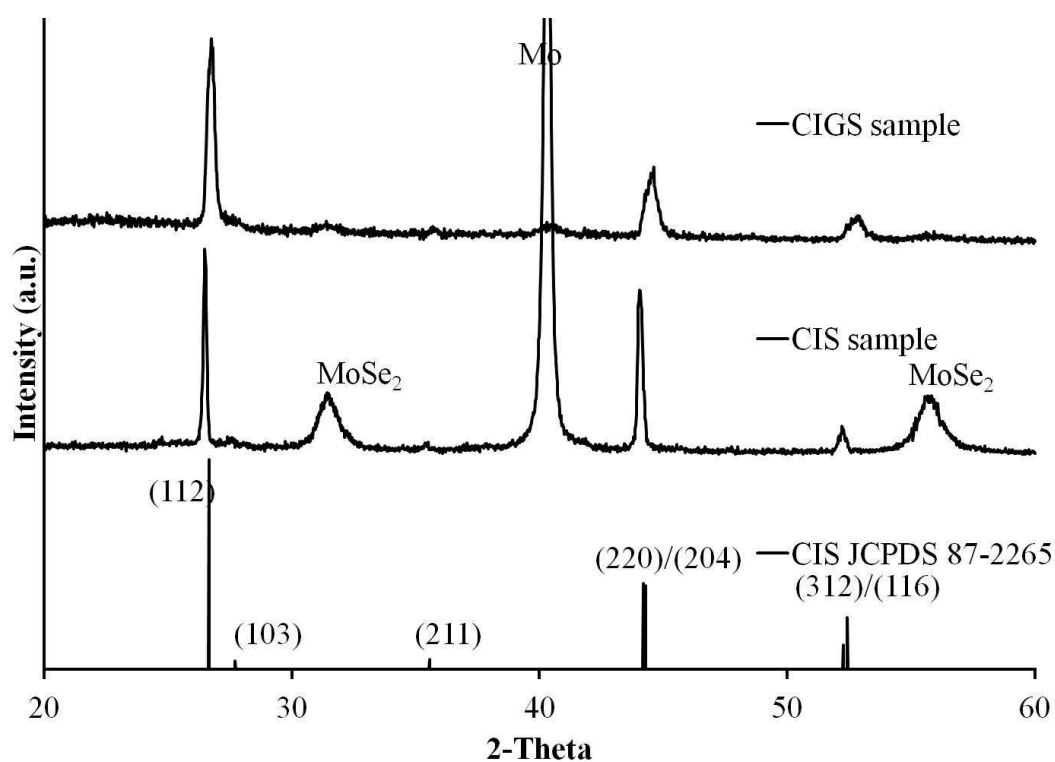


Figure 4.4 X-ray diffraction of CIS and CIGS films made from recipe A.

The XRD spectra of CIS films selenized at different temperatures (see figure 4.5) were used to understand the evolution of CuInSe_2 film formation process. The air-annealed precursor films show peaks that could be identified with the indium oxide and copper oxide phases. However, only a portion of the metal salts were transformed to metal

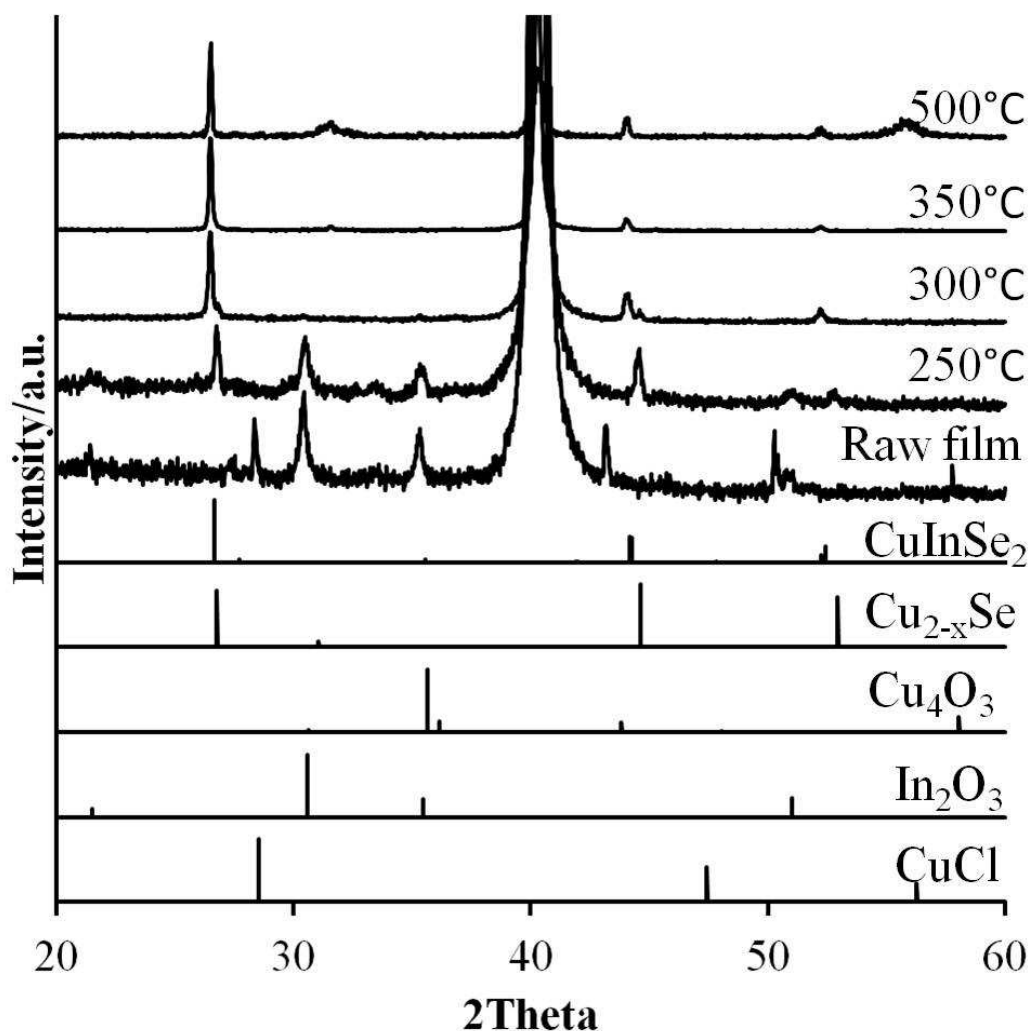


Figure 4.5 X-ray diffraction of CIS films made from recipe A at different selenization temperatures. JCPDS #: CuInSe₂ (87-2265), Cu_{2-x}Se (06-0680), Cu₄O₃ (83-1665), In₂O₃ (88-2160) and CuCl (06-0344).

oxides after annealing in air since there was still considerable amount of chlorine existing in films according to the energy dispersive X-ray spectroscopy (EDX) result and the CuCl peak in figure 4.5. After the selenization process at 250°C, peaks from the Cu_{2-x}Se phase appeared. As the annealing temperature increased, peaks from

chalcopyrite CIS phase appeared along with the decreasing peaks of Cu_{2-x}Se and the disappearing of oxide peaks. The peaks from Cu_{2-x}Se phase disappeared after 350°C . A similar trend was observed for the synthesis of CIGS as well.

Recipe B

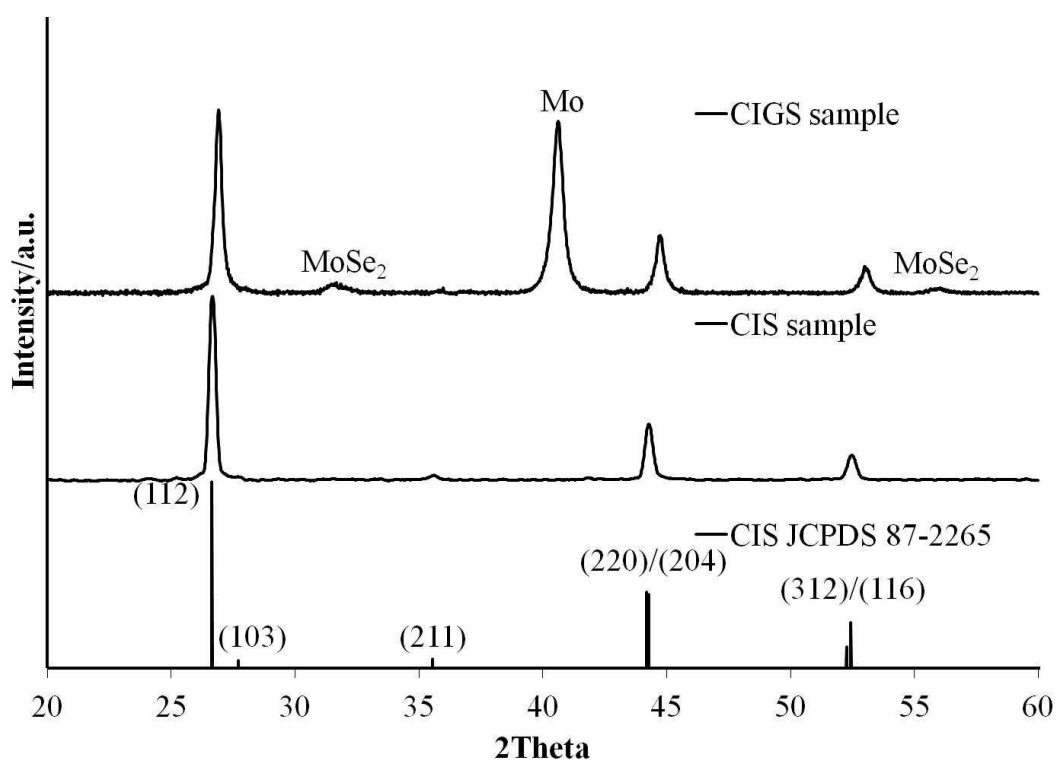


Figure 4.6 X-Ray diffraction of CIS and CIGS films made from recipe B.

X-ray diffraction patterns of CuInSe_2 and CuInGaSe_2 synthesized from recipe B are presented in figure 4.6. According to the XRD spectra, it is clearly shown that polycrystalline CIS and CIGS films were successfully formed without the co-existence of other phases, such as Cu_{2-x}Se . The shift of the $(220)/(204)$ XRD peaks after the

addition of gallium indicates the successfully incorporation of gallium into the chalcopyrite lattice⁵⁵.

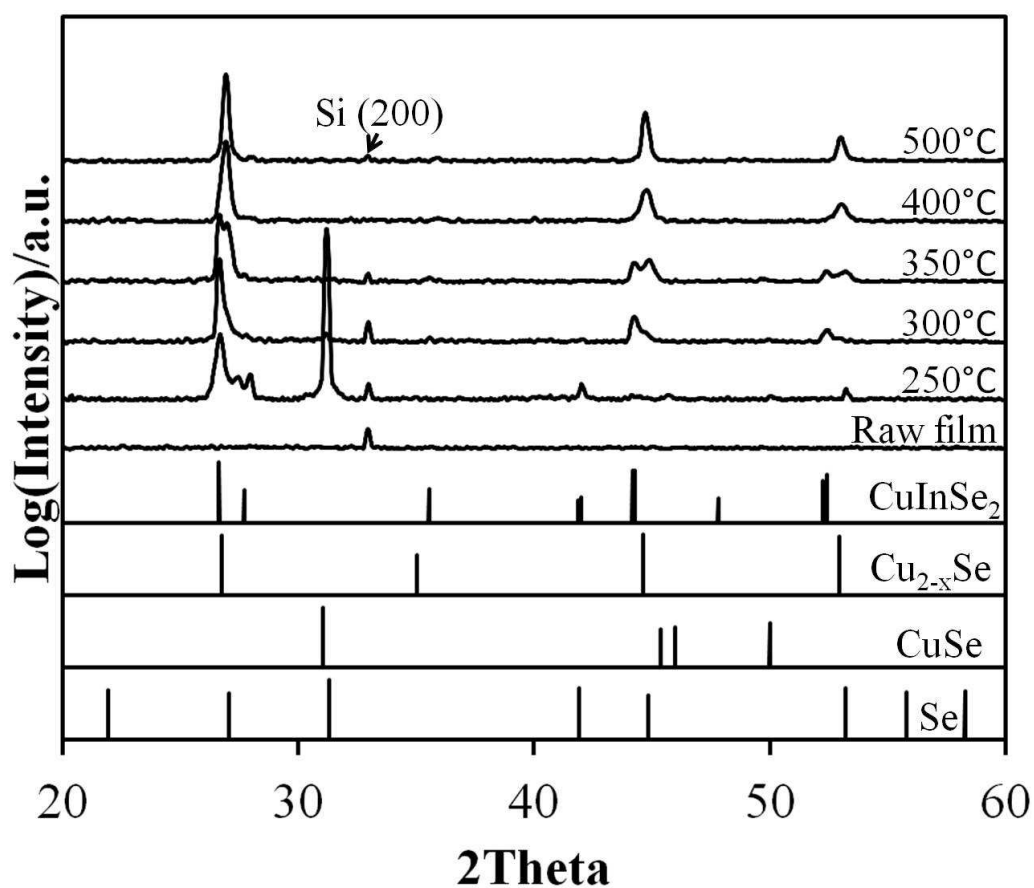


Figure 4.7 X-ray diffraction of CIS films made from recipe B at different selenization temperatures. JCPDS #: CuInSe₂ (87-2265), Cu_{2-x}Se (06-0680), CuSe (49-1457), and Se (51-1389).

X-Ray diffraction was used to determine the phase of CIGS films on silicon substrates after different selenization temperatures (see figure 4.7). The precursor films after 350°C air annealing were amorphous as indicated by the flat XRD spectrum. After

selenization at 250°C, Cu_{2-x}Se and CuSe phases were formed with elemental Se according to XRD. At an annealing temperature higher than 300°C, peaks from Cu_{2-x}Se and CuSe disappear. Instead peaks from CuInSe_2 phase could be identified from XRD. Small bumps at the right shoulders of peaks with 2θ around 26.69°, 44.26° and 52.45° were observed in the XRD spectrum. This indicates the incorporation of gallium into the ternary CIS phase and forms the quaternary CIGS phase.

When annealing temperature increased to 350°C, the intensities of XRD peaks of CIGS phase increased significantly along with the intensities of peaks of CIS phase decreasing. Peaks of CIS phase disappeared in the XRD spectrum while only peaks of CIGS phase could be found after 400°C annealing. The peaks of CIGS phases become narrower which indicated the formation of films with better crystallinity.

4.1.2.3. Raman spectrum

Recipe A

The Raman spectrum was also utilized to identify the secondary phases and to verify the purity of chalcopyrite CIS phase (see figure 4.8). A peak at 174 cm^{-1} , associated with the “A1” mode of lattice vibration for the chalcopyrite structures, appeared after the selenization process⁶⁶⁻⁶⁸. The absence of other Raman peaks indicates the purity of the CIS phase. In contrast, most of CIS films fabricated by solution-based approaches suffer from contamination of binary chalcogenides which require an extra KCN etching step.

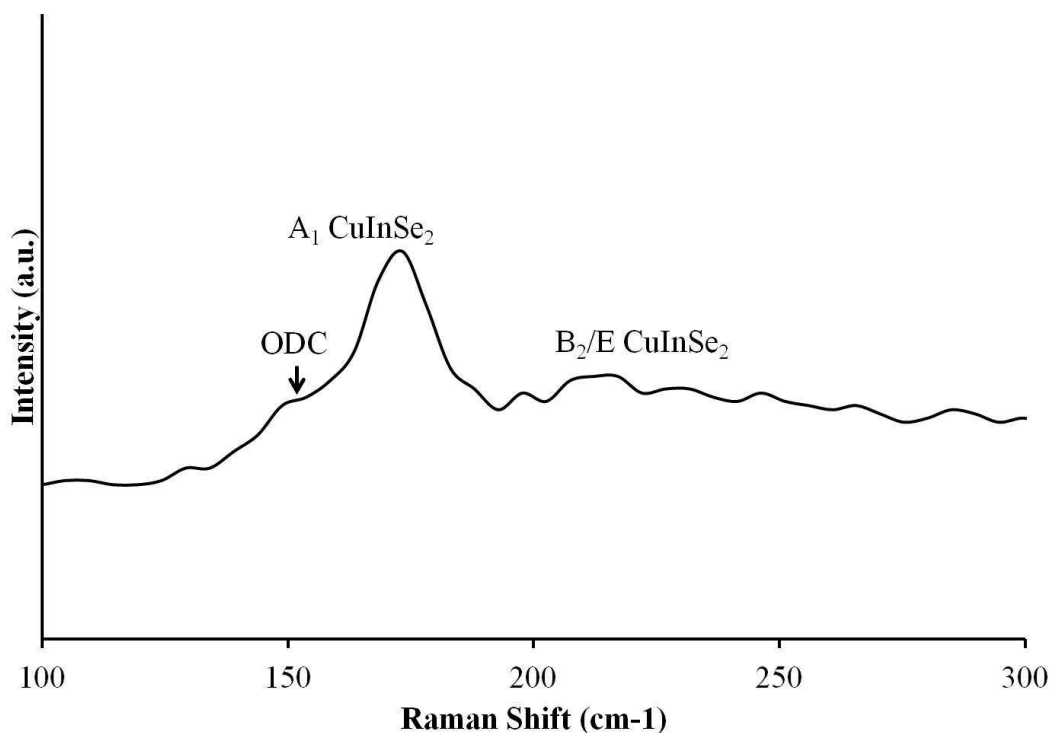


Figure 4.8 Raman spectrum of CIS films made from recipe A.

Recipe B

To resolve the potential overlapping of XRD signals for CIS and Cu_{2-x}Se , Raman spectroscopy was usually utilized to distinguish these two phases. Figure 4.9 shows Raman spectra of CIGS films selenized at different temperatures. Raman spectrum of the film after selenization at 250°C does not have a peak at 173cm^{-1} which indicates the absence of CIS phase. The spectrum show a peak at 257cm^{-1} which could come from a mixture of copper selenide and selenium. At an annealing temperature higher than 300°C , peaks from Cu_{2-x}Se and CuSe disappear from the Raman spectrum. Instead peaks from CuInSe_2 phase could be identified from Raman spectra. When

annealing temperature increased to 350°C, in the Raman spectrum A_1 peak of CIS phase at 173cm^{-1} shifted to 176cm^{-1} indicating the domination of CIGS phase. Moreover, small shoulders at peaks around 150cm^{-1} were contributed to the formation of ordered defect compounds (ODC) which is beneficial for the CIGS solar cells¹⁹.

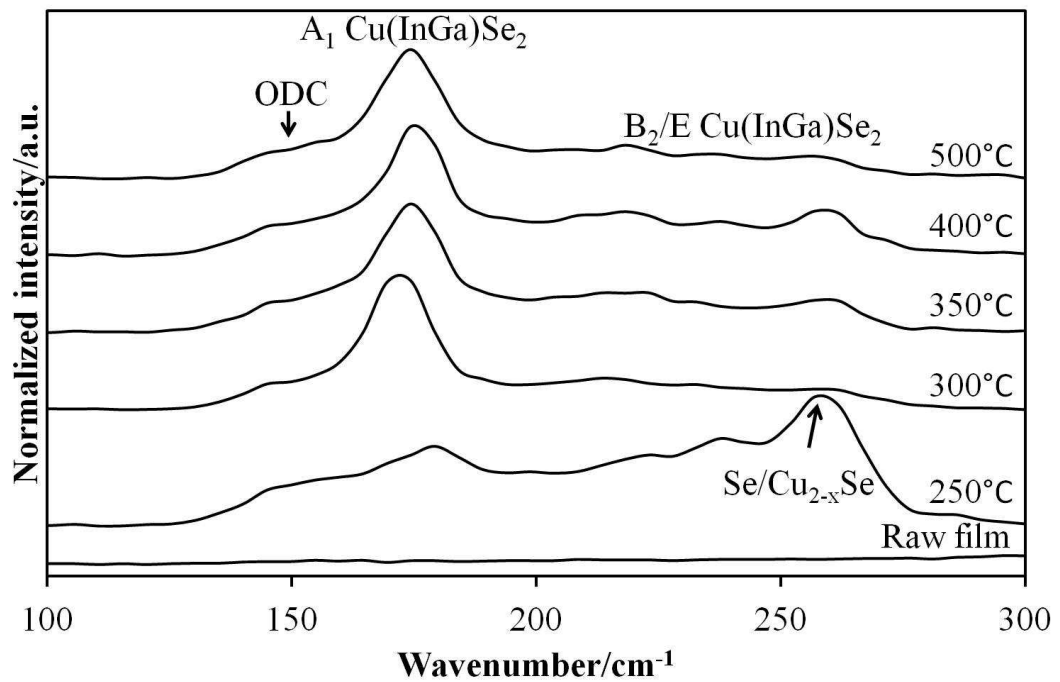


Figure 4.9 Raman spectra of CIGS films made from recipe B at different selenization temperatures.

4.1.2.4. UV-Vis-NIR spectrum

For direct bandgap materials, the absorption coefficient is dependent on the incident light energy and energy bandgap of materials (see equation below).

$$\alpha \propto \frac{\sqrt{h\nu - E_g}}{h\nu}$$

where α is absorption coefficient, $h\nu$ is photon energy and E_g is bandgap energy. By rearranging this equation to $(\alpha \cdot h\nu)^2 \propto h\nu - E_g$, one can extrapolate E_g by plotting $(\alpha \cdot h\nu)^2$ vs. $h\nu$.

In order to obtain the absorption coefficient, transmittance and reflectance were measured on CIGS thin films (100-200nm thick) deposited on quartz glass using recipe B. The absorption coefficient can be calculated using equation listed below.

$$\alpha = -\frac{1}{l} \ln \frac{T}{(1-R)^2}$$

where T and R are transmittance and reflectance and l is film thickness.

Figure 4.10 shows the results for three CIGS film with different Ga concentration. The bandgaps are estimated to be 0.95eV, 1.03eV and 1.13eV for no Ga, 15% Ga and 30% Ga chalcopyrite films. These values are slightly smaller than the results calculated from the equation¹⁹:

$$E_g^{CIGS}(x) = 1.65x + 1.01(1-x) - 0.151(1-x)x$$

where x is the proportion of gallium. Early measurements of bandgap energy of single crystal CIS suggested a value in the range of 1.02-1.04eV¹⁹. However, considerable papers reported the measured bandgap energy of CIS films were below 1.0eV due to

various reasons^{69, 70}. Due to the sublimation of gallium acetylacetonate, the final gallium contents in CIGS films were slightly below the initial precursor compositions, which reduced the bandgap energies of 15% and 30% Ga films.

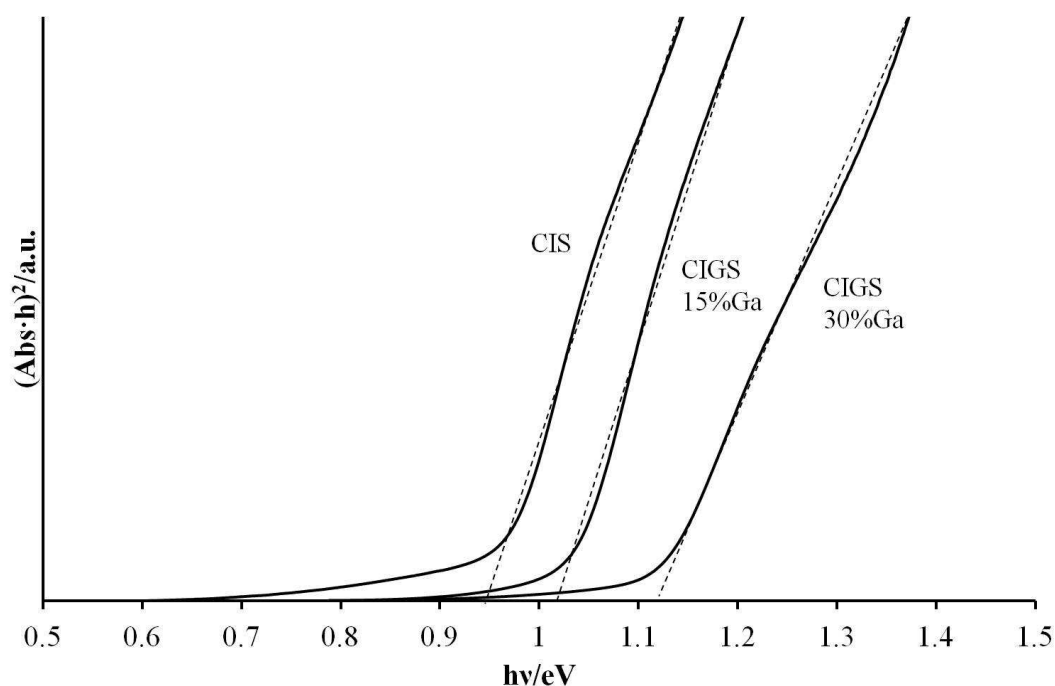


Figure 4.10 UV-Vis-NIR spectra of CIGS films with various Ga concentrations using recipe B.

4.1.2.5. Wavelength dispersive X-ray spectroscopy (WDS)

Gallium source in recipe B tended to evaporate resulting in the decreasing of gallium concentration. Wavelength dispersive X-ray spectroscopy was used to quantitatively identify the elemental composition in CIGS thin films. The analysis results are present in table below.

Table 4.1 Compositional comparison between WDS results on CIGS films and calculated results based on precursors' weights

	Ga	In	Cu	Ga/(Ga+In)
Measured after selenization	13.4%	43.1%	43.5%	24%
Calculated precursors	15.0%	35.3%	49.7%	30%

Based on the results in the table, gallium concentration decreased about 6%. Moreover, copper also lost about 6% during selenization. This made the resulted film more Cu-poor which might benefit for CIGS electronic properties.

4.1.2.6. Scanning electron microscopy (SEM)

Scanning electron microscopy was used to characterize films' grain size and morphology. Figure 4.11 shows SEM images of CIGS thin films using recipe A selenized at 500°C and 530°C. From the top-view images, it is easy to conclude that both samples were very crystallized, whereas from the side-view images, very small grains exist at the CIGS/Mo interfaces for both CIGS films. The origin of these small crystals will be discussed in chapter 5.

Figure 4.12 shows SEM images of CIGS thin films using recipe B. The small crystals at the interface (figure 4.12 side view), however, are still visible for samples selenized at low Se vapor pressure. By controlling the selenization condition, the CIGS film's crystallinity can be improved significantly (see figure 4.13). The influence of ink recipes and selenization on crystallinity will be discussed in chapter 5.

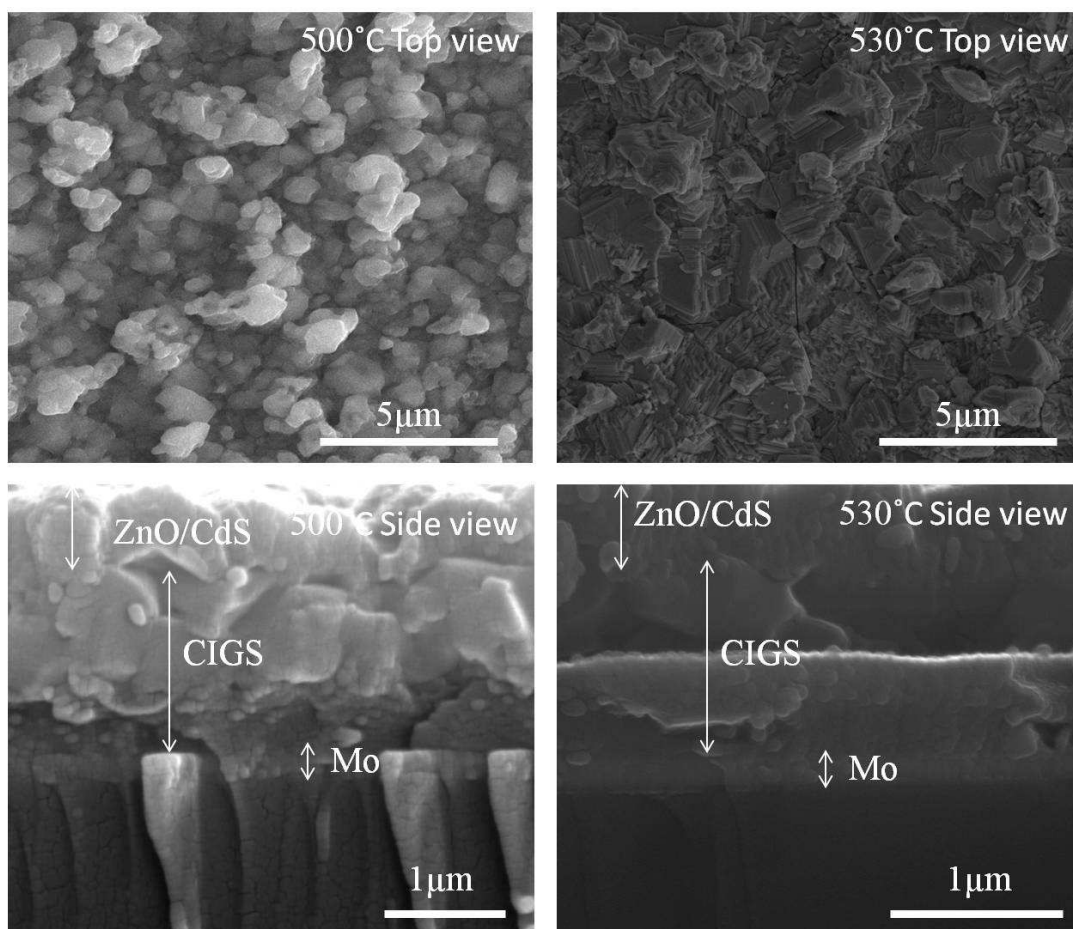


Figure 4.11 Scanning electron microscopy images of CIGS films using recipe A.

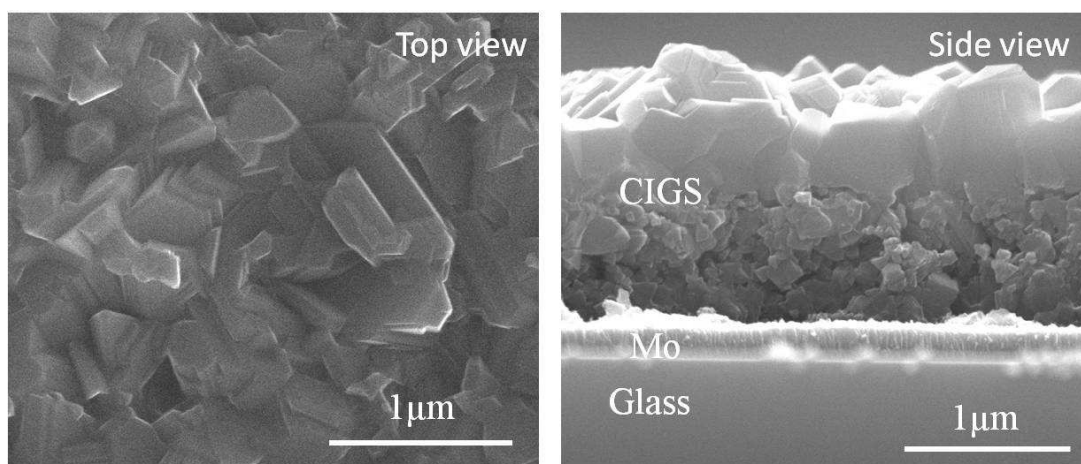


Figure 4.12 SEM images of CIGS films using recipe B under low Se pressure.

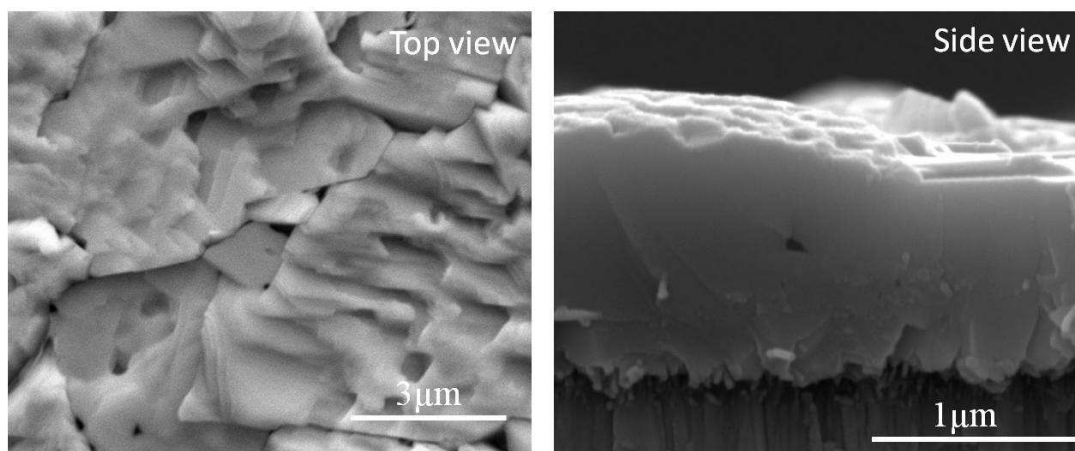
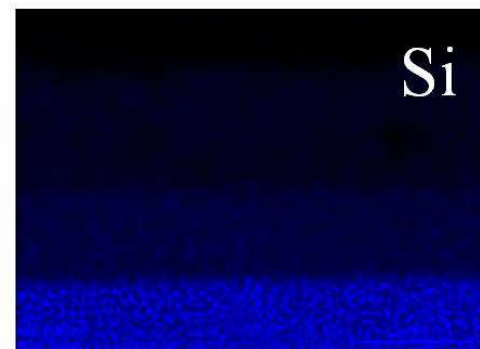
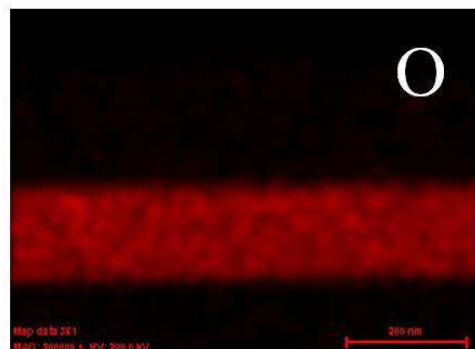
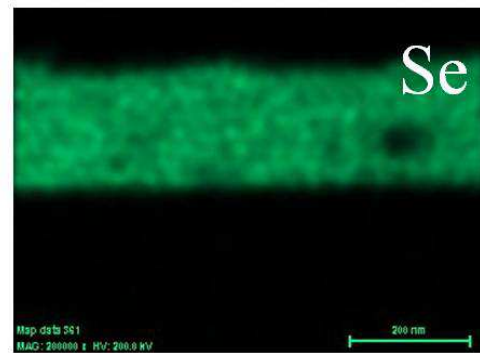
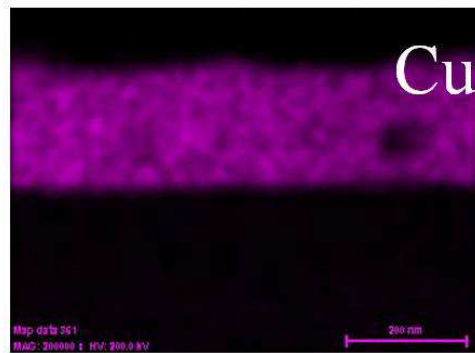
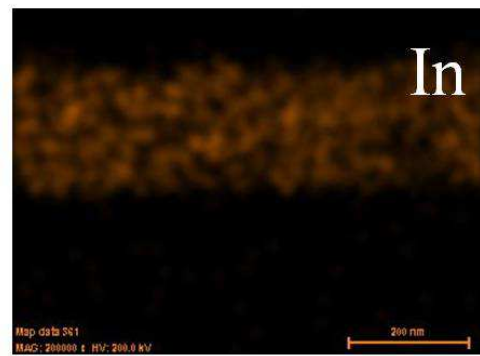
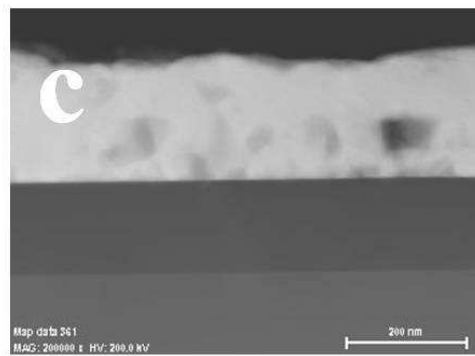
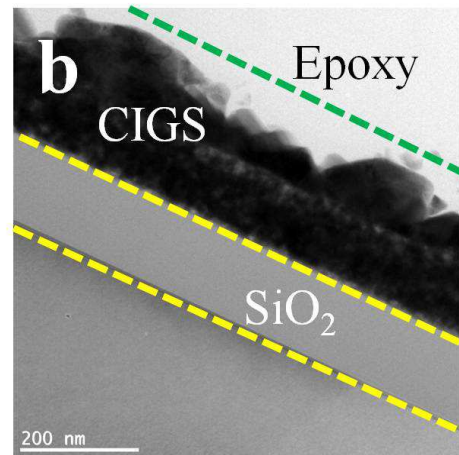
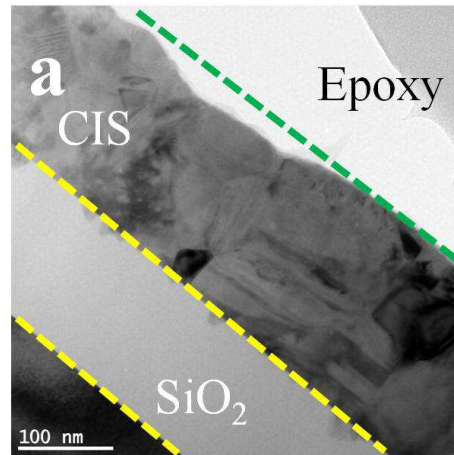


Figure 4.13 SEM images of CIGS films using recipe B under high Se pressure.

4.1.2.7. Transmission electron microscopy (TEM)

Transmission electron microscopy was used to quantitatively analyze the elemental distribution of CIGS films. In figure 4.14(a) and (b), CIS and CIGS films TEM images are presented. Both films were deposited on SiO_2/Si substrates at and selenized at same condition. For the CIS sample, the film is very crystallized whereas for the CIGS films, the film contains two separated layers with small crystals at interface. The TEM results are consistent with SEM results shown in figure 4.11 and 4.12.

Figure 4.14(c) and (d) shows elemental mapping for these two samples. It clearly shows that both samples have very uniform elemental distribution. Therefore this rules out the possibility that these small crystals for the CIGS sample resulted from elemental gradients or non-uniformity.



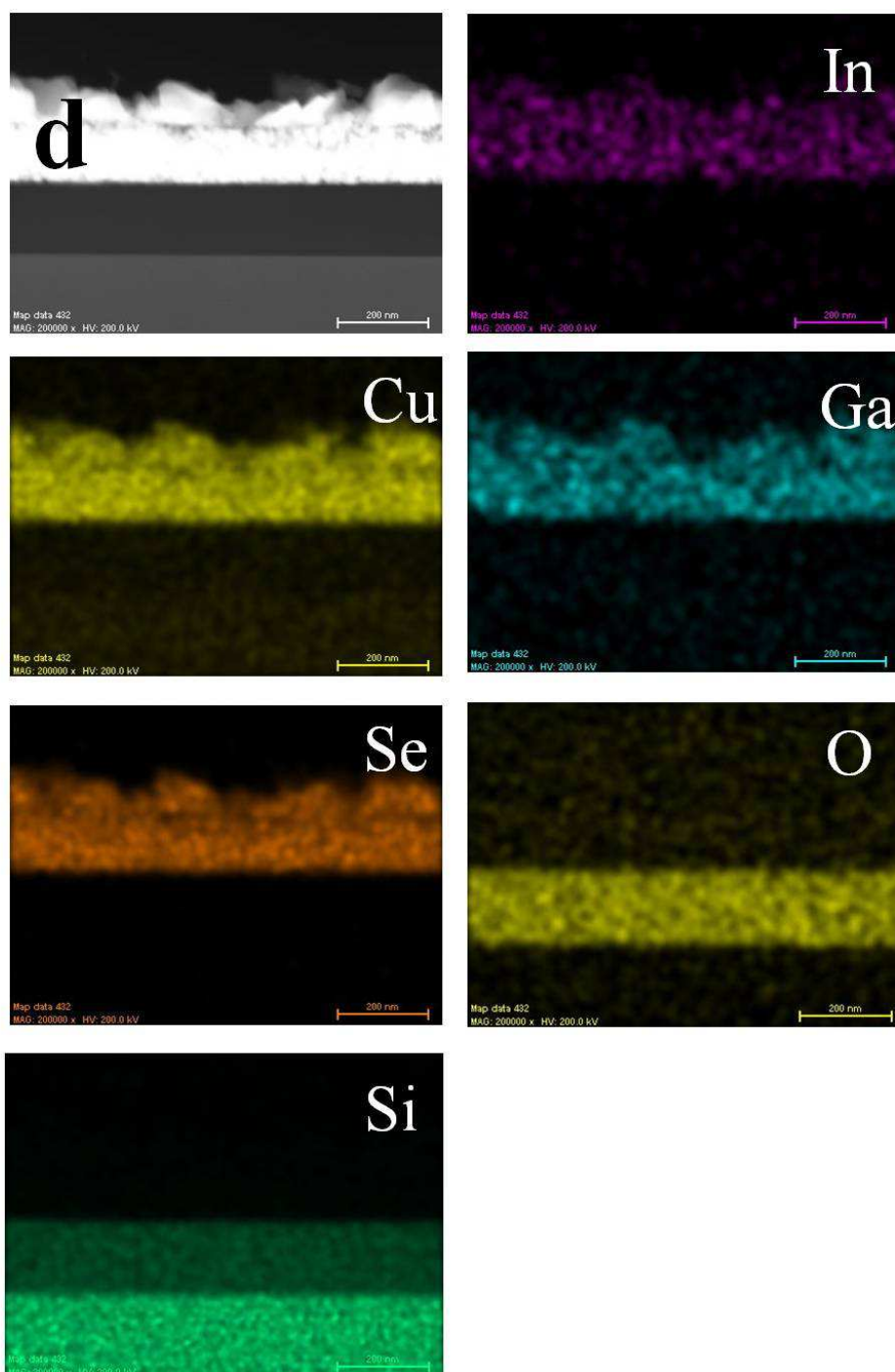


Figure 4.14 TEM cross-section images (a,b) and elemental mappings (c, d) of CIS and CIGS films, (a, c) for CIS and (b, d) for CIGS.

4.1.3 Buffer layer CdS

The thickness of buffer layers was calibrated by TEM cross-section images (see figure 4.15). The estimated thickness of CdS is 50nm. The deposition of CdS films is very uniform and conformal over CIGS layers.

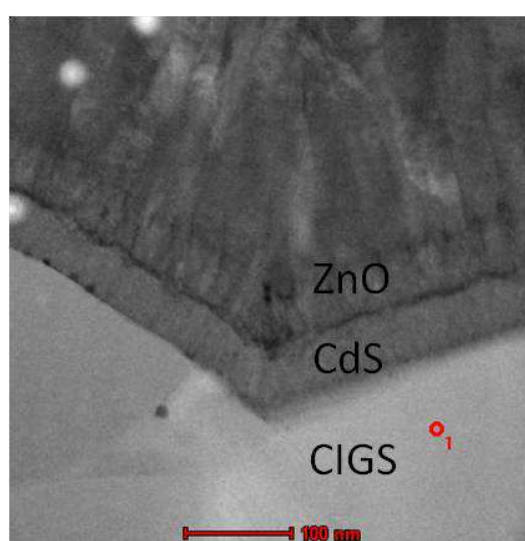


Figure 4.15 TEM images of ZnO/CdS/CIGS structures.

4.1.4 Window layer ZnO

The thicknesses of i-ZnO and Al:ZnO were 50nm and 340nm measured by Veeco profiler, which are consistent with the results from SEM and TEM cross-section images. Both films show dominant (002) orientation for hexagonal ZnO phase (see figure 4.16). For i-ZnO films, UV-Vis-NIR spectrum (figure 4.16(a) inset) shows 80% transmittance for light wavelength $> 400\text{nm}$ and 90% transmittance for light wavelength $> 600\text{nm}$. For Al:ZnO films, UV-Vis-NIR spectrum (figure 4.16(b) inset)

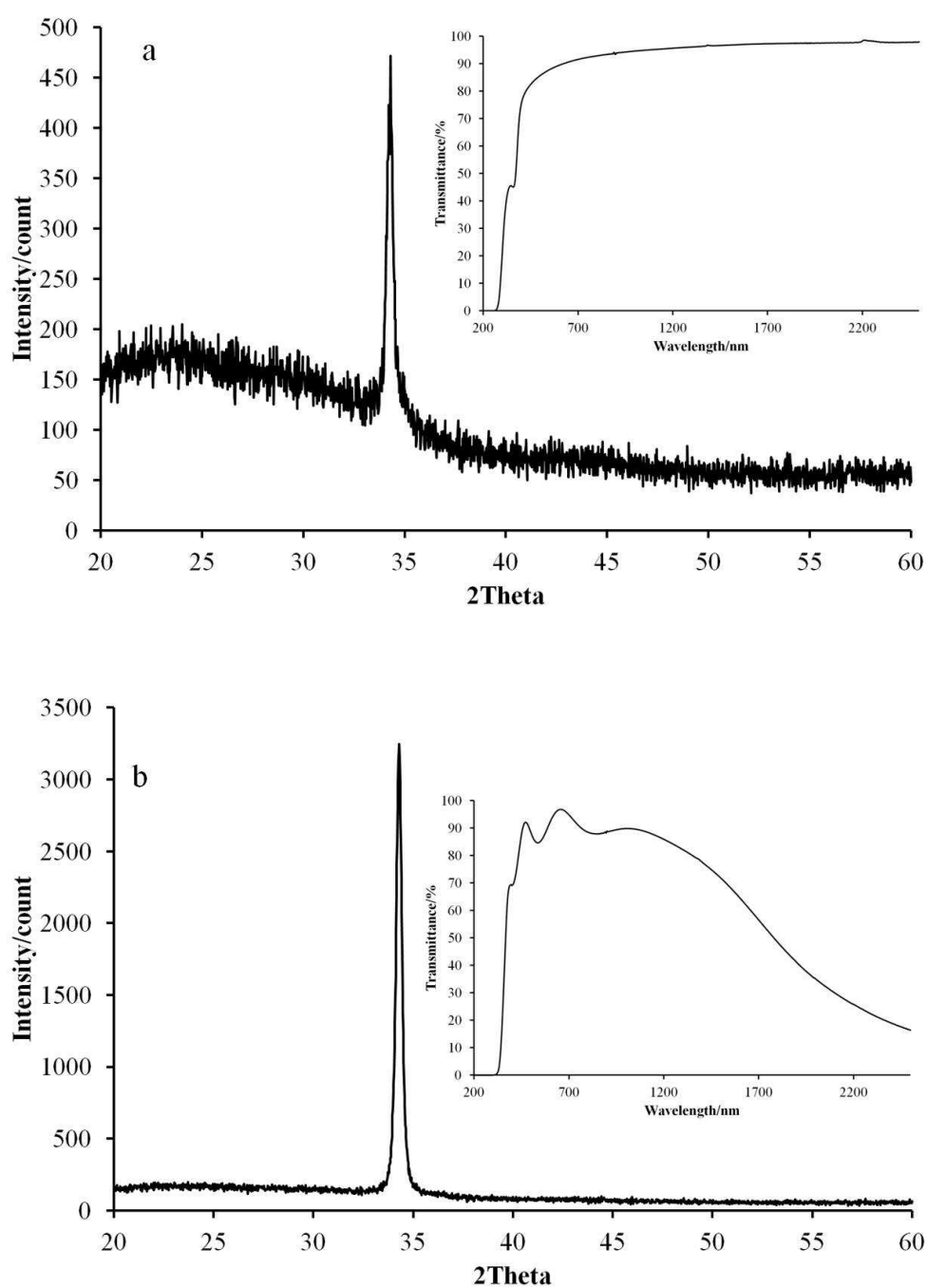


Figure 4.16 XRD and UV-Vis-NIR (insets) spectra of i-ZnO (a) and Al:ZnO (b).

shows that the transmittance is larger than 80% for wavelength $> 430\text{nm}$ but decreases dramatically for wavelength $> 1300\text{nm}$ due to strong free carrier absorption⁷¹. For resistivity measurement, sheet resistance of i-ZnO is too high to measure while the sheet resistance of 340nm-thick Al:ZnO is $56\Omega/\text{sq}$.

4.2 Solar cell characterization

4.2.1 Current-voltage analysis

Current-voltage (J-V) measurements under standard illumination conditions, $100\text{mW}/\text{cm}^2$ Am1.5 spectrum at 25°C , were applied to solar cell evaluation and characterization. Three basic parameters can be directly determined from illuminated J-V curves: V_{oc} , J_{sc} and FF . For a single diode model, the J-V relation can be described as

$$J = J_0 \left(e^{\frac{q(V-JR_S)}{AkT}} - 1 \right) + \frac{V - JR_S}{R_{SH}} - J_L \quad (1)$$

In order to determine A , J_0 , R_S and R_{SH} , several techniques have been developed. Here, a method adopted from Sites⁶³ is introduced.

Differentiate equation 1 to eliminate J_L (assume J_L is constant and ignore 1 in the parentheses):

$$1 = J_0 e^{\frac{q(V-JR_S)}{AkT}} \frac{\frac{dV}{dJ} - R_S}{\frac{AkT}{q}} + \frac{\frac{dV}{dJ} - R_S}{R_{SH}} \quad (2)$$

Substitute equation 1 into equation 2:

$$1 = \left(J + J_L - \frac{V - JR_S}{R_{SH}} \right) \frac{\frac{dV}{dJ} - R_S}{\frac{AkT}{q}} + \frac{\frac{dV}{dJ} - R_S}{R_{SH}} \quad (3)$$

If $R_S/R_{SH} \ll 1$, then

$$1 = \left(J + J_L - \frac{V}{R_{SH}} \right) \frac{\frac{dV}{dJ} - R_S}{\frac{AkT}{q}} + \frac{\frac{dV}{dJ}}{R_{SH}} \quad (4)$$

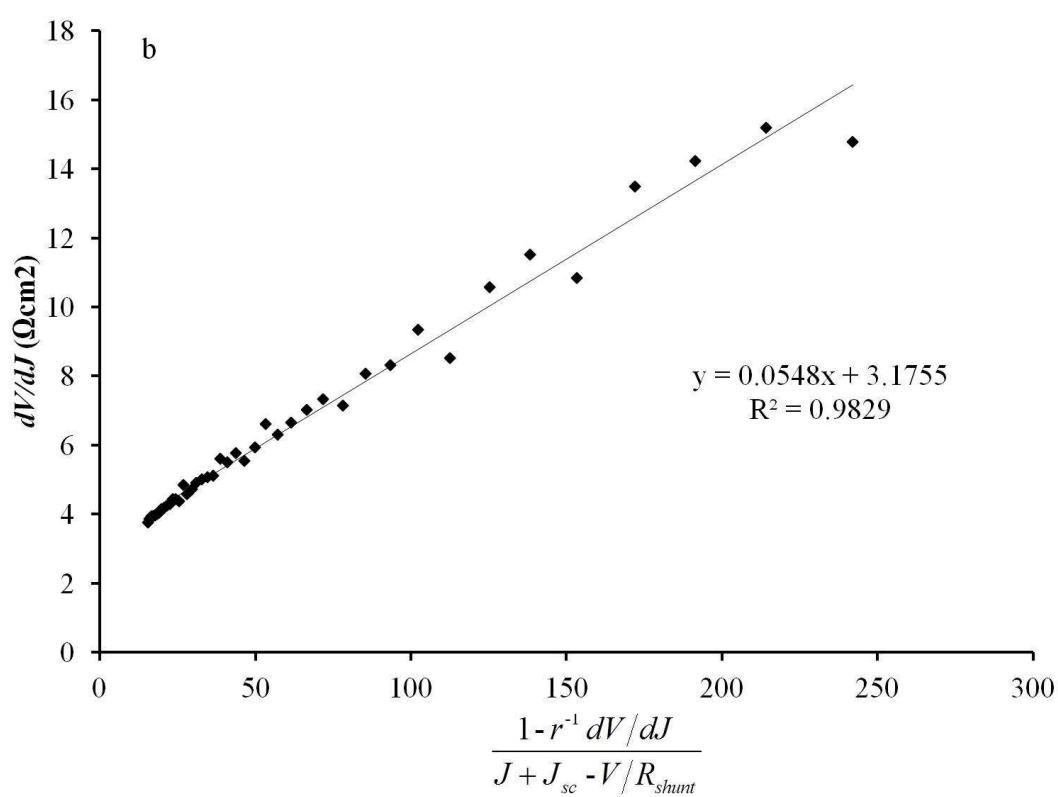
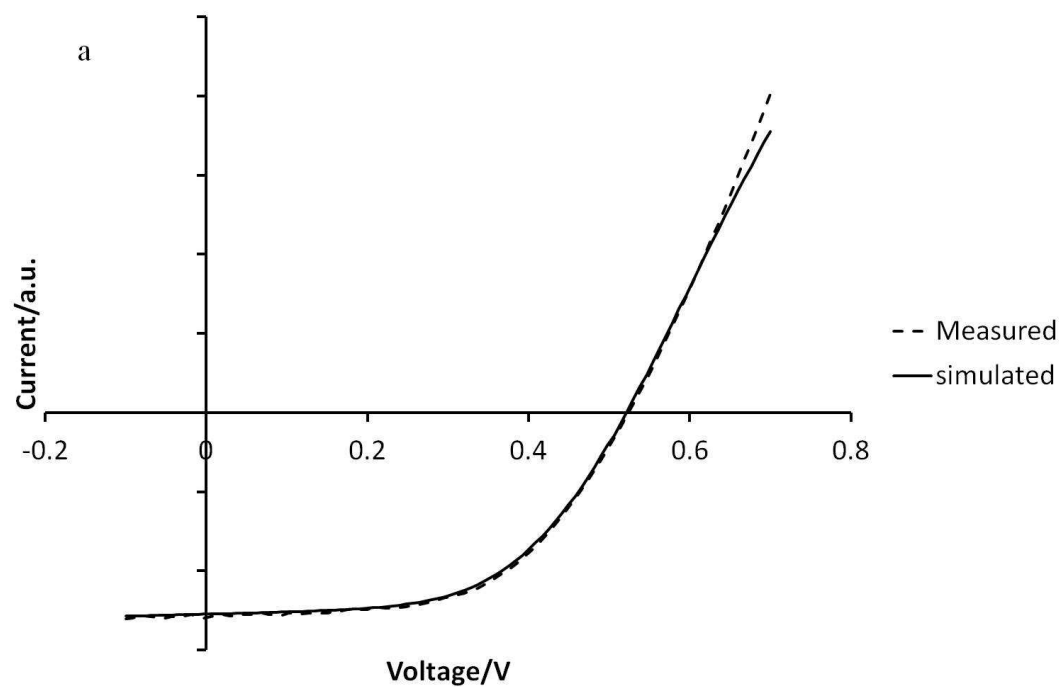
Rearrange equation 4:

$$\frac{dV}{dJ} = R_S + \frac{AkT}{q} \frac{1 - \frac{1}{R_{SH}} \frac{dV}{dJ}}{J + J_L - \frac{V}{R_{SH}}} \quad (5)$$

R_{SH} is determined from the slope at J_{sc} in J-V curves. By plotting $\frac{dV}{dJ}$ vs.

$\frac{1 - \frac{1}{R_{SH}} \frac{dV}{dJ}}{J + J_L - \frac{V}{R_{SH}}}$ at forward bias region, R_S and A can be extrapolated from the intercept

and the slope of the plotted curve.



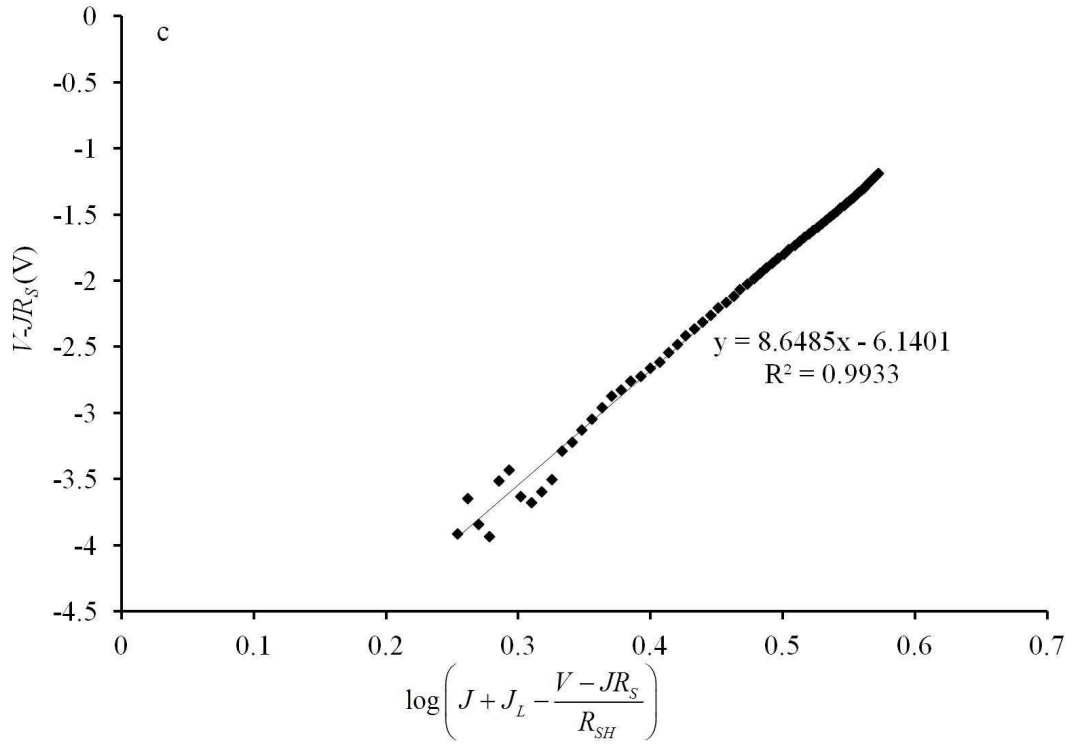


Figure 4.17 J-V characteristics of a solar cell. (a) measured and simulated J-V curves, (b) plotting equation (5) and (6) to extrapolate device parameters.

Rearrange equation 1:

$$\log \left(J + J_L - \frac{V - JR_s}{R_{SH}} \right) = \log J_0 + \frac{\log e}{\frac{AkT}{q}} (V - JR_s) \quad (6)$$

By plotting the left side of equation 6 vs. $(V - JR_s)$ at forward bias region, J_0 and A can be extrapolated from the intercept and the slope of the plotted curve. The value of A should be consistent with the value extrapolated from equation 5.

Figure 4.17(a) shows the measured and simulated J-V curves for a solar cell with $V_{oc}=0.524\text{V}$, $J_{sc}=25.66\text{mA/cm}^2$ and $\eta=7.52\%$. Table 4.2 shows device parameters extrapolated from the curves shown in figure 4.17(b) and (c) which are based on equation (5) and (6). The simulated results can generate a very close curve as measured one shown in figure 4.17(a). The comparison of solar cells fabricated under different conditions will be discussed in chapter 5.

Table 4.2 Device parameters of a solar cell

$J_0 (\text{A/cm}^2)$	$R_{series} (\Omega\text{cm}^2)$	R_{shunt} at $V_{oc} (\Omega\text{cm}^2)$	A (ideality factor)
1.75e-6	3.18	405	2.16

4.2.2 Quantum efficiency (QE)

Quantum efficiency measurements are commonly used to analyze the current losses responsible for the reducing of J_{sc} ⁷¹. QE is equal to the ratio of the number of electrons generated by the device to the incident photon at each wavelength. The directly measured QE is called as external QE which can be quantitatively corrected to generate internal QE defined as $\text{EQE}/(1-\text{Reflectance})$. Figure 4.18(a) shows QE results for a 6.92% efficient solar cell. The EQE stays at around 70% in the range of 500-650nm and decreases gradually afterwards. The IQE curve moves up about 3-4% in the range of 400nm-950nm after eliminating the influence of surface reflection. The major energy loss of current is a result of poor carrier collection efficiency in the range of 650nm to 1100nm which could be attributed to severe backside recombination and the insufficient thickness of the absorber layer⁷. For CIGS, IQE can be approximated by:

$$IQE \cong 1 - \frac{e^{-\alpha W}}{\alpha L + 1}$$

where α , W and L are absorption coefficient, depletion width and minority carrier diffusion length, respectively⁷¹. By assuming $\alpha L \ll 1$ which is usually true for low efficient solar cells, the equation can be simplified as:

$$IQE = 1 - e^{-\alpha W}$$

By rearranging this equation, the absorption coefficient can be extrapolated as:

$$\alpha = \frac{\ln(1 - IQE)}{W}$$

The absorption coefficient and energy bandgap for direct bandgap materials has a relationship as $(\alpha \cdot h\nu)^2 \propto h\nu - E_g$. Since W is only a function of bias voltage, E_g can be extrapolated by plotting $[h\nu - \ln(1 - IQE)]^2$ vs. $h\nu$ ⁷². For this 6.92% CIGS solar cell, the bandgap is estimated to be 1.13eV (see figure 4.18(b)) which is consistent with other measurements.

Current losses measured by QE can result from optical issues, such as front surface reflection and the absorption in window, TCO and buffer layers, or electronic issues, such as recombination in absorber⁷¹. By applying a reverse bias during QE measurement, the electronic loss can be separated from the optical losses, since only former is affected by the applied bias⁷¹. Figure 4.19 shows the EQE results at 0V and -1V for a 6.24% efficiency solar cell. At reverse bias of 1 V, the collection of carrier at

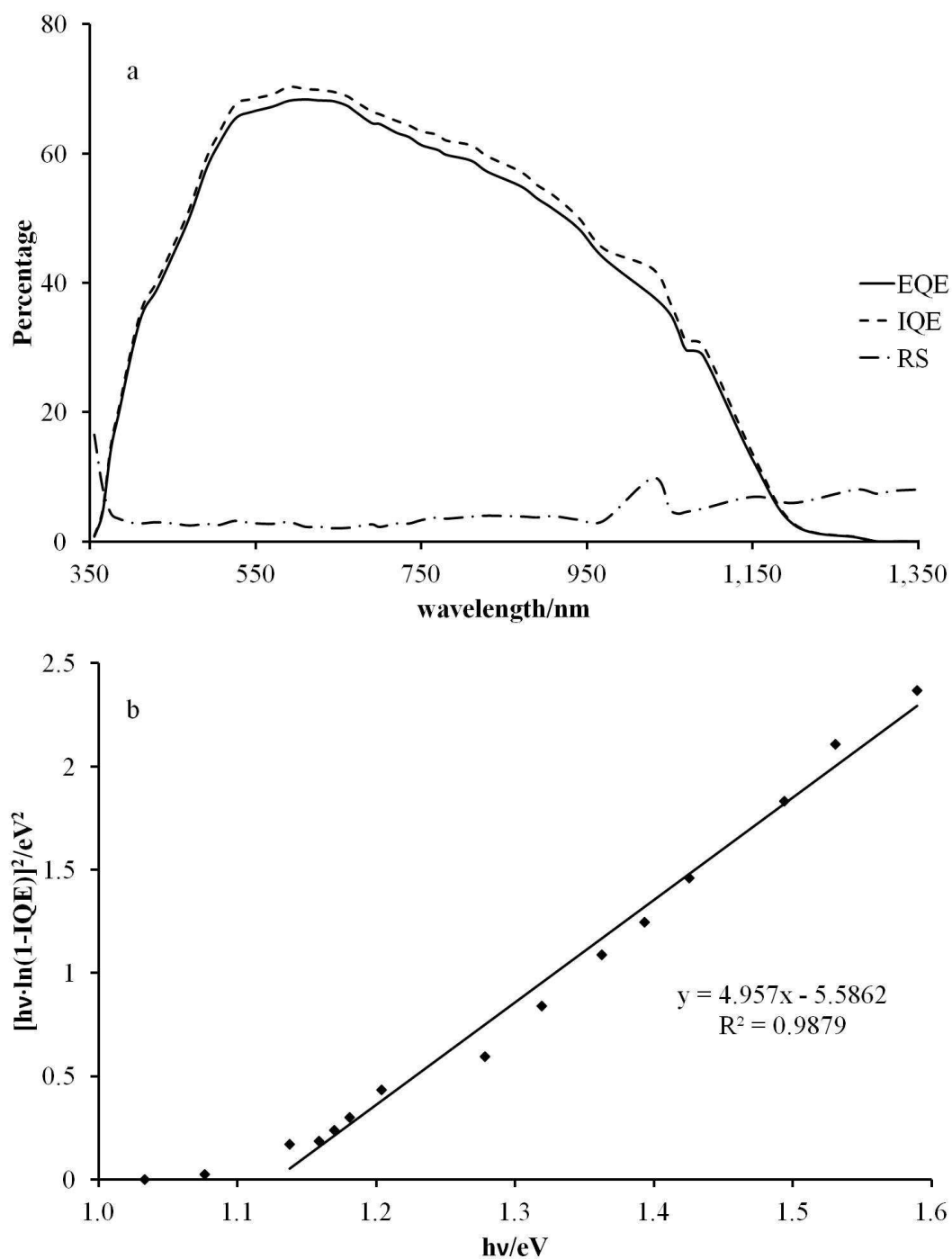


Figure 4.18 (a) External QE, internal QE and reflectance of a solar cell, (b) bandgap energies extracted from IQE in forward bias range.

longer wavelength becomes more efficient compared to the values at 0 V bias, which may imply severe backside recombination and short minority carrier lifetime in absorber layers⁷.

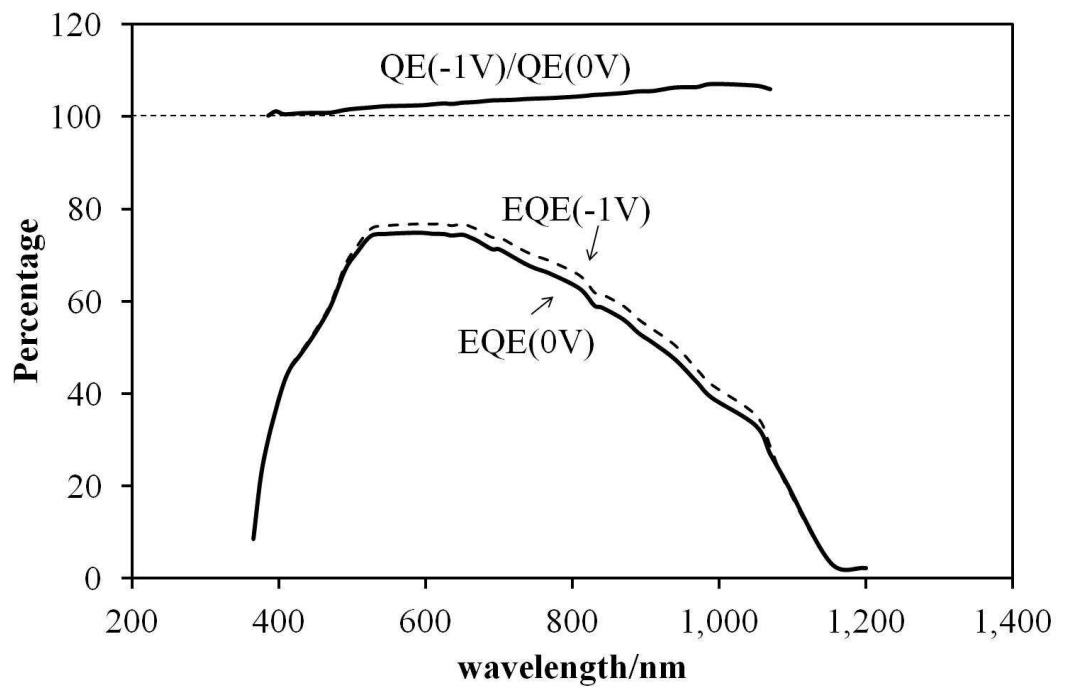


Figure 4.19 EQE curves of CIGS solar cells at 0V and 1V bias. Top inset: EQE ratio at -1V and 0V bias.

Chapter 5 Discussions

5.1 Thermodynamics of selenization

Thermodynamic properties of reactions are very useful information to predict how easy these reactions can occur. Here, I used copper and indium chlorides as an example to study the Gibbs free energies of selenization. Two possible reactions can happen during selenization:

- Reaction 1: $\text{CuCl}_2(\text{s}) + \text{InCl}_3(\text{s}) + 2.5\text{H}_2(\text{g}) + \text{Se}_2(\text{g}) \rightarrow \text{CuInSe}_2(\text{s}) + 5\text{HCl}(\text{g})$
- Reaction 2: $\text{CuCl}_2(\text{s}) + \text{InCl}_3(\text{s}) + 2\text{H}_2\text{Se}(\text{g}) + 0.5\text{H}_2(\text{g}) \rightarrow \text{CuInSe}_2(\text{s}) + 5\text{HCl}(\text{g})$

In reaction 2, H_2Se is formed by the reaction in gas phase between H_2 and Se_2 . The Gibbs free energies of these two reactions were calculated based on equation below:

$$\Delta_r G_T^0 = \sum \Delta_r H_{298}^0 - T \sum \left(\Delta_r \left\{ -\frac{G_T^0 - H_{298}^0}{T} \right\} \right)$$

Table 5.1 Gibbs free energy of forming ternary selenide CIS

T/k		298	500	600	700	800
$\Delta_r G_T^0 /$ kJ·mol ⁻¹	Reaction 1	-132	-187	-212	-237	-261
	Reaction 2	-72	-142	-176	-209	-242

The thermodynamic data of all the reaction compounds can be found in references^{73, 74}. Table 5.1 lists the Gibbs free energies of these two reactions. Since the Gibbs free energies are very negative at temperature above the melting temperature (494K) of

selenium, it can be concluded that these two reactions are thermodynamically favorable, which means both of them are likely to occur during selenization.

Except these two reactions to form ternary chalcopyrite CIS directly, metal chlorides may react with selenium to form binary selenides as well (see reactions listed below and table 5.2 for Gibbs free energies). Based on the data, it can be concluded that Cu_2Se , CuSe and In_2Se_3 can be easily formed at heated condition whereas the formation of InSe is less favorable.

- Reaction 3: $2\text{CuCl}_2(\text{s}) + 2\text{H}_2(\text{g}) + 1/2\text{Se}_2(\text{g}) \rightarrow \text{Cu}_2\text{Se}(\text{s}) + 4\text{HCl}(\text{g})$
- Reaction 4: $\text{CuCl}_2(\text{s}) + \text{H}_2(\text{g}) + 1/2\text{Se}_2(\text{g}) \rightarrow \text{CuSe}(\text{s}) + 2\text{HCl}(\text{g})$
- Reaction 5: $2\text{InCl}_3(\text{s}) + 3\text{H}_2(\text{g}) + 1.5\text{Se}_2(\text{g}) \rightarrow \text{In}_2\text{Se}_3(\text{s}) + 6\text{HCl}(\text{g})$
- Reaction 6: $\text{InCl}_3(\text{s}) + 1.5\text{H}_2(\text{g}) + 0.5\text{Se}_2(\text{g}) \rightarrow \text{InSe}(\text{s}) + 3\text{HCl}(\text{g})$

Table 5.2 Gibbs free energy of forming binary selenides

	T/k	298	300	400	500	600
$\Delta_r G_T^0 /$ $\text{kJ} \cdot \text{mol}^{-1}$	Reaction 3	-150	-151	-179	-207	-235
	Reaction 4	-122	-122	-128	-175	-201
	Reaction 5	-98	-98	-126	-154	-182
	Reaction 6	18	18	0.2	17	-34

XRD results presented in section 4.1.2.2 showed that copper and indium oxides were initially formed after air annealing. Therefore it is necessary to examine the transformation reactions of these oxides to selenides (see reaction 7-12 and table 5.3 for their Gibbs free energies). One can conclude based on data in table 5.3 that copper and indium oxides can be easily converted to selenides, which is consistent with the

XRD results in section 4.1.2.2 where this transformation was able to occur at only 250°C.

- Reaction 7: $\text{CuO(s)} + 1/2\text{Se}_2\text{(g)} + \text{H}_2\text{(g)} \rightarrow \text{CuSe(s)} + \text{H}_2\text{O(g)}$
- Reaction 8: $\text{Cu}_2\text{O(s)} + 1/2\text{Se}_2\text{(g)} + \text{H}_2\text{(g)} \rightarrow \text{Cu}_2\text{Se(s)} + \text{H}_2\text{O(g)}$
- Reaction 9: $\text{CuO(s)} + \text{H}_2\text{Se(g)} \rightarrow \text{CuSe(s)} + \text{H}_2\text{O(g)}$
- Reaction 10: $\text{Cu}_2\text{O(s)} + \text{H}_2\text{Se(g)} \rightarrow \text{Cu}_2\text{Se(s)} + \text{H}_2\text{O(g)}$
- Reaction 11: $\text{In}_2\text{O}_3\text{(s)} + 1.5\text{Se}_2\text{(g)} + 3\text{H}_2\text{(g)} \rightarrow \text{In}_2\text{Se}_3\text{(s)} + 3\text{H}_2\text{O(g)}$
- Reaction 12: $\text{In}_2\text{O}_3\text{(s)} + 3\text{H}_2\text{Se(g)} \rightarrow \text{In}_2\text{Se}_3\text{(s)} + 3\text{H}_2\text{O(g)}$

Table 5.3 Gibbs free energy of transformation of oxides to selenides

T/k		298	500	600	700	900
$\Delta_r G_T^0 /$ kJ·mol ⁻¹	Reaction 7	-189	-183	/	-175	-166
	Reaction 8	-196	-191	/	-190	-188
	Reaction 9	-156	-159	/	-160	-160
	Reaction 10	-163	-167	/	-175	-182
	Reaction 11	-305	-287	-279	/	/
	Reaction 12	-216	-205	-229	/	/

In both recipes A and B, instead of using Cu^{1+} , Cu^{2+} was selected to synthesize CIGS where copper owns 1+ state. This contradicted our common sense that it should be easier to happen for reactions from Cu^{1+} salts to Cu^{1+} selenides. Figure 5.1 compares the CIS formation reactions using CuCl (reaction 13 and 14) and CuCl₂ (reaction 1 and 2). It clearly shows that reactions involving CuCl₂ have more negative Gibbs free energies than reactions involving CuCl. This means that from thermodynamic

standpoint of view CuCl_2 can be transformed to CIS easier than CuCl does. Therefore Cu^{2+} salts were chosen as copper precursor instead of CuCl .

- Reaction 13: $\text{CuCl(s)} + \text{InCl}_3\text{(s)} + 2\text{H}_2\text{(g)} + \text{Se}_2\text{(g)} \rightarrow \text{CuInSe}_2\text{(s)} + 4\text{HCl(g)}$
- Reaction 14: $\text{CuCl(s)} + \text{InCl}_3\text{(s)} + 2\text{H}_2\text{Se(g)} \rightarrow \text{CuInSe}_2\text{(s)} + 4\text{HCl(g)}$

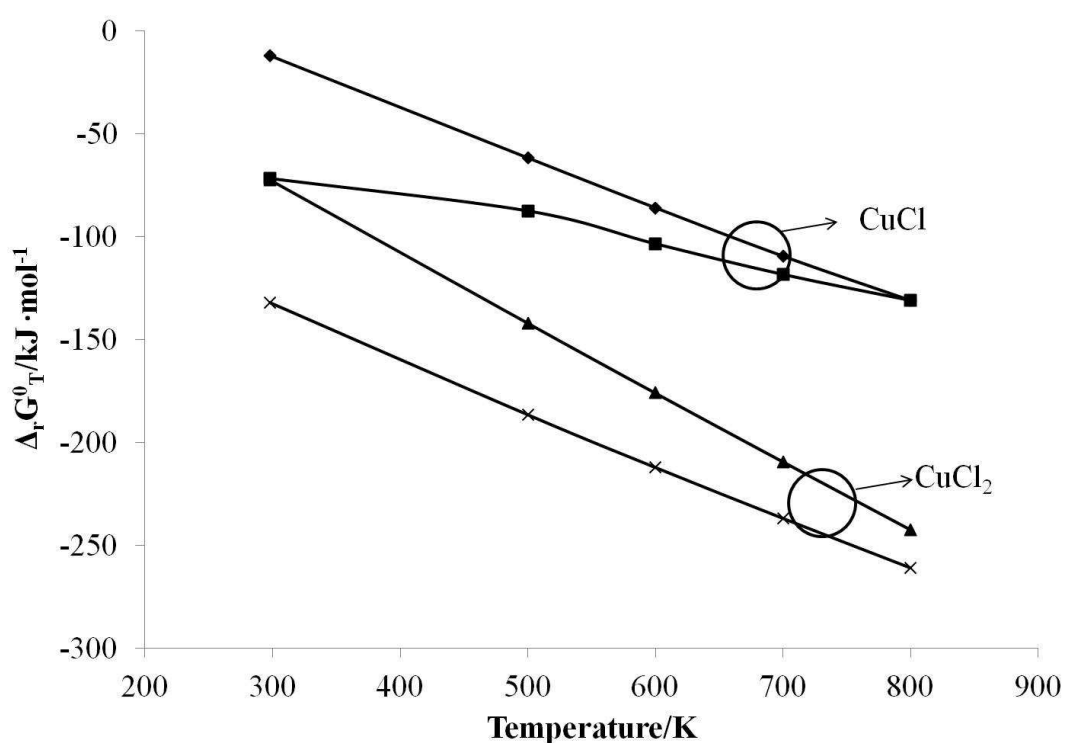


Figure 5.1 Gibbs free energies of CIS formation using CuCl and CuCl_2 .

5.2 Characterization of solar cells using recipe A

CIGS thin films were able to be successfully synthesized using recipe A. In chapter 4, the XRD and Raman analysis confirmed the formation of pure CIGS phase without contamination of binary selenides such as copper selenide which is a common by-

product for most of CIGS deposition techniques and requires an extra KCN etching step^{8, 59}. In order to achieve highly efficient CIGS solar cell, it is essential to obtain micron-sized grains to diminish the recombination of electron-hole pairs. Cu_{2-x}Se usually serves as a flux agent to form a quasi-liquid phase to enhance the crystallization at a relatively lower temperature. However, this technique has a possibility to leave Cu_{2-x}Se as a secondary phase which would short the solar cells due to its higher conductivity compared with the chalcopyrite CIGS phase. In our process, Selenium vapor was utilized to assist the growth of crystals in a slightly In-rich phase which eliminates the formation of Cu_{2-x}Se and avoids the KCN etching step.

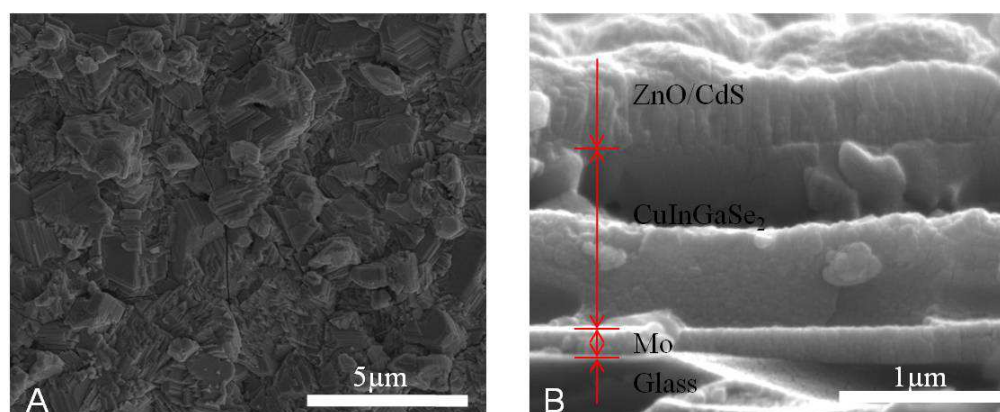


Figure 5.2 SEM images of CIGS films: (A) top view of a CIGS film and (B) cross-sectional view of the full device.

Scanning electron microscopy (SEM) images of a top view CIGS film and a cross-sectional view from a finished device film-stack are given in figure 5.2, respectively. A dense polycrystalline film with grain sizes at a micron scale can be seen clearly from the image shown in figure 5.2A. The cross-sectional image (see figure 5.2B)

clearly shows a film stack with several layers including a $\sim 340\text{nm}$ ZnO top contact layer, a $1.2\mu\text{m}$ CIGS layer, and a 200nm Mo back contact layer. Due to the resolution limit of the instrument, it is hard to distinguish between the CdS and i-ZnO layers. It is interesting to notice that the CIGS film has a clear interface which separates the CIGS film into dual layers. The main reason for this is due to the two-pass printing strategy which requires printing of two identical passes in order to reach certain thickness. The top layer of the CIGS film has larger grain sizes compared to the grains of the bottom layer.

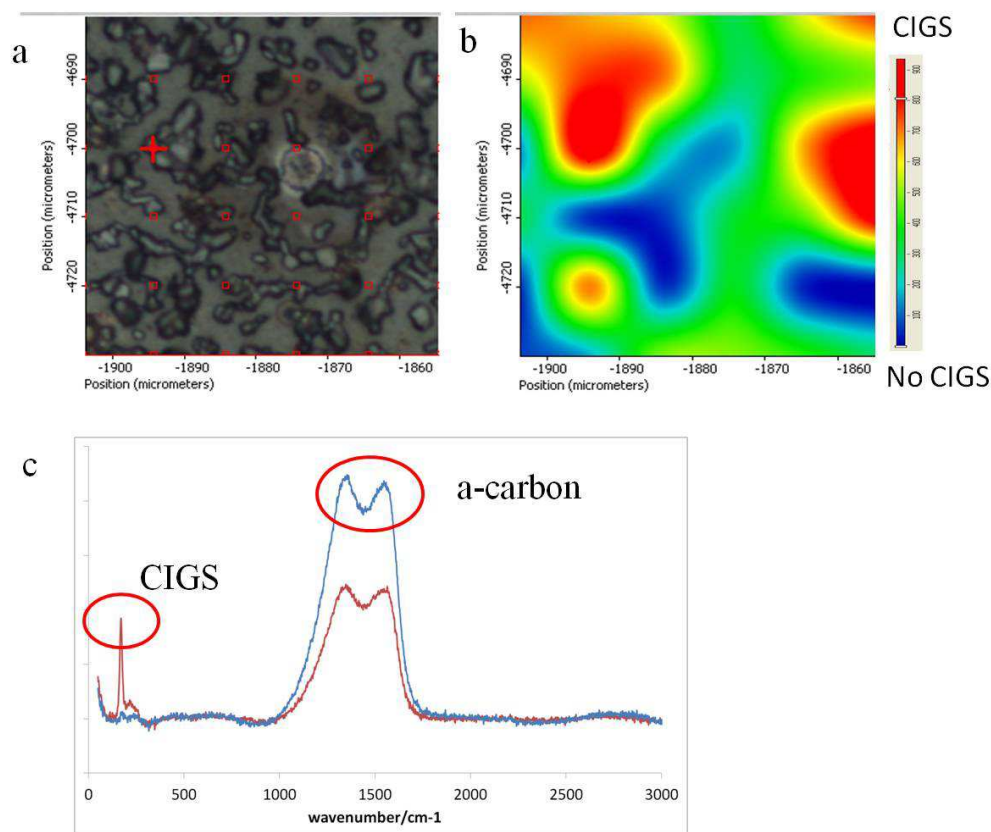


Figure 5.3 Optical Image (a) and Raman mapping image (b) of CIGS films and Raman spectra corresponding to Raman mapping image (c).

In addition, Raman results (figure 5.3) reveal that the absorber layer contains certain amount of amorphous carbon resulting from the incomplete evaporation or decomposition of solvents and acetate anion which may prevent CIGS forming large grains. No voids were observed from the cross-sectional image. The dense crystalline CIGS films are essential for good photovoltaic solar cells. No chloride residues were detected by Energy-dispersive X-ray spectroscopy (EDS). EDS indicated a $\text{Cu}_{0.81}\text{In}_{0.79}\text{Ga}_{0.21}\text{Se}_{1.87}$ composition with $\text{Cu}/(\text{In}+\text{Ga})=0.81$ and $\text{Ga}/(\text{In}+\text{Ga})=0.21$. The Cu vacancy, V_{Cu} , is considered to be the dominant acceptor which controls the p-type property of the Cu-poor CIGS film^{14, 19}. Thus a slightly copper-poor composition is beneficial for the formation of p-type semiconductor, while 20% gallium doping is lower than the typical value used in the high efficiency CIGS solar cells.

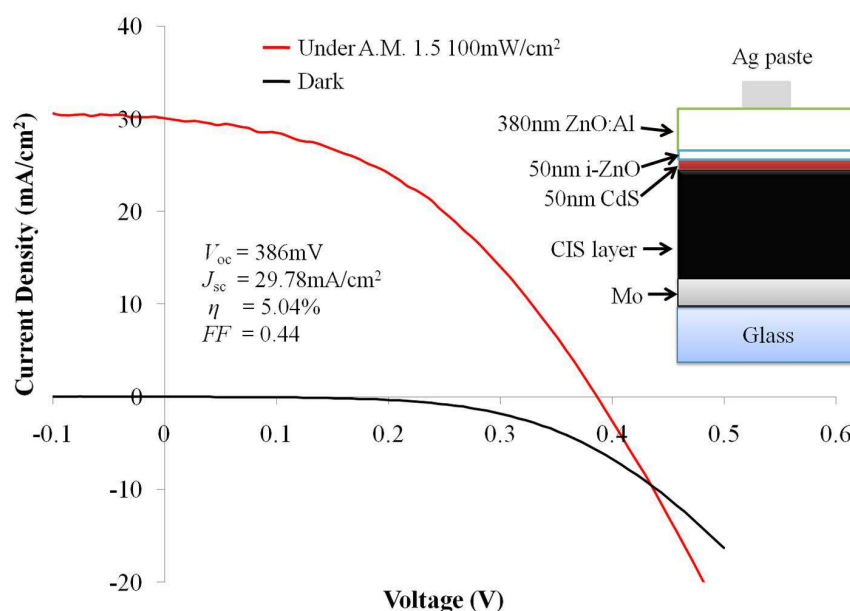


Figure 5.4 J-V characteristics of a CIGS solar cell.

Figure 5.4 shows the J-V characteristics of a best printed CIGS solar cell using recipe A. The short circuit current (J_{sc}), open circuit voltage (V_{oc}), fill factor (FF), and total area power conversion efficiency (η) of the device are 29.78 mA/cm², 386 mV, 0.44, and 5.04%, respectively. A crossover can be seen in the J-V curves shown in Figure 5.4. The common explanation of the crossover is the absorption of photons in the CdS layers⁷⁵. In order to verify the origin of the crossover in the devices, a 610nm long pass filter was used to eliminate the absorption of photons in CdS layers (CdS bandgap is 2.4eV). From Figure 5.5, one can observe that the crossover disappeared when red light was shined on the device confirming the above explanation.

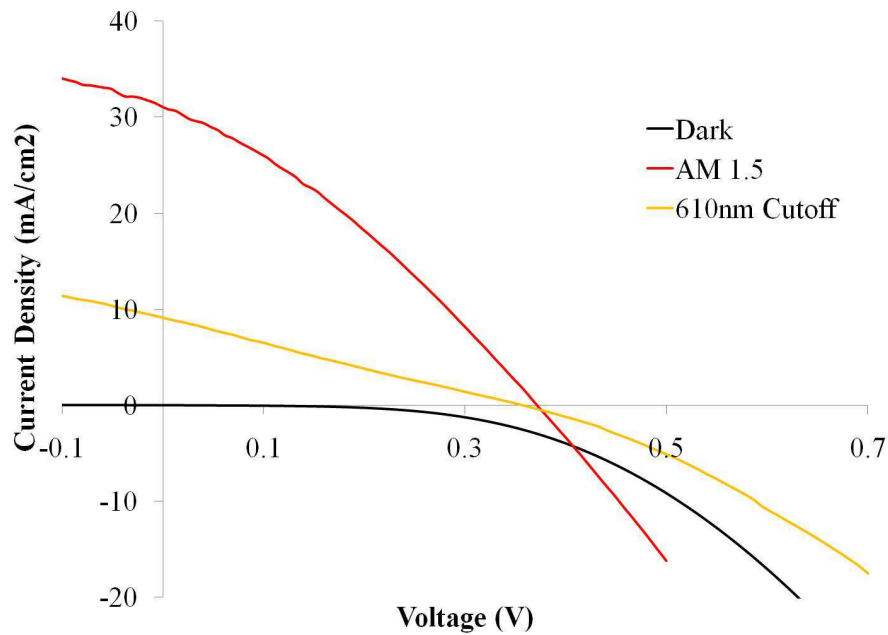


Figure 5.5 Comparison of J-V measurements of CIGS solar cell at dark, AM1.5 and 610nm long pass filter.

Compared to the 19.9%-efficiency solar cell made by NREL¹, the deficiency of V_{oc} and FF limits the performance of solar cells. The diode ideality factor, the area-normalized shunt resistance and the series resistance under AM 1.5 illumination are estimated to be $2.3 \Omega\text{cm}^2$, $95.9 \Omega\text{cm}^2$ and $3.3 \Omega\text{cm}^2$, respectively. Low shunt resistance resulting from pin-holes, cracks or impurities in and near the junction leads to an increasing shunt current and a decreasing V_{oc} . Usually, a large diode ideality factor is caused by interface recombination and space charge recombination which result from the impurities at metallurgical junction and depletion region, respectively^{63, 76}. Therefore, the elimination of pin-holes, cracks or impurities are essential for the fabrication of higher efficient solar cells. In addition, the series resistance which is 10 times larger than the series resistance of the co-evaporation solar cells results in the softness in the knee of J-V curve which degrades both FF and η .

5.3 Carbon contamination issue

Raman results presented in figure 5.3 show series amorphous carbon contamination for CIGS synthesized using recipe A, which is consistent with TGA result shown in section 4.1.2.1. Carbon contamination left from organic species in printed inks is a very common problem for most of solution-based processing techniques. Kaelin *et al.*⁵⁹ used metal salts dissolved in organic solvents with binders to fabricate CIGS films. The resulted films preserved a thick carbon layer beneath CIGS crystals. Long carbon chain binder Ethylcellulose is the major source for the carbon contamination. Guo *et al.*³⁶ converted CuInGaS_2 nanoparticles to dense CuInGaSe_2 films by

selenization. Several hundred nanometer-thick carbon layers were formed at the Mo/CIGS interface, which was due to surface ligand oleylamine.

Two suspicious reagents in recipe A are responsible for the carbon contamination in CIGS films. Chlorine in GaCl_3 is very acidic and corrosive, which may etch Mo back contacts and more importantly react with organic species in solution resulting in the formation of amorphous carbon residues in films. In order to eliminate the influence of chlorine, a stable and neutral compound gallium acetylacetonate was chosen to substitute gallium chloride. Anions in gallium acetylacetonate can improve the solubility of copper metals and be decomposed easily in air⁷⁷.

Ethanolamine used in recipe is a common complex agent used for the stabilization of metal precursors in solutions. Free electron pair on nitrogen atom of ethanolamine are bonded to copper cations in solution. The bond between ethanolamine and copper is too strong to break due to the strong nucleophilic property of ethanolamine, which inevitably results in carbon residue. Therefore ethanolamine was replaced by other agents.

There are several requirements for forming suitable inks without carbon residue left in deposited films. First, metal salts have to be dissolvable at high concentration ($>0.3\text{M}$) in alcohols. Copper acetate and indium acetate have very low solubility in alcohol unless strong complex agents are employed. Therefore it is desirable to find new reagents to help dissolve copper acetate. Second, the complex agents can be easily evaporated or decomposed. It is very challenging to fulfill both requirements at the

same time, since strong complex agents are usually hard to get rid of. Recipe B was developed to fulfill these requirements and able to produce CIGS films without carbon contamination.

5.4 Resolving carbon contamination issue using recipe B

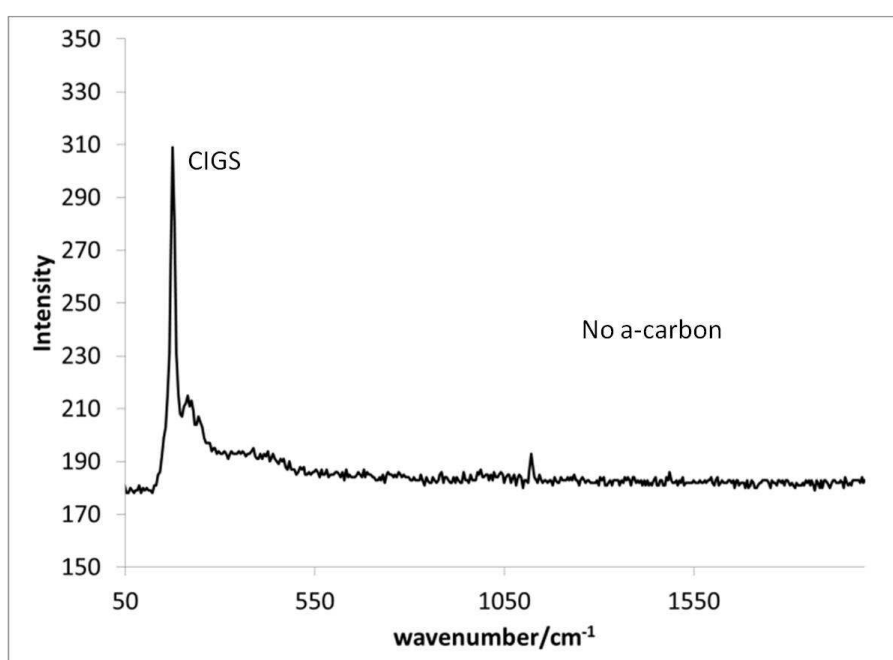


Figure 5.6 Raman spectrum of a CIGS film using recipe B.

CIGS thin films were synthesized by using recipe B. In chapter 4, TGA results of recipe B show that metal salts can be completely decomposed before 350°C which is also high enough to evaporate all the solvents in inks. XRD and Raman were used to verify the purity of CIGS phase. Amorphous carbon residual which shows broad Raman peaks from 1200 and 1600 cm^{-1} could not be detected in CIGS films (see figure 5.6). TEM elemental mapping in figure 4.14(c) and (d) excluded the existing of

oxygen. The purity of obtained CIGS films proves the excellent property of the new recipe to eliminate carbon and the superior selenization process to reduce the oxygen content.

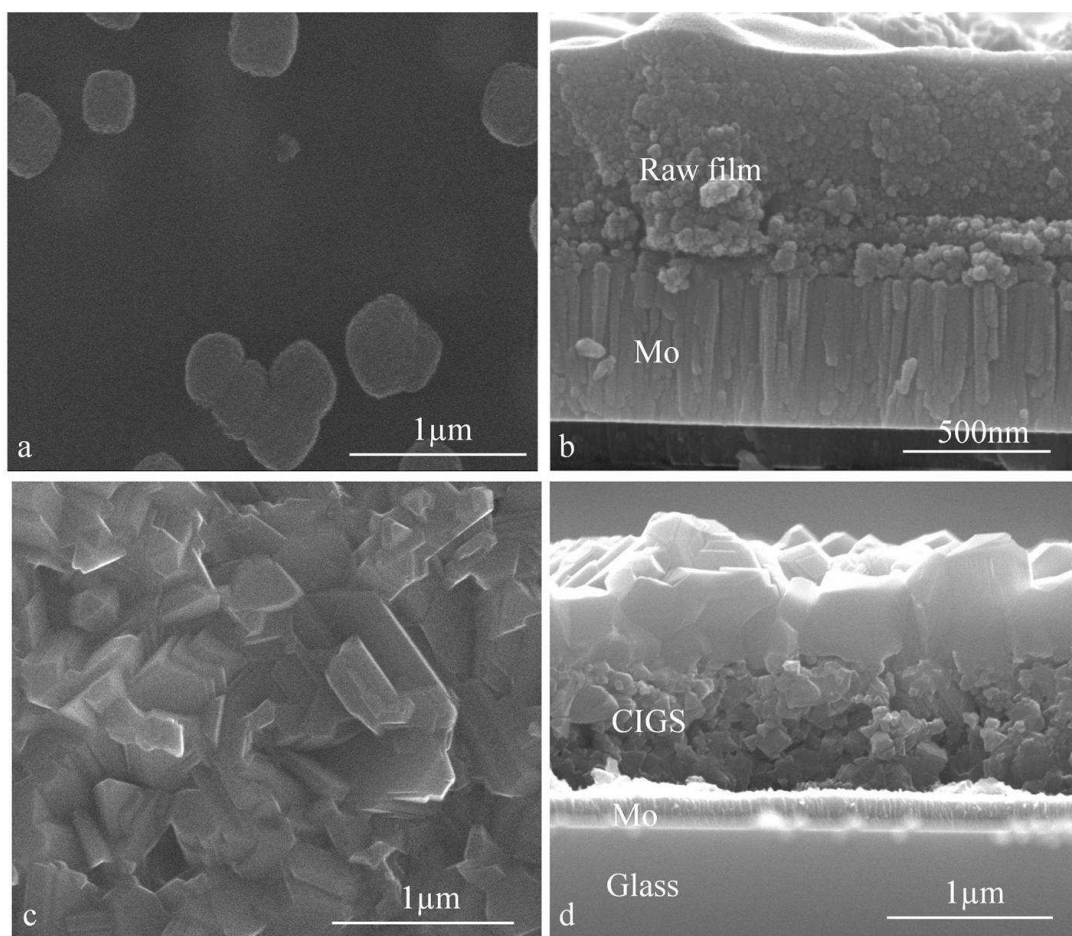


Figure 5.7 SEM images of precursor film and CIGS film: top-view (a) and side view (b) of precursor film, top view (c) and side view (d) of CIGS film.

From figure 5.7a and 5.7b, it can be seen clearly that the precursor film contains densely packed nano-sized particles with amorphous appearance from top view, which corresponds to the XRD results. After selenization, micron-sized crystals were formed

across the film, which is confirmed by the top-view and side-view SEM images shown in figure 5.7c and 5.7d. These results provide solid evidences to support the effectiveness of recrystallization and grain growth during the selenization process. However, there are still some smaller crystals existing at the interface between CIGS and Mo layers. The main reason for these smaller grains could be attributed to the limitation of Se diffusion through the dense CIGS films.

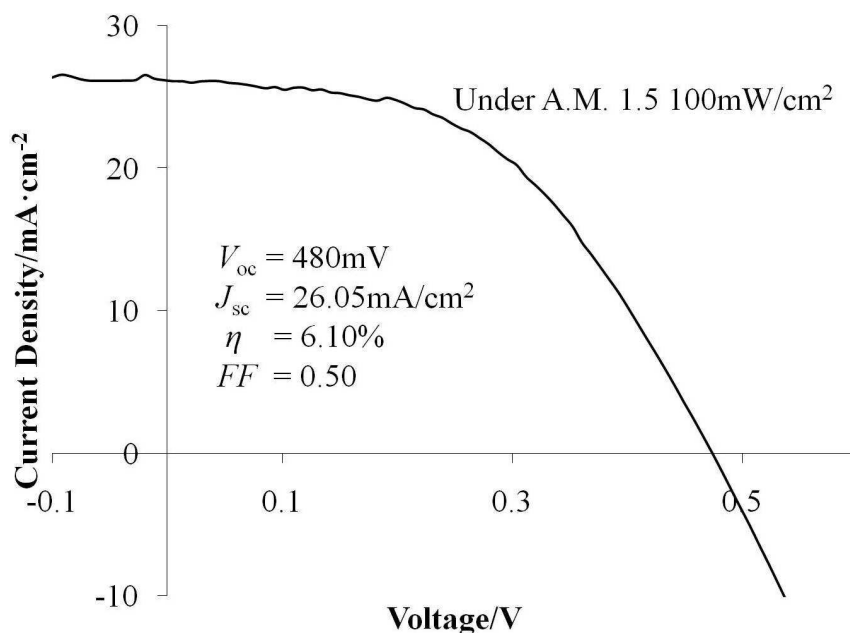


Figure 5.8 J-V characteristics of CIGS thin film solar cells using recipe B.

With the standard CIGS/CdS/i-ZnO/Al:ZnO structure, the finished cells have a conversion efficiency as high as 6.10% with open circuit voltage V_{oc} 480mV, short circuit current J_{sc} 26.05mA/cm², and fill factor FF 50% (see figure 5.8). The calculated series and shunt resistances are 3.7 Ωcm^2 and 266 Ωcm^2 , respectively. The

increased shunt resistance from solar cells made from recipe A may result from better film morphology and less shunt paths. Compared to record devices¹⁸, small CIGS grain size at the CIGS/Mo interface plays an important role in limiting J_{sc} and FF .

5.5 Improved CIGS crystallinity

By replacing GaCl_3 and ethanolamine with GaAcac_3 and other reagents, carbon contamination was eliminated resulting in a better grain growth and better IV performance. However, small CIGS crystals near Mo layers still existed and potentially acted as recombination centers which prevent the minority carriers from reaching to the junctions. Two possible reasons could explain the formation of small CIGS crystals near the Mo back contact: Ga concentration gradient and insufficient Se vapor pressure during selenization.

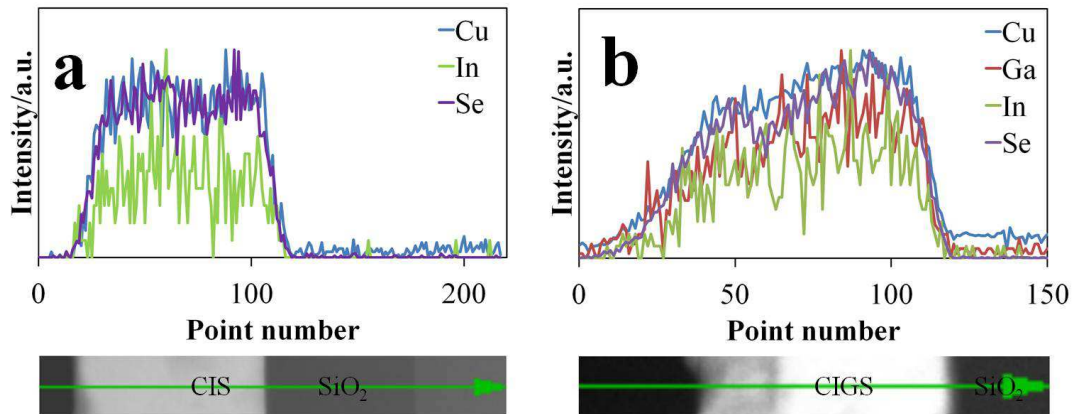


Figure 5.9 TEM elemental profiles of CIS and CIGS thin films.

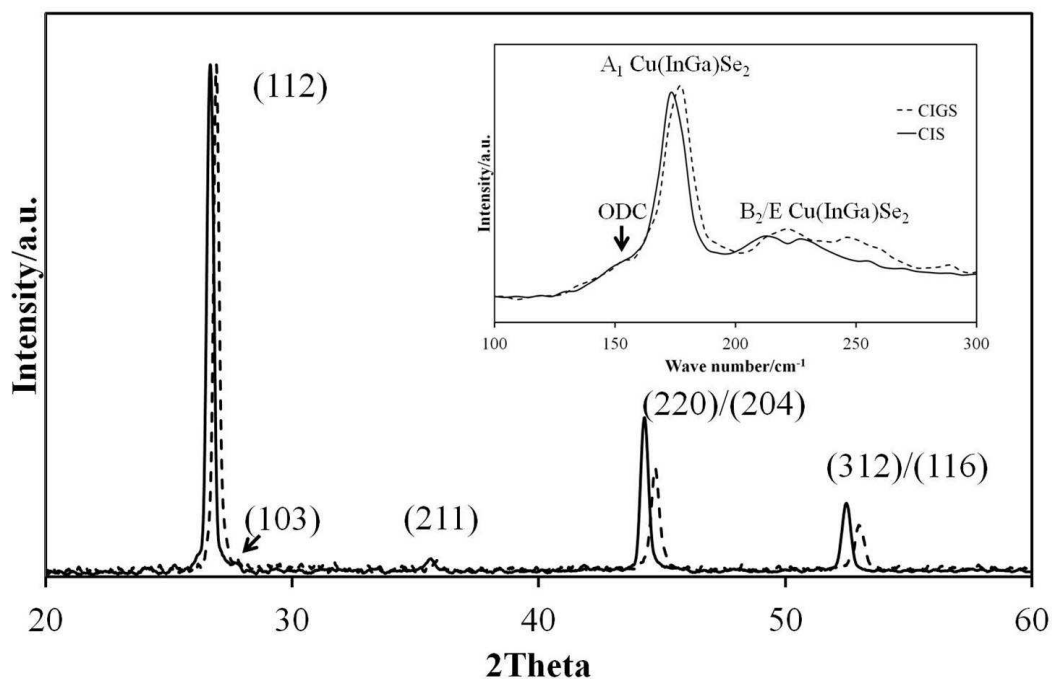


Figure 5.10 XRD comparison of CIS and CIGS films, Inset: Raman spectra for the same films.

In figure 4.14(a) and (b), the CIS film shows a relatively uniform degree of crystallinity with fairly large grain size across the film whereas the CIGS film exhibits a dual-layer structure: a large-crystal layer at top and a small-crystal layer below. Based on the results of chemical mapping analysis shown in figure 4.14(c-d) and EDS line scans across both films shown in the figure 5.9, it is evident that the distribution of all elements are relatively even in both films. These results indicate that the separated dual-layer structure in the CIGS film is not resulted from the non-uniform elemental distribution, such as gallium gradient. XRD and Raman spectra shown in figure 5.10 also confirm the chemical purity for both films and exclude the existence

of binary selenides. Seyrling *et al.*⁷⁸ found that by increasing the Ga content in the CIGS films, the CIGS grain size decreases. Although a different deposition technique (i.e. co-evaporation) was used in their study, a similar influence of Ga content on grain size and structure could also occur in our films. Therefore, the incorporation of gallium into CIS is one of the possible reasons for the small CIGS crystals at the interface.

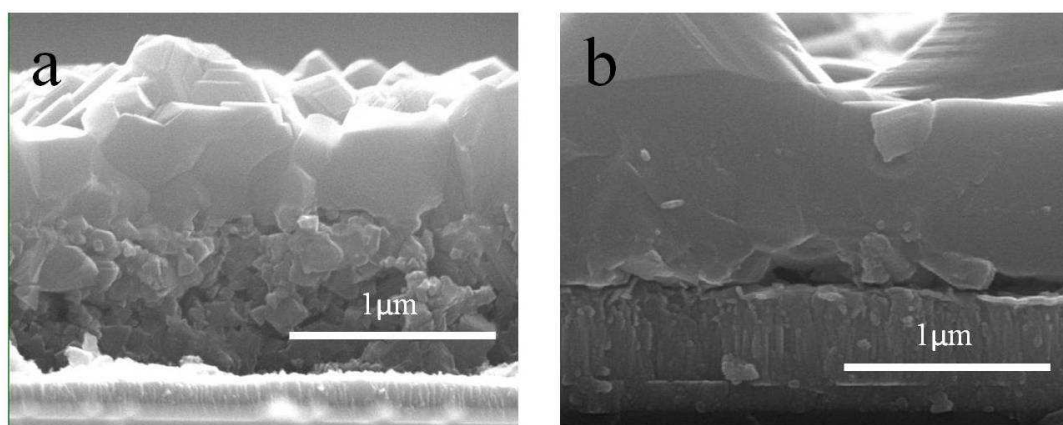


Figure 5.11 SEM cross-section images of CIGS films selenized at low Se pressure (a) and high Se pressure (b).

Kaelin *et al.*³² have studied the influence of Se vapor pressure on CIGS grain growth from metal nanoparticle precursors during selenization. They found that low Se vapor pressure resulted in small CIGS crystals at the interface of CIGS absorber layer and Mo back contact layer whereas the high Se vapour pressure resulted in much larger CIGS crystals. In our experiment, we found Se vapour pressure has similar impact on CIGS grain growth. Figure 5.11 show SEM cross-sectional images of CIGS films annealed under low Se vapor pressure (figure 5.11a) and high Se pressure (figure

5.11b). Compared with the CIGS film selenized under lower Se vapour pressure, the high Se vapour pressure improves the crystallization and enlarges the CIGS grain size dramatically. An interesting observation about the selenization is that increasing the duration of selenization does not improve the crystallization of these small crystals under low selenium pressure condition. This observation suggests that once the top dense part of CIGS films is formed, it may potentially behave as a barrier for the transport of selenium to the interface of CIGS and Mo layers thus the selenium concentration at the bottom part of film is not high enough for enhanced grain growth. Therefore high selenium vapor pressure is needed to ensure sufficient amount of selenium for the enhanced grain growth throughout the entire absorber film. We were able to fabricate highly crystalline CIGS thin films with micron-sized grains after selenization using a high Se vapour pressure.

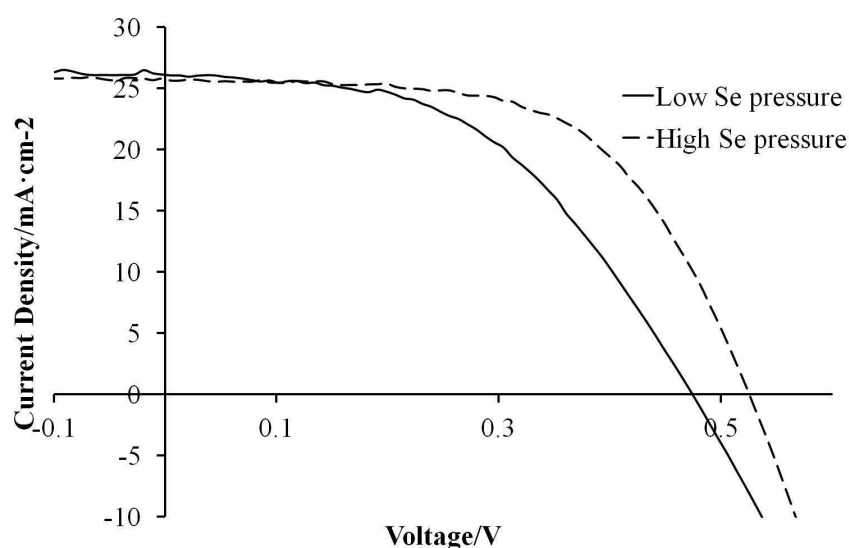


Figure 5.12 J-V characteristics of CIGS solar cells selenized at different Se partial pressures.

Current-voltage and device characteristics of different selenized samples are presented in figure 5.12 and table 5.4. The energy conversion efficiency increased to 8.01% for cells fabricated using CIGS films annealed at high Se partial pressure. In contrast to the energy conversion efficiency of 6.10% for cells fabricated using lower Se partial pressure, the improvement of cell performance mainly results from the increase of V_{oc} and fill factor. The high Se partial pressure benefits the grain growth of CIGS and produces larger grains with less grain boundary areas which reduce minority carrier recombination rate and improve the quality of absorber films in terms of diode ideality factor A and saturation current density J_0 leading to the increase of V_{oc} according to equation 1. Considering the similar cell structures in these two devices, the reason for the decrease of series resistance R_{series} and the increase of shunt resistance R_{shunt} are attributed to the improved crystallinity of CIGS films. Compared to solar cells with 19.9% efficiency, the large value of R_{series} is likely a result of interface and contact barriers. The smaller R_{shunt} could be attributed to pinholes and cracks in the absorber film.

$$V_{oc} = \frac{Ak_bT}{q} \ln \left(\frac{J_{sc}}{J_0} \right) \quad (1)$$

Table 5.4 Device characteristics of CIGS solar cells selenized at different partial Se pressures

Cell	V_{oc} mV	J_{sc} $\text{mA} \cdot \text{cm}^{-2}$	η %	FF %	R_{series} Ωcm^2	R_{shunt} Ωcm^2	A	J_0 $\text{mA} \cdot \text{cm}^{-2}$
Low Se	473	26.05	6.10	49	3.7	266	2.9	$3.9\text{e-}2$
High Se	525	25.69	8.01	59	2.3	614	2.24	$2.5\text{e-}3$

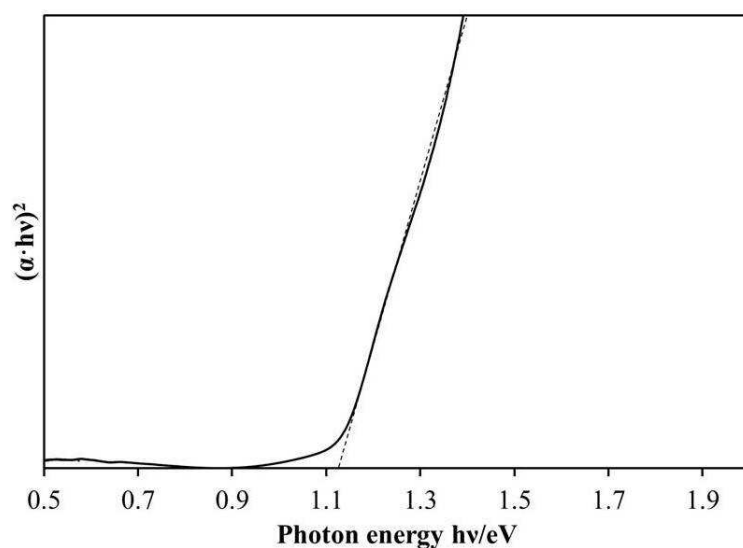


Figure 5.13 Bandgap measurement by UV-Vis absorption.

In figure 4.18, the External Quantum Efficiency (EQE) of a solar cell selenized at high Se partial pressure shows that the efficiency stays around 70% in the range of 500-650nm and decreases gradually afterwards. The bandgap of the absorber layer is estimated to be 1.13eV which is consistent with the bandgap extracted from the absorption measurement (figure 5.13). The efficiency loss below 500nm is by virtue of CdS and ZnO absorption. Based on the EQE curve, one can conclude that the major energy loss of short circuit current is a result of poor carrier collection efficiency in the range of 650nm to 1100nm which could be attributed to severe backside recombination and short minority carrier lifetime. This poor minority-carrier collection problem is also indicated by the EQE voltage bias dependence shown in

figure 4.19 top inset, where at reverse bias of 1 V, the collection of carrier at longer wavelength becomes more efficient compared to the values at 0 V bias. In figure 5.11b, the cross-sectional image shows voids at the backside of the absorber film. Longer wavelength photons travel further distance in the absorber layer and are absorbed mostly at the back of the absorber layer. Therefore, increasing minority carrier lifetime and reducing voids at interfaces are needed to improve the collection efficiency of longer wavelength photons.

5.6 Future works

Carrier lifetime describing the average time for a minority carrier between generation and recombination is one of the most important parameters for semiconductor devices, especially for solar cells. The diffusion length L of the minority carriers is proportional to the square root of the product of carrier lifetime τ and diffusion coefficient D . Equation 2 shows the photocurrent in solar cells has a value equal to the generated carriers by light in the depletion region of the diode and a minority carrier diffusion length on either side of the p-n junctions⁶². For CIGS thin film solar cells, the carriers collected in p-side predominates because most of light is absorbed in p-type CIGS layers. Therefore long minority carrier lifetime (i.e. electron) in CIGS films is crucial for high-efficiency solar cells.

$$J_L = qG(L_e + W + L_h)(2)$$

EQE spectra presented in figure 4.18 shows limited collection of photocurrent for long wavelength photons, which could be attributed to severe backside recombination and

short minority carrier lifetime. Besides, short carrier lifetime is expected to lower V_{oc} as well⁷. So it is desirable to measure the lifetime of CIGS films fabricated by our solution-based process to determine and understand the origin of current loss, which will provide very useful information to improve the efficiency of CIGS solar cells.

The J-V characteristics of our fabricated CIGS solar cells reveal considerably high series resistance which decreases both FF and η . The blocking back contact or barriers arising from the buffer/absorber interface or grain boundaries are the common sources for high series resistance⁷. In order to unveil the real cause for this high series resistance, it is necessary to conduct temperature-dependant J-V and capacitance measurements. Moreover, these measurements can also provide insightful information for recombination mechanism, defect density and defect energy^{7, 72}. All of these are very useful to identify device/material problems and guide the improvement of deposition processing.

Grazing incidence XRD was used to detect the composition uniformity of CIGS films as a function of film depth. In figure 5.14, the (112) peak of CIGS centred near 27 degrees keeps constant for incident angles from 5 to 0.5 degrees. The GIXRD results indicate a uniform elemental distribution across the CIGS film that is consistent with the cross-sectional TEM elemental analysis shown in figure 5.9. Usually gallium gradients were intentionally introduced to optimize the electronic properties of CIGS devices for high performance CIGS thin film solar cells^{79, 80}. Therefore, for our

process gallium gradients can potentially be controlled by simply adjusting the ratios of dissolved metal compounds in the precursor inks.

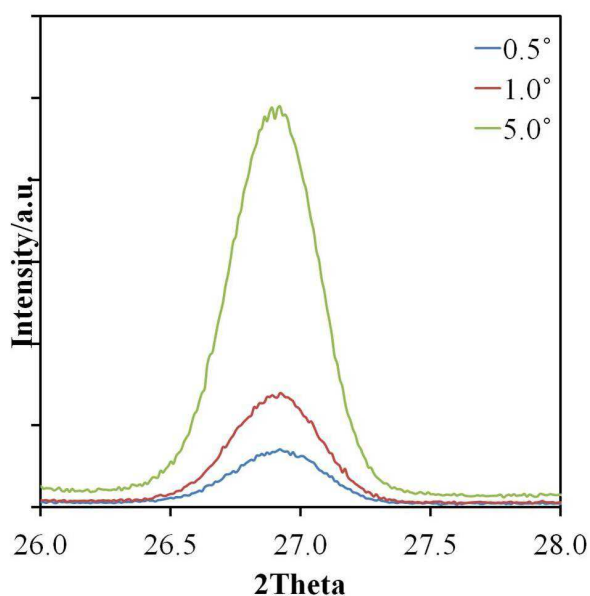


Figure 5.14 Grazing incidence XRD of a CIGS film at different angles.

In addition, the optimization of deposition processes of buffer layer CdS and TCO layers and selenization process is able to reduce the series resistance and interface defects and achieve better crystallinity in CIGS films, which will further increase the performance of solar cells.

Chapter 6 Conclusion

In summary, a simple solution-based deposition process using newly developed air-stable, low-cost inks is developed for the fabrication of high quality CIGS solar cells. The inks used for the fabrication of CIGS thin films consist of commercially available low-cost compounds and can be processed using various printing and coating techniques. In addition, printing in an atmospheric environment is able to further reduce the manufacture cost and produce absorber thin films at large scale with high raw material utilization. No binary selenides, detrimental by-products for CIGS synthesis, were formed in CIGS thin films. CIGS solar cells using recipe A achieved 5.04% efficiency with a short circuit current (J_{sc}) of 29.78 mA/cm², an open circuit voltage (V_{oc}) of 386 mV and a fill factor (FF) of 0.44.

By optimizing the chemicals used in the formulated inks, carbon-free CIGS thin films were able to be fabricated for the first time. The obtained CIGS films were used to make thin film solar cells with an open circuit voltage V_{oc} of 480mV, a short circuit current J_{sc} of 26.05mA/cm², a fill factor FF of 0.50 and a conversion efficiency as high as 6.10%. The increasing of solar cell efficiency is mainly caused by virtue of the elimination of carbon contamination.

By increasing Se vapor pressure during selenization, the small CIGS grains can be densified. Highly crystalline CIGS films with micrometer-sized grains could be fabricated. 8.01% energy conversion efficiency could be achieved with improved V_{oc} ,

FF , R_{series} , R_{shunt} and diode quality factor. Less grain boundaries reduced the electron-hole recombination and substantially improved the quality of the absorber material.

References

1. M. A. Green, K. Emery, Y. Hishikawa, W. Warta and E. D. Dunlop, *Prog. Photovolt. Res. Appl.*, 2012, **20**, 12.
2. N. Inc, in *17th International Photovoltaic Science and Engineering Conference*, Tokyo, Japan, 2007.
3. Q. Guo, G. M. Ford, H. W. Hillhouse and R. Agrawal, in *37th IEEE Photovoltaic Specialists Conference*, Seattle, WA, 2011, p. 003522.
4. V. Kapur, R. Kemmerle, A. Bansal, J. Haber, J. Schmitzberger, P. Le, D. Guevarra, V. Kapur and T. Stempien, in *33rd IEEE Photovoltaic Specialists Conference*, San Diego, US, 2008.
5. R. N. Bhattacharya, W. Batchelor, J. F. Hiltner and J. R. Sites, *Appl. Phys. Lett.*, 1999, **75**, 1431.
6. J. F. Guillemoles, J. P. Connolly, O. Ramdani, O. Roussel, D. Guimard, V. Bermudez, N. Naghavi, P. P. Grand, L. Parissi, J. Kurdi, J. Kessler, O. Kerrec and D. Lincot, *J. Nano Res.*, 2008, **4**, 79.
7. D. A. R. Barkhouse, O. Gunawan, T. Gokmen, T. K. Todorov and D. B. Mitzi, *Prog. Photovolt: Res. Appl.*, 2012, **20**, 6.
8. B. Weil, S. T. Conner and Y. Cui, *J. Am. Chem. Soc.*, 2010, **132**, 6642.
9. D. Lee, Y.-J. Chang, G. S. Herman and C.-H. Chang, *Adv. Mater.*, 2007, **19**, 843.
10. D. Lee, Y.-J. Chang, G. S. Herman and C.-H. Chang, *Adv. Mater.*, 2007, **19**, 843-847.
11. V. K. Kapur, M. Fisher and R. Roe, in *Mat. Res. Soc. Symp. Proc*, 2001, p. H2.6.1.
12. V. K. Kapur, A. Bansal, P. Le and O. I. Asensio, *Thin Solid Films*, 2003, **431-432**, 53.

13. T. Negami, Y. Hashimoto, M. Nishitani and T. Wada, *Sol. Energy Mater. Sol. Cells*, 1997, **49**, 343.
14. U. Rau and H. W. Schock, in *Solar Cells: Materials, Manufacture and Operation*, eds. T. Markvart and L. Castaner, Elsevier, Great Britain, 2005, pp. 305-349.
15. J. Parkes, R. D. Tomlinson and M. J. Hampshire, *J. Crystal Growth*, 1973, **20**, 315.
16. R. A. Mickelsen and W. S. Chen, *Appl. Phys. Lett.*, 1980, **36**, 371.
17. P. Jackson, D. Hariskos, E. Lotter, S. Paetel, R. Wuerz, R. Menner, W. Wischmann and M. Powalla, *Prog. Photovolt: Res. Appl.*, 2011, 10.1002/pip.1078.
18. I. Repins, M. A. Contreras, B. Egaas, C. DeHart, J. Scharf, C. L. Perkins, B. To and R. Noufi, *Prog. Photovolt: Res. Appl.*, 2008, **16**, 235.
19. B. J. Stanbery, *Critical Reviews in Solid State and Materials Sciences*, 2002, **27**, 73.
20. P. Würfel, *Physics of solar cells: from basic principles to advanced concepts*, WILEY-VCH, Germany, 2009.
21. A. M. Gabor, J. R. Tuttle, D. S. Albin, M. A. Contreras, R. Noufi and A. M. Hermann, *Appl. Phys. Lett.*, 1994, **65**, 198.
22. H. Rau and A. Rabenau, *J. Solid State Chem.*, 1970, **1**, 515.
23. J. Schmidtke, *Optics Express*, 2010, **18**, A477.
24. J. A. Frantz, R. Y. Bekele, V. Q. Nguyen, J. S. Sanghera, A. Bruce, S. V. Frolov, M. Cyrus and I. D. Aggarwal, *Thin Solid Films*, 2011, **519**, 7763.
25. M. Marudachalam, H. Hichri, R. Klenk, R. W. Birkmire, W. N. Shafarman and J. M. Schultz, *Appl. Phys. Lett.*, 1995, **67**, 3978.
26. N. G. Dhere and K. W. Lynn, *Solar Energy Materials and solar cells*, 1996, **41/42**, 271.

27. H.-R. Hsu, S.-C. Hsu and Y. S. Liu, *solar Energy*, 2012, **86**, 48.
28. A. Halbe, P. Johnson, S. Jackson, R. Weiss, U. Avachat, A. Welsh and A. P. Ehiasarian, *Mater. Res. Soc. Symp. Proc.*, 2010, **1210**.
29. J. H. Shi, Z. Q. Li, D. W. Zhang, Q. Q. Liu, Z. Sun and S. M. Huang, *Prog. Photovolt: Res. Appl.*, 2011, **19**, 160.
30. A. N. Y. Samaan, R. Vaidhyanathan, R. Noufi and R. D. Tomlinson, *Solar Cells*, 1985, **16**, 181.
31. L. Eldada, M. Taylor, B. Sang, S. McWilliams, R. Oswald and B. J. Stanbery, *Proc. of SPIE*, 2008, **7039**, 70390M-70391.
32. M. Kaelin, D. Rudmann, F. Kurdesau, T. Meyer, H. Zogg and A. N. Tiwari, *Thin Solid Films*, 2003, **431-432**, 58.
33. B. M. Sager, D. Yu and M. R. Robinson, Nanosolar Inc., US, 2008, p. 15.
34. S. Yoon, T. Yoon, K.-s. Lee, S. Yoon, J. M. Ha and S. Choe, *Solar Energy Materials & Solar Cells*, 2009, **93**, 783.
35. C. Eberspacher, K. Pauls and J. Serra, in *28th IEEE Photovoltaic Specialists Conference*, Anchorage, Alaska, 2000, p. 517.
36. Q. Guo, S. J. Kim, M. Kar, W. N. Shafarman, R. W. Birkmire, E. A. Stach, R. Agrawal and H. W. Hillhouse, *Nano Letters*, 2008, **8**, 2982.
37. M. G. Panthani, V. Akhavan, B. Goodfellow, J. P. Schmidtke, L. Dunn, A. Dodabalapur, P. F. Barbara and B. A. Korgel, *J. Am. Chem. Soc.*, 2008, **130**, 16770.
38. W. Shockley and H. J. Queisser, *J. Appl. Phys.*, 1961, **32**, 510.
39. Q. Guo, G. M. Ford, H. W. Hillhouse and R. Agrawal, in *34th IEEE Photovoltaic Specialists Conference*, Philadelphia, PA, 2009, p. 002126.
40. Q. Guo, G. M. Ford, H. W. Hillhouse and R. Agrawal, *Nano Letters*, 2009, **9**, 3060.

41. V. A. Akhavan, M. G. Panthani, B. W. Goodfellow, D. K. Reid and B. A. Korgel, *Optics Express*, 2010, **18**, A411.
42. Ball Mill, http://en.wikipedia.org/wiki/Ball_mill.
43. T. Arita, N. Suyama, Y. Kita, S. Kitamura, T. Hibino, H. Takada, K. Omura, N. Ueno and M. Murozono, in *20th IEEE Photovoltaic Specialists Conference*, Las Vegas, NV, 1988, p. 1650.
44. A. Vervaeet, M. Burgelman, I. Clemminck and M. Casteleyn, in *10th European Photovoltaic Solar Energy Conference*, Lisbon, Portugal, 1991, p. 900.
45. T. Wada, Y. Matsuo, S. Nomura, Y. Nakamura, A. Miyamura, Y. Chiba, A. Yamada and M. Konagai, *Phys. Stat. Sol. (a)*, 2006, **203**, 2593.
46. C. B. Murray, D. J. Norris and M. G. Bawendi, *J. Am. Chem. Soc.*, 1993, **115**, 8706.
47. B. Li, Y. Xie, J. Huang and Y. Qian, *Adv. Mater.*, 1999, **11**, 1456.
48. X. Gou, F. Cheng, Y. Shi, L. Zhang, S. Peng, J. Chen and P. Shen, *J. Am. Chem. Soc.*, 2006, **128**, 7222.
49. D. L. Schulz, C. J. Curtis, R. A. Flitton, H. Wiesner, J. Keane, R. J. Matson, K. M. Jones, P. A. Parilla, R. Noufi and D. S. Ginley, *J. Elec. Mater.*, 1998, **27**, 433.
50. D. Lincot, J. F. Guillemoles, S. Taunier, D. Guimard, J. Sicx-Kurdi, A. Chaumont, O. Roussel, O. Ramdani, C. Hubert, J. P. Fauvarque, N. Bodereau, L. Parissi, P. Panheleux, P. Fanouillere, N. Naghavi, P. P. Grand, M. Benfarah, P. Mogensen and O. Kerrec, *Solar Energy*, 2004, **77**, 725.
51. G. Hodes, T. Engelhard, D. Cahen, L. L. Kazmerski and C. R. Herrington, *Thin Solid Films*, 1985, **128**, 93.
52. J. Herrero and J. Ortega, *Solar Energy Mater.*, 1990, **20**, 53.
53. R. N. Bhattacharya, *J. Electrochem. Soc.*, 1983, **130**, 2040.

54. D. B. Mitzi, in *Solution processing of inorganic materials*, ed. D. B. Mitzi, John Wiley & Sons, Inc., 2009, pp. 77-102.
55. D. B. Mitzi, M. Yuan, W. Liu, A. Kellock, S. J. Chey, V. Deline and A. G. Schrott, *Adv. Mater.*, 2008, **20**, 3657.
56. D. B. Mitzi, M. Yuan, W. Liu, A. J. Kellock, S. J. Chey, L. Gignac and A. G. Schrott, *Thin solid films*, 2009, **517**, 2158.
57. T. K. Todorov, O. Gunawan, T. Gokmen and D. B. Mitzi, *Prog. Photovolt. Res. Appl.*, 2012, In press.
58. L. Oliveira, T. Todorov, E. Chassaing, D. Lincot, J. Carda and P. Escribano, *Thin Solid Films*, 2009, **517**, 2272.
59. M. Kaelin, D. Rudmann, F. Kurdesau, H. Zogg, T. Meyer and A. N. Tiwari, *Thin solid films*, 2005, **480-481**, 486.
60. S. Jeong, B.-S. Lee, S. Ahn, K. Yoon, Y.-H. Seo, Y. Choi and B.-H. Ryu, *Energy & Environmental Science*, 2012, **5**, 7539-7542.
61. R. Pierret, *Semiconductor device fundamentals*, Addison-Wesley publishing company, 1996.
62. M. Green, *Solar cells: operating principles, technology, and system applications*, Prentice-Hall, 1982.
63. J. R. Sites and P. H. Mauk, *Solar Cells*, 1989, **27**, 411.
64. Z. Lin, D. Han and S. Li, *J. Therm. Anal. Calorim.*, 2012, **107**, 471.
65. M. D. Judd, B. A. Plunkett and M. I. Pope, *J. Therm. Anal.*, 1974, **6**, 555.
66. S. Yamanaka, M. Konagai and K. Takahashi, *Jpn. J. Appl. Phys.*, 1989, **28**, L1337.
67. S. Yamanaka, M. Tanda, N. Nakada, A. Yamada, M. Konagai and K. Takahashi, *Jpn. J. Appl. Phys.*, 1991, **30**, 442.

68. S. Shirakata, H. Kubo, C. Hamaguchi and S. Isomura, *Jpn. J. Appl. Phys.*, 1997, **36**, L1394.
69. W. Horig, H. Neumann and H. Sobotta, *Thin Solid Films*, 1978, **48**, 67.
70. C. Rincon and J. Gonzalez, *Phys. Stat. Sol. (b)*, 1983, **118**, K21.
71. S. S. Hegedus and W. N. Shafarman, *Prog. Photovolt: Res. Appl.*, 2004, **12**, 155.
72. Q. Cao, O. Gunawan, M. Copel, K. B. Reuter, J. Chey, V. Deline and D. B. Mitzi, *Adv. Energy Mater.*, 2011, **1**, 845.
73. D. Cahen and R. Noufi, *J. Phys. Chem. Solids*, 1992, **53**, 991.
74. I. Barin, *Thermochemical data of pure substances*, VCH publishers, Inc, New York, NY (USA), 1995.
75. M. Burgelman, F. Engelhardt, J. F. Guillemoles, R. Herberholz, M. Igalson, R. Klenk, M. Lampert, T. Meyer, V. Nadenau, A. Niemegeers, J. Parisi, U. Rau, H. W. Schock, M. Schmitt, O. Seifert, T. Walter and S. Zott, *Prog. Photovolt. Res. Appl.*, 1997, **5**, 121.
76. A. Rockett and R. W. Birkmire, *J. Appl. Phys*, 1991, **70**, R81.
77. M. Nieminen, L. Niinisto and E. Rauhala, *J. Mater. Chem.*, 1996, **6**, 27.
78. S. Seyrling, S. Calnan, S. Bucheler, J. Hupkes, S. Wenger, D. Bremaud, H. Zogg and A. N. Tiwari, *Thin Solid Films*, 2009, **517**, 2411.
79. B. E. McCandless, *Mater. Res. Soc. Symp. Proc.*, 2005, **865**, F4.1.1.
80. I. Repins, M. Contreras, M. Romero, Y. Yan, W. Metzger, J. Li, S. Johnston, B. Egaas, C. DeHart, J. Scharf, B. E. McCandless and R. Noufi, in *Photovoltaic specialists conference*, San Diego, 2008.